Graduate Theses and Dissertations   Graduate School

4-22-2008

Stress Analysis and Mechanical Characterization of Thin Films for Microelectronics and MEMS Applications

Patrick Waters
University of South Florida

Follow this and additional works at: https://scholarcommons.usf.edu/etd

Part of the American Studies Commons

www.manaraa.com

Stress Analysis and Mechanical Characterization of Thin Films for Microelectronics and

MEMS Applications

by

Patrick Waters

A dissertation submitted in partial fulfillment
of the requirements for the degree of
Doctor of Philosophy
Department of Mechanical Engineering
College of Engineering
University of South Florida

Major Professor: Alex Volinsky, Ph.D.
Craig Lusk, Ph.D.
Frank Pyrtle, Ph.D.
Ralph Fehr, Ph.D.
George Nolas, Ph.D.

Date of Approval:
April 22, 2008

Keywords: residual stress, sputtering, X-ray diffraction, nanoindentation, wafer curvature

Dedication

I would like to dedicate this manuscript to my parents. This would not have been

possible without the support and guidance they have provided me throughout the years.

Acknowledgements

I would like to thank my advisor Alex Volinsky for guiding me through this process. He has always made himself available for any questions and problems that I've had. I would also like to thank the staff of the Mechanical Engineering Department for all the help they've given me throughout my entire stay at USF, specifically Sue Britten, Wes Frusher and Shirley Tevort. Most importantly, I would like to thank my wife Heather for her incredible patience in dealing with me while I've been in graduate school.

Note to Reader

The original of this document contains color that is necessary for understanding

the data. The original dissertation is on file with the USF library in Tampa, Florida.

Table of Contents

List of Tables

List of Figures

iv

ix

List of Nomenclature

a	lattice constant, interfacial crack length
A	fracture surface area
A_c	indentation contact area
c	plastic zone size
d	lattice plane spacing
D	grain size
E	Young's modulus
E_r	reduced modulus
F_E	electrostatic force constant
G	strain energy release rate
h	indentation depth
H	thin film hardness
I	number of incident ions
j	current density
k	curvature
K	stress intensity at a crack tip ($K_{I,II,III}$ are used for mode I, II and III)
K_C	fracture toughness
M	atomic mass
n_e	electron concentration
N_s	number of sputtered atoms
P	load
q	electronic charge
R	radius of curvature
s_n'	reduced nuclear stopping cross section
S	indentation unloading stiffness
S_n	nuclear stopping power
S_y	sputtering yield
T	temperature
t	film thickness
U	energy
V_I	indentation volume
W_A	thermodynamic work of adhesion
$W_{A,P}$	practical work of adhesion
Z	atomic number
α	thermal expansion coefficient, Dundar's parameter
β	Dundar's parameter
γ	surface energy, indentation correction factor
Γ_i	interface fracture toughness
δ	displacement

ε	strain
λ	wavelength
Λ	sputtering constant dependent on target material
μ	shear modulus
ν	Poisson's ratio
σ	stress
ψ	mode mixity (phase) angle

Stress Analysis and Mechanical Characterization of Thin Films for Microelectronics and
MEMS Applications

Patrick Waters

ABSTRACT

Thin films are used for a variety of applications, which can include electronic

devices, optical coatings and decorative parts. They are used for their physical, electrical,

magnetic, optical and mechanical properties, and many times these properties are

required simultaneously. Obtaining these desired properties starts with the deposition

process and they are verified by a number of analysis techniques after deposition. A DC

magnetron sputter system was used here to deposit tungsten films, with film thickness

and residual stress uniformity being of primary interest. The film thickness was

measured to vary by up to 45 % from the center to outer edge of a 4" wafer. Ar pressure

was found to influence the thin film residual stress with lower Ar pressures leading to

compressive residual stress (-1.5 GPa) and higher Ar pressures leading to tensile residual

stress (1 GPa). Residual stress measurements of the tungsten films were made using a

wafer curvature technique and X-ray diffraction. The results of the two techniques were

compared and found to be within 20 %.

Nanoindentation was used to analyze the mechanical properties of several types

of thin films that are commonly used in microelectronic devices. Thin film reduced

modulus, hardness, interfacial toughness and fracture toughness were some of the

mechanical properties measured. Difficulties with performing shallow indents (less than

100 nm) were addressed, with proper calibration procedures for the indentation equipment and tip area function detailed. Pile-up during the indentation of soft films will lead to errors in the indentation contact depth and area, leading to an overestimation of the films' reduced modulus and hardness. A method was developed to account for pile-up in determining the indentation contact depth and calculating a new contact area for improving the analysis of reduced modulus and hardness.

Residual stresses in thin films are normally undesired because in extreme cases they may result in thru-film cracking or interfacial film delamination. With the use of lithography techniques to pattern wafers with areas of an adhesion reducing layer, thin film delamination was controlled. The patterned delamination microchannels may be used as an alternative method of creating microchannels for fluid transport in MEMS devices. Delamination morphology was influenced by the amount of residual stress in the film and the critical buckling stress, which was primarily controlled by the width of the adhesion reducing layers.

Chapter 1

Introduction

1.1 Motivation for Thin Film and MEMS Research

The current trend in technology is to make everything smaller and faster. A few decades ago a person was lucky to have access to a computer at work. Now it is not only standard to have a personal computer at both work and home, but computers can even be found in our vehicles and in the form of cell phones and personal digital assistants (PDAs). This is possible because of a number of improvements in the semiconductor industry such as: improved integration level, compactness, functionality, storage and use of power, reduced cost and increased speed. These improvements allowed for smaller devices to be contrived and have made computers available to the mass population. The development of microfabrication in the semiconductor industry was sparked by the invention of the transistor in 1947. Before transistors, large vacuum tubes were used in electronic equipment and computers that were the size of rooms. Now, hundreds of millions of transistors are placed on semiconductor chips, with the size of transistors being reduced down to the sub-micrometer range.

The increase in device density has been following a trend known as Moore's law. In 1965, Gordon Moore a co-founder of Intel, made a prediction on the development of semiconductor technology that the number of transistors on a chip will approximately double every eighteen months [1]. This prediction has been accurate for the last four

1

decades. The primary reason for this exponential growth in integrated circuit (IC) technology is the reduction in manufacturable feature size, which is defined as the minimum element size on a chip. Gate widths in transistors were around 30 μm in the early 1960s, then reduced to around 10 μm in the 1970s, to less than 0.2 μm in the year 2000 and they continue to decrease. At one point physicists predicted that the lower bound of gate width would be around 50 nm for the current form of metal-oxide-semiconductor field-effect transistors (MOSFET)[2]. This prediction was challenged by the end of 2007 when Intel released its 45 nm process technology and the International Technology Roadmap for Semiconductors has recently predicted that devices will have a physical gate width of 13 nm by the year 2013 [1].

Unfortunately, for many of the materials used in these devices only the electronic, magnetic and optical properties are of focus. Chemical and mechanical properties are often overlooked because these materials are generally not thought to be meant for load bearing applications. Integrated circuits, microelectromechanical systems (MEMS), and magnetic disks are perfect examples of where materials are needed not only for their electric, magnetic and optical properties, but for their chemical and mechanical properties as well [3]. The manufacturing of integrated circuits is a perfect example where high levels of stress may be introduced during processing. In order to avoid device failure, they must be able to withstand the stresses introduced in film deposition and processing. The types of stress may depend on the deposition and processing methods involved, such as residual stresses introduced by sputter deposition and thermal stresses introduced because of deposition at elevated temperatures and subsequent cooling to room temperature.

Elevated temperatures are often required during the processing of ICs and this will lead to thermal stresses when there are materials with different thermal expansion coefficients. The expansion and contraction of a material is normally proportional to the temperature change it experiences and can be seen in the following equation

$$\varepsilon = \alpha \cdot \Delta T \qquad (1),$$

where ε is the strain, α is the thermal expansion coefficient and ΔT is the change in temperature. For the case of a film/substrate combination, the strain of the film will be constrained by the substrate due to mismatched thermal expansion coefficients and the thermal stress of the film can be expressed as:

$$\sigma_f(T) = \frac{(\alpha_s - \alpha_f)\Delta T \cdot E_f}{1 - \nu_f} \qquad (2),$$

where E and ν are the modulus and Poisson's ratio, respectively, and the subscripts s and f stand for the substrate and film, respectively.

In addition to thermal stresses, integrated circuits may also be exposed to external forces that are applied during chemical mechanical planarization (CMP). The CMP process uses an abrasive/corrosive chemical slurry to remove material and irregularities from the sample surface. CMP is the final step in the damascene process, which is broken down into four basic steps: 1) oxide deposition, 2) oxide etching, 3) metal deposition and 4) metal planarization and polishing. The damascene process is commonly used for metals that cannot by plasma etched. Copper is an example of a metal that cannot be patterned using standard photolithography and plasma etching techniques. Therefore, damascene is used for copper metallization of ICs (Figure 1).

a)   b)   c)
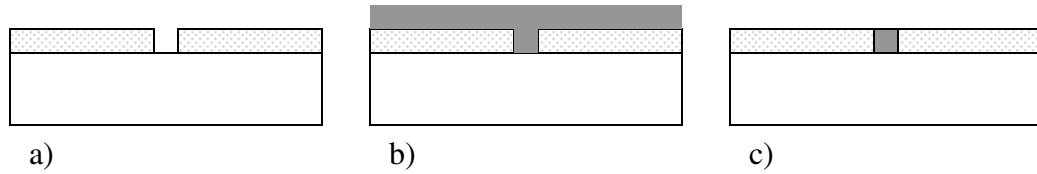
Figure 1. Damascene metallization starting with the second step: a) etch trench in oxide, b) deposit metal and c) planarization.

Figure 1 starts with the second step in the damascene process which is etching a desired pattern of trenches into a silicon dioxide layer. This is followed by the deposition of a metal film, which overfills the trenches. CMP is then used to polish the excess metal to the point where it is level with the top of the trenches. Ideally, the only metal that is left is in the trenches and this process can be repeated several times to develop multiple layers of contacts and interconnects (Figure 2).
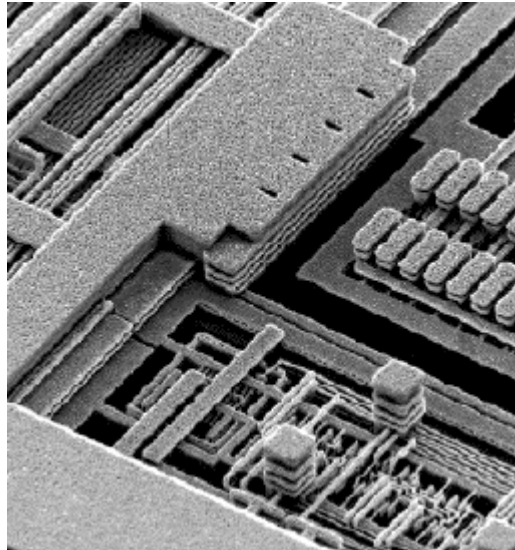
Figure 2. SEM view of IBM's six-level copper interconnect technology in an integrated circuit chip.

The last two causes for stress are common examples of what can be expected when producing ICs. One example of large stresses experienced after production is in the use of magnetic disks. Magnetic disks are often used in information storage for products

such as the hard drives in computers. During normal usage, large stresses will be experienced as a result of high rotational speeds and frequent collisions between the read/write heads and the disk surface. The collisions will occur each time the disk is turned on and off reducing the layer of air between the disk and read/write head. This layer of air between the disk and read/write head acts as a fluid dynamic bearing created by the rotation of the disk. Currently, carbon coatings in the thickness range of 5-10 nm are used to protect the magnetic layers underneath from the externally applied forces. To achieve the expected storage densities within the next few years (Gbit/in^2), it will be necessary to reduce the head to disk fly height and the protective coating thickness [4]. This ultra thin film is what stands between normal operation and failure of the hard drive. That is why a thorough understanding and control over the mechanical properties is so important.

Whatever the cause of stress, it must be accepted that stresses are commonly present and may result in deformation, fracture and delamination of films. To ensure device reliability, the mechanisms that control the mechanical properties of these materials must be understood. To understand these mechanisms, analysis and characterization of the materials and devices must be performed after processing. From there, the manufacturing parameters may be adjusted to improve the final product.

The focus of the work presented here will be on addressing issues with film deposition using DC magnetron sputtering and characterizing the film's mechanical properties using nanoindentation. It was observed that factors such as inert gas pressure used during sputter deposition will have significant effects on the residual stresses present in the deposited film. Film non-uniformities produced from sputtering were measured

5

and the factors leading to these non-uniformities will be discussed. Typically, residual stresses and film non-uniformities are not desired, but the possible use of these in creating microchannels will be examined. A close examination of using nanoindentation for measuring thin film mechanical properties was done and some potential challenges will be addressed.

1.2 Thin Films

Thin films are a perfect example of how much technology has advanced in the last two centuries. Many of the advances in the IC industry have been the result of advances in thin film technology. Thin films are now widely used for making electronic devices, optical coatings and decorative parts. They are used for their physical, electrical, magnetic, optical and mechanical properties and many times these desired properties are obtained simultaneously. By variations in the deposition process, as well as modifications of the film properties during deposition, a range of unusual properties can be obtained which are not possible with bulk materials. Additional functionality in thin films can be achieved by depositing multiple layers of different materials. Multiples film layers have found use in applications such as optical interference filters, where tens or even hundreds of layers are deposited. The layers are alternated between high and low indexes of refraction to achieve the desired filtering effects.

There are many different methods available for film deposition, but all could be broken down into three basic sequential steps: 1) A source of film material is provided, 2) the material is transported to the substrate and 3) deposition takes place. If the deposition process is relatively new, the film will be analyzed to evaluate the success of the process. The results of the analysis can then be used to adjust the deposition conditions if the film

6

properties need to be modified. Additional process control and understanding are obtained by monitoring the first three steps during film deposition. The source of the film material may be a solid, liquid, vapor or gas. For solid materials, vaporization is needed to transport the material to the substrate. This can be accomplished by heat or by an energetic beam of electrons, photons and ions. These methods are categorized as physical vapor deposition (PVD) processes. Thin film deposition processes where the source materials are brought in as gas phases are categorized as chemical vapor deposition (CVD) processes.

Film uniformity will primarily be affected by the transport and deposition steps. The transport medium plays a significant role in affecting film uniformity and may consist of a high vacuum or a fluid medium depending on the deposition method. The transport medium will directly affect the source material's arrival rate, direction and energy. The deposition behavior is determined by the source and transport factors and by conditions at the substrate surface. The principal factors are the substrate surface condition, reactivity of the arriving material and energy input. Substrate surface conditions include roughness, level of contamination, degree of chemical bonding with the arriving material and crystallographic parameters in the case of epitaxy. Epitaxial deposition is a special case of thin film deposition where film growth will be single crystal and dependent on the crystal orientation of the substrate. In order to grow properly the crystal lattices of the film and substrate must be closely matching.

Analysis of the film after deposition can be thought of as the final stage of the process monitoring. This stage consists of directly measuring those properties that are important for the application at hand. For example, properties such as the hardness for a

7

tool coating, the breakdown voltage of an insulator, or the index of refraction of an optical film are all important. Many film deposition processes are optimized by measuring the key film properties as a function of the process variables. The process variables are then adjusted in the three steps of the deposition sequence to achieve the desired product.

1.3 Thin Film Characterization

Just as the technology used for manufacturing smaller devices and new materials is evolving, so is the equipment available to test and analyze it. The reduction in material size means that there must be a change in testing equipment and methods used. It must be kept in mind that thin film material properties do not always resemble those measured at the bulk level. The application of thin films is becoming increasingly interdisciplinary in nature, leading to new demands for film characterization and properties measurements for both individual films and multilayer films. At first, single films on thick substrates were studied. Now, thin films are able to be deposited one atomic layer at a time, which creates the need for testing instrumentation that has control and sensitivity at that scale.

Atomic layer deposition (ALD) is a method that is similar to CVD, but it allows for conformal atomic level control over the deposition process. This control is achieved by introducing the reactants individually, separating the purge steps in a sequential manner and carrying out self-limiting surface reactions that occur during each step on the substrate surface. The result from using ALD is the ability to deposit films with accurate thickness control, excellent conformability and uniformity over large areas that are not achievable in CVD [5, 6]. Measurements and characterization of the film thickness, microstructure and composition can be carried out using various techniques. They

8

include ellipsometry, X-ray diffraction (XRD), transmission electron microscopy (TEM) and X-ray photoemission spectroscopy (XPS).

The previously mentioned techniques have been around for quite some time and have proven their effectiveness in analyzing ultra-thin films. So far, experimental techniques for measuring film thickness, structure, composition and surface morphology have been proven reliable. However, thin films must be characterized with respect to all the various properties equally and to the same ease and precision that we associate with testing bulk materials. Mechanical testing is lacking when material size is decreased to the extreme that we see in ALD. Questionable results are presented using nanoindentation to measure thin film elastic modulus and hardness, at contact depths below 50 nm. This is due to a measurement process that is complicated by effects such as unknown geometry of the indenter tip, surface and substrate effects and limitations in the testing equipment [7-10]. Nevertheless, researchers will continue to push the limits of the existing equipment used for these measurements and strive to find a way over the mentioned hurdles. Until then, the proper consideration should be taken when reviewing results for ultra thin films and shallow indentation depths.

1.4 Chapter Objectives

This manuscript has been broken-down into 6 different chapters. Chapter 1 was to get the reader familiar with thin films, and some of the uses and issues associated with them. Chapter 2 starts off with an introduction into DC magnetron sputtering and it then goes into the testing of a CRC-100 sputtering system. Experiments were conducted to measure the deposition and etch rates, film thickness profile and the relation between Ar pressure and residual stress in tungsten films. Two different residual stress measuring

9

techniques were the focus of Chapter 3. The objectives of the chapter were to be able to compensate for non-uniformities in film thickness and residual stress and to then compare the results of the Stoney's equation using the wafer curvature method and the $\sin^2\Psi$ technique using X-ray diffraction. The objectives of Chapter 4 were to introduce the reader to nanoindentation and the different mechanical properties it is capable of testing. Some of its challenges were addressed, specifically, calibration procedures and difficulties with testing in the sub 50 nm region. Indentation pile-up effects on soft films were also compensated for when calculating the film's reduced modulus and hardness. The objective of Chapter 5 was to propose an alternative method for manufacturing microchannels by controlling thin film delaminations. This was accomplished by using photolithography to create patterned areas of an adhesion reducing material and then the microchannels were created by depositing a compressively stressed film on top of the patterned area. A summary of the chapters is provided in Chapter 6, along with the authors intended future work.

Chapter 2

Sputter Deposition

2.1 Introduction

In the past, thermally evaporated and sputtered aluminum films were primarily
used for the contacts and interconnects of integrated circuits. Due to problems with
electromigration and RC delays, aluminum-copper interconnects became more widely
used [11]. The introduction of copper alloys resulted in larger current densities and
reduced resistivity, thereby reducing RC delays and electromigration problems.
Unfortunately, this alloy could not be easily evaporated and it was found that film
stoichiometry was maintained by glow-discharge sputtering. Another advantage of using
sputtering over evaporation becomes apparent when working with refractory materials
such as tungsten. Thermal evaporation is not appropriate for high melting temperature
materials because it is difficult to find a suitable crucible that will not contaminate the
target at high temperatures [12]. With the progression from aluminum to aluminum-
copper as the alloy of choice in IC technology, sputter deposition became an integral part
of the metallization processing in the early 1970s.

The earliest published observation of sputtering was in 1852 by Grove who was
investigating discharge tubes. During his investigation, Grove noticed the formation of a
dull coating on the surface of a highly polished silver coated copper sample. The coating
was only observed when the silver sample was the anode and the steel wire was the

11

cathode of the electrical circuit. By reversing the polarity he was able to remove the

deposited material from the silver surface [13]. He did not make any studies of the

deposited films' properties because he was more interested in the effects of the voltage

reversal on the discharge. It wasn't until years later that scientists took note of Grove's

discovery and coined the phrase "sputtering".

Earlier uses of sputtering were for creating mirrors [14], decorative ornaments and

chrome coatings on the plastic grilles of cars. Now, sputter deposition is used for various

applications across a number of industries. Sputtering is not limited by the electrical

conductivity or melting temperature of the deposited material. It can be used for

depositing materials over a wide range of thicknesses. Film thicknesses from a few

nanometers up to a few microns are normally classified as a thin film and thicknesses

above a few microns are normally considered a coating.

2.1.1 Sputtering Yield

Early theories to explain sputtering were based on the idea that bombarding ions

created areas of high local temperatures on the target, leading to an evaporation of the

target. These early theories also predicted that the sputtering rate depended on the heat of

sublimation of the target and the energy of the bombarding ions. Currently, the accepted

cause of sputtering is that sputtering is a momentum transfer process, where surface

atoms are physically ejected from a solid surface by the momentum transfer from

bombarding energetic particles.   The energetic particles are usually gaseous ions that are

accelerated from a plasma. When a solid surface is bombarded with energetic particles,

some of the target surface atoms of the solids are scattered backward as shown in Figure

3.

12
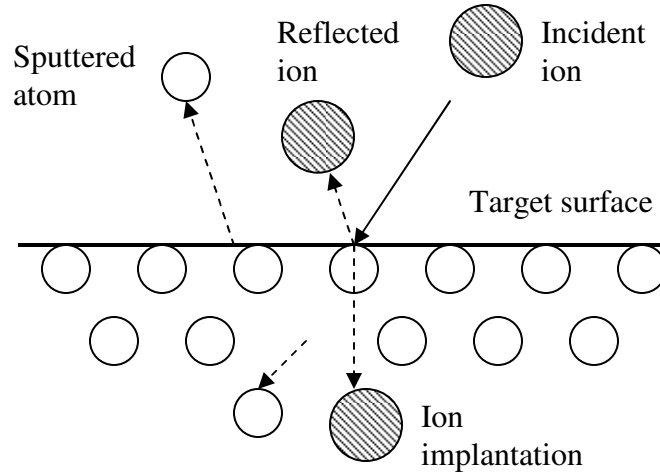
Figure 3. Physical sputtering process.

Sputtering is typically a multiple collision process involving a cascade of moving target atoms. This cascade may extend over a considerable region inside the target, but the sputtered atoms originate only in a layer near the surface. The thickness of this layer will depend on the ion mass, the ion energy and the ion-target geometry. Only atoms that gain enough energy to overcome the target binging energy will be ejected from the target, while others are displaced from normal lattice sites. A measure of the efficiency of sputtering is the sputtering yield and is defined as

$$S_y = \frac{N_s}{I} \tag{3},$$

where N_s is the number of atoms sputtered and I is the number of incident ions. The result of sputtering is like a game of billiards. If the incident ion was represented by the cue ball, the number of sputtered atoms would be the number of pool balls scattered back towards the player. The sputtering yield will be affected by many things, including the ion energy, the angle of incidence, the binding energy of the target material, the type of

13

collision cascade that occurs between the ion and target atoms, the target surface morphology and the target crystal structure [15-18].

Sigmund was the first to describe the sputtering process as a linear collision cascade and his theoretical modeling of sputtering was been widely accepted by others [15-19]. Sigmund's work, along with the contribution of others has pointed out four major concepts in the collisional description of sputtering: 1) the stopping of the projectile via nuclear energy loss to target atoms, 2) the occurrence of a linear collision cascade, 3) the escape of certain recoils through the surface potential energy barrier and 4) the introduction of anisotropy into yield distributions by lattice correlated effects within single crystal regions of the target. The Sigmund theory suggests a specific dependence of the sputtering yield on the ion energy, E, for both low and high energies [15]. Sigmund's general sputtering yield expression is a product of two terms:

$$S_y = \Lambda \cdot F_D(E) \tag{4},$$

where the first term, Λ, is a material constant that includes the range of a displaced target atom and the probability of ejection of an atom at the surface. The second term, $F_D(E)$, accounts for the energy deposited at the surface and depends on type, energy and incident angle of the ion, as well as on target parameters. The sputtering yield at low energies (E < 1 keV) is predicted to be

$$S_y = \frac{3 \cdot \alpha \cdot M_1 \cdot M_2 \cdot E}{\pi^2 (M_1 + M_2)^2 U_s} \tag{5},$$

where M_1 and M_2 are the ion and target atomic masses, U_s is the target atom's binding energy, E is the ion energy and α is a constant that depends on the mass ratio and angle of impact, but often assumes a value between 0.2 and 0.4. The low energy yield expression

14

is linear in E and does not predict a threshold. For energies above 1 keV, S_y is predicted to be

$$S_y = \frac{0.042 \cdot \alpha \cdot S_n(E)}{U_s} \tag{6},$$

where $S_n(E)$ is defined as the nuclear stopping power or nuclear energy loss cross section, and is approximated as

$$S_n = 4 \cdot \pi \cdot a \frac{Z_1 \cdot Z_2 \cdot q^2 \cdot M_1 \cdot s_n^{'}(E)}{M_1 + M_2} \tag{7},$$

where Z_1 and Z_2 are the atomic numbers of the projectile and target atoms, a is the effective radius (0.1 to 0.2 Å) over which the nuclear charge is screened by electrons during the collision, q is the electronic charge and $s_n{'}(E)$ is a reduced nuclear stopping cross section.

His theory was based on the assumption that there will be a random slowing down of the incident ions, with much of his work focused on amorphous targets. For polycrystalline materials there may be a contribution of focused collision chains to the sputtering yield that may not average out. If this contribution were substantial, the sputtering yield of polycrystalline materials would be greater than that of an amorphous target. With this effect to sputtering yield in mind, X-ray diffractometry was used to analyze the 99.95 % pure tungsten target used here. The X-ray diffraction tests were done with a Philips X'pert and the 2θ peaks are displayed in Figure 4. The corresponding d-spacing and plane orientation can be found in Table 1. Results clearly show that the target is polycrystalline.
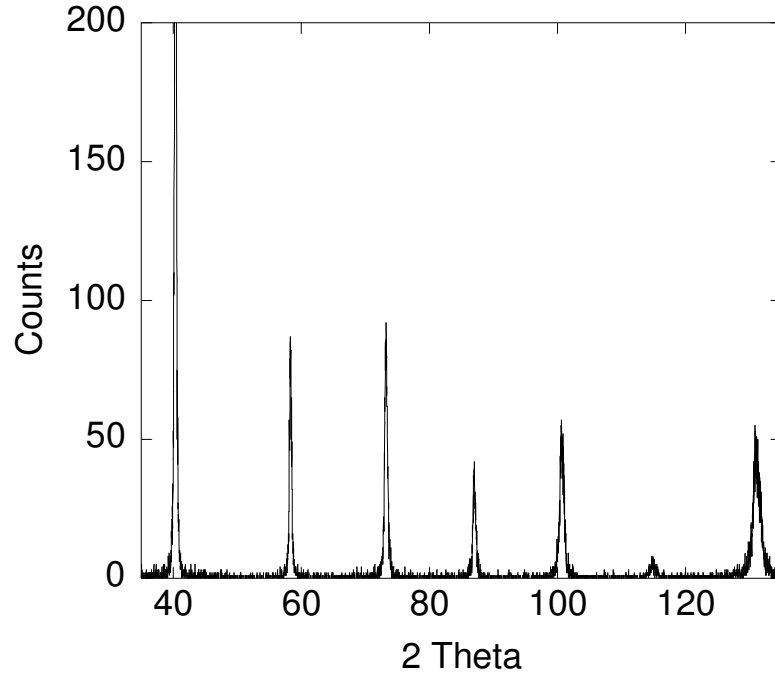
Figure 4. Tungsten target 2θ peaks.

Table 1. XRD data from tungsten target.

Pos. [°2Th.]	d-spacing [Å]	Rel. Int. [%]	hkl
40.3672	2.23441	100.00	110
58.3203	1.58221	15.65	200
73.1687	1.29351	16.20	112 reflection
86.9512	1.12047	7.30	220
100.5662	1.00224	9.38	310
115.4510	0.91332	6.22	222
131.0195	0.84645	8.43	321

It has been observed that Sigmund's theory overestimates the experimentally measured yields by a factor of 2. More recent attempts to model sputtering in the linear collision cascade regime have been made by Mahon and Vantomme. It is called the

16

"simplified collision model of sputtering in the linear cascade regime" and their sputtering yield expression is as follows [19]:

$$S_y = \frac{E}{E_{avg}} \frac{R_{pr}}{R_{pp}} \frac{1}{4}$$ (8).

The first term gives the number of recoils at the practical endpoint of the cascade, where E is the ion energy and E_{avg} is the average energy of the recoils at termination. The second term gives the fraction of recoils which are close enough to the surface to reach it and have enough energy to escape, where R_{pr} is the projected range of recoils and R_{pp} is the projected range of projectiles. The third term gives the fraction of those particles which are traveling in the right direction. By using Mahon and Vantomme's newer, simplified expression for sputtering yield, the predicted sputtering yield of tungsten with argon as the working gas was tabulated and the results are compared with Stuart's and Wehner's experimental results (Figure 5). It can also be observed in Figure 5 that there will be a theoretical maximum sputtering yield that is asymptotically approached with an increasing ion energy. This corresponds to Sigmund's predictions that the nuclear stopping power is dependent on the ion energy, thus resulting in a maximum yield. For a tungsten target with argon as the plasma, a maximum yield around 1.5 is calculated using Mahon and Vantomme's simplified collision model.

17
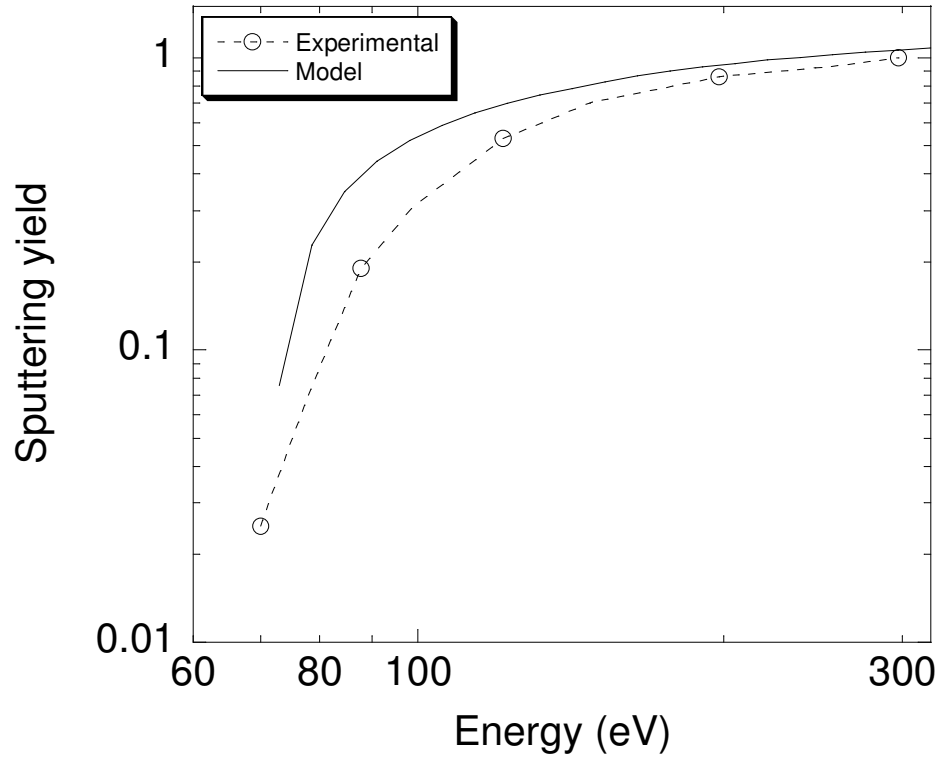
Figure 5. Comparison of Mahon model with Stuart and Wehner experimental results [19, 20].

Along with predicting the sputtering rate, it is also important to understand the dispersion of sputtered atoms from the target. The profile of dispersion will affect transport of sputtered atoms through the ambient gas and their finally resting location of the substrate and chamber walls. Sticking with the billiards analogy, just as the pool balls scatter in many directions after the break, the target atoms are sputtered from the target in a range of directions about the target normal. The number atoms ejected in a given direction is proportional to the cosine of the angle from the normal [21]. An atom ejected with a given energy has a greater chance of escaping from the surface binding energy if it is ejected along the normal. Along with the sputtered atoms, a percentage of the incident ions will be reflected from the target with a significant amount of energy, while a small

18

percent will remain in the target and are sputtered later. The fraction of energy reflected depends on mass of the incident and target atoms along with the angle of incidence.

A great deal of literature has been published attempting to further explain and simulate the interactions during the sputtering process. Many papers deal with the interactions between incident ions and the target atoms as previously summarized and others concentrate on the transport of sputtered particles through the gas phase [22-28]. The latter of the two bodies of work will be briefly discussed in the following sections and how they pertain to planar DC magnetron sputtering.

2.2 DC Magnetron Sputter Deposition

Sputtering is generally divided into four major categories: DC, AC (mostly RF), reactive and magnetron sputtering. There are clear distinctions between each of the sputtering categories and even hybrids between categories. Some of the obvious variants between categories are the power source used, whether reactive gases are present in the chamber and if there is an addition of magnetic fields. In the current research, a planar DC magnetron sputtering system was used and is considered the dominant method of physical vapor deposition using plasma.

The two main advantages of a magnetron sputtering system over a diode system are higher deposition rates and lower substrate temperatures. In magnetron sputtering systems a magnetic field is used to help prevent electrons from escaping the target region, which creates a dense plasma near the cathode surface at lower pressures. The lower pressure allow ions to be accelerated from the plasma to the cathode without loss of energy due to physical and charge exchange collisions. This produces a higher current for the same applied voltage as in simple DC discharges, which results in a higher

19

sputtering rate. Furthermore, by containing the electrons near the target surface, fewer electrons will be striking the substrate keeping substrate temperatures close to room temperature. A general system layout for a DC magnetron sputtering system can be seen in Figure 6.
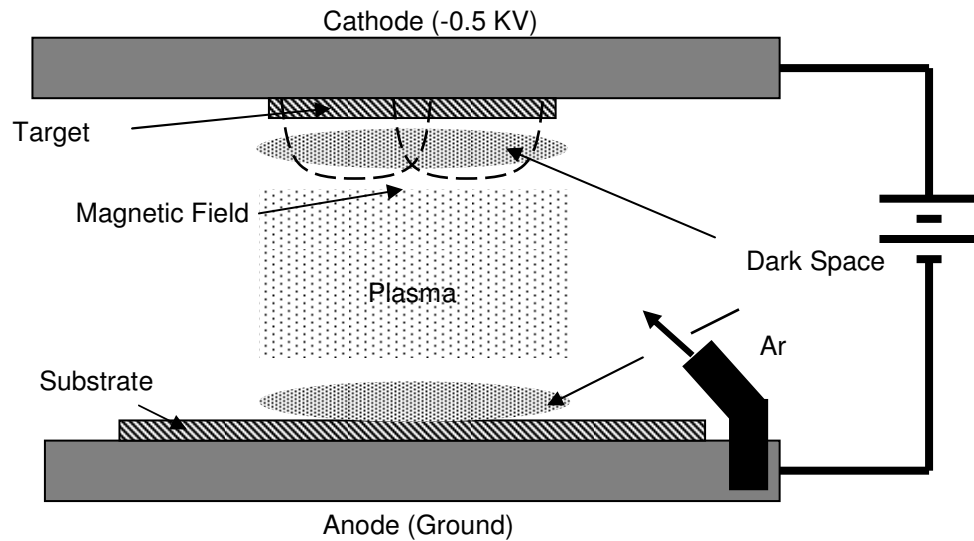
Figure 6. DC magnetron sputtering system layout.

A CRC-100 sputtering system was used here and can be operated either in DC or RF modes. The cathode/magnetron assembly is water cooled to help reduce the high target temperatures. Since tungsten was the only target used in this research, operation in DC mode was sufficient. If high resistance targets were needed, then RF mode would have been required. Insulating targets would require very high voltages because of their large resistivities. This can be overcome by using a RF source since target impedance will drop with increasing frequency. Therefore, high frequency plasmas can pass current through insulating targets the same way DC plasmas do through metal targets.

This particular system is contained by a cylindrical glass container that is 6" in diameter, and it requires targets that are 2" in diameter and about 0.125" in thickness.

20

The unit can also be operated in etch mode to pre-clean the substrate by reversing the bias on the electrodes. The pedestal, which holds the substrates to be coated, is located 5 cm from the target. Argon was used as the working gas and its flow inside the chamber is manually controlled with a leak valve. Due to the analog nature of the controls and the age of the equipment, some difficulties in attaining repeatability with gas flow and pressures were encountered. Discussions of some of the essential components that make up a planar DC magnetron sputtering system are in the following sections.

2.2.1 Glow Discharge Plasma

Energy input by non-thermal means is a powerful and widely used process in thin film deposition. The energy may be delivered by electrons, photons or ions, with ions being used in sputtering. Sputtering is a ballistic type process that will work on any material type, which eliminates the issue of high melting temperature materials. Since sputtering is a momentum transfer process, the bombarding ions must have energies exceeding chemical bond strengths, which are a few eV. Most energy enhanced techniques such as sputtering, involve the generation of a plasma, which is a partially ionized gas consisting of nearly equal concentrations of positive ions and negative particles (electrons and negative ions).

Plasma can be thought of as the fourth state in a progression of increasingly energetic states of matter, starting with solids having fixed atom positions. Adding energy to this first state allows the atoms to move around each other as a liquid and then to separate completely as a gas. Adding even more energy causes gas atoms to separate into the ions and free electrons of a plasma. Some familiar examples of plasma include stars, lightning, solar winds, neon signs and fluorescent tubes.

To begin the sputtering process, a discharge is initiated by the application of a sufficiently high DC voltage between metal electrodes immersed in a low pressure gas. The discharge represents a gaseous breakdown that may be viewed as the analog of dielectric breakdown in insulating solids. The process begins in gases when a stray electron near the cathode carrying an initial current is accelerated towards the anode by an applied electric field. The electron then collides with a neutral gas atom converting it into a positively charged ion. During this impact, ionization takes place and conservation of charge is maintained by releasing a second electron. The process continues by generating more ions and electrons and is represented in Figure 7.
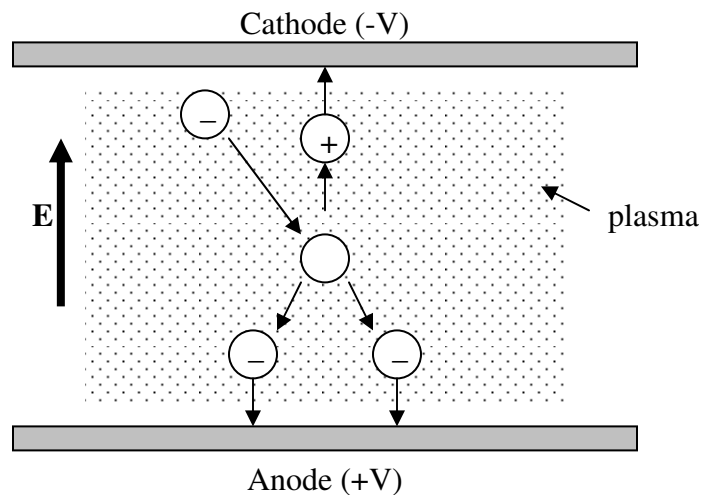
Figure 7. Ionization and current flow in a plasma sustained between electrodes.

The positive ions are attracted to the cathode where they collide with the target ejecting target atoms and secondary electrons. This effect snowballs until a sufficiently large current causes the gas to breakdown, creating a discharge that is self sustaining and the gas begins to glow. To operative in the domain for sputtering and other discharge processes such as plasma etching, the current is increased further after discharge and this

is called the abnormal discharge regime. For magnetron sputtering systems the plasma is able to be self sustaining at much lower pressures. The magnetic field creates a high concentration glow discharge near the cathode which allows for the working gas pressure to be as low as 10^{-5} torr.

For a DC discharge, it can be observed that there is a progression of alternating dark and luminous regions between the cathode and anode as shown in Figure 8. The general structure of the discharge has been known for some time now, but the microscopic details of charge distributions, behavior and interactions within these regions are not yet understood. The progression of regions starts with the Aston dark space. This first dark space is very thin and contains both low energy electrons and high energy positive ions with each moving in opposite directions. The cathode glow is just beyond it and appears as a luminous layer that envelops the cathode. De-excitation of positive ions through neutralization is the probable mechanism of light emission here. Next to the cathode dark space is a region of little ionization. The cathode dark space is also referred to as the cathode sheath and most of the discharge voltage is dropped across this region. The resulting electric field accelerates ions towards the cathode. Then, next to the cathode dark space is the negative glow region which is apparent due to interactions between assorted secondary electrons and neutrals with attendant excitation and de-excitation. Finally, the Faraday dark space, the positive column and anode then follow, but during sputtering the substrate is typically placed inside the negative glow region so the Faraday dark space and positive column normally are not apparent.

23
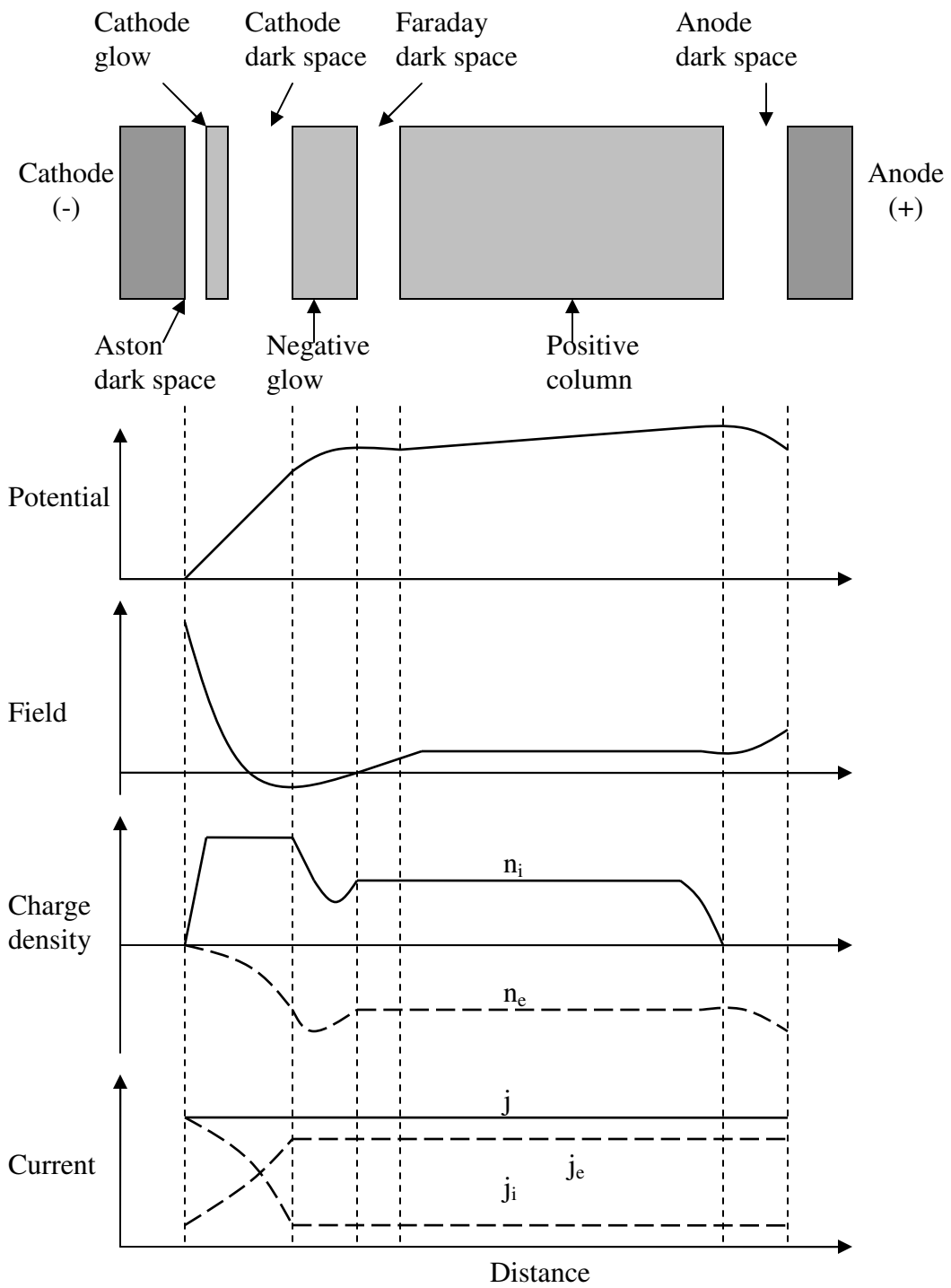
Figure 8. Structure of DC glow discharge [11].

24

2.2.2 Magnetic Field in Sputtering

The benefits of a magnetron sputtering system over a basic DC sputtering system are the result of combining magnetic and electric fields. This combination leads to higher sputtering rates and reduced substrate temperature. By superimposing a magnetic field perpendicular to the electric field, greater electron confinement is achieved. The ideal electric and magnetic field directions to confine electrons near the cathode surface are shown in Figure 9. The combination of an electric and magnetic field results in increased ionization close to the cathode which leads to higher levels of current drawn in a magnetron system compared to a DC system at the same applied voltage. With a larger current being drawn, higher sputtering yields are achievable. In addition to producing higher currents, by confining electrons around the cathode surface with the magnetic field, fewer electrons and ions are accelerated towards the substrate which reduces substrate temperature and thermal stresses.
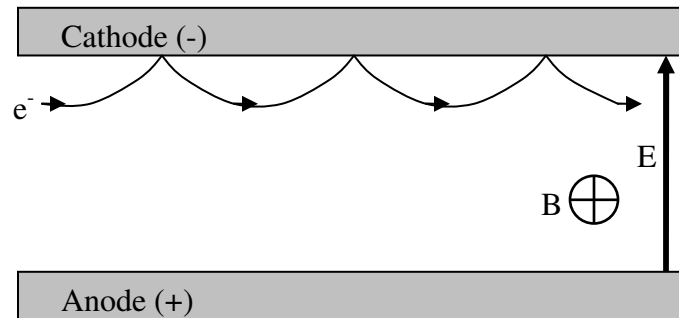
Figure 9. Effect of electric and magnetic fields on electron motion.

Another important advantage of a magnetron system is the capability of reduced operating pressures. The lower limit of operating pressure is based on the need for ejected electrons from the cathode to undergo enough ionizing collisions with the ambient gas to sustain a plasma. If the electrons escape the magnetic field they will more

25

than likely reach the anode and be removed before making any collisions with the ambient gas. With a magnetron system, the electrons have a longer path length before they can escape to the anode due to their orbital motion. The increased electron path length will increase the chances of electrons colliding with the working gas to produce ions. The effects of the magnetic and electric fields on electron motion can be observed in Figure 10. For simplification the magnetic and electric fields were drawn parallel to each other to show the helical orbits of escaping electrons. The ideal situation in a magnetron system would be to have the magnetic field perpendicular to the electric field everywhere across the cathode. But due to the circular magnets used in the system here, the magnetic field is not exactly like the ideal situation and some electrons will escape the magnetic field and reach the anode.
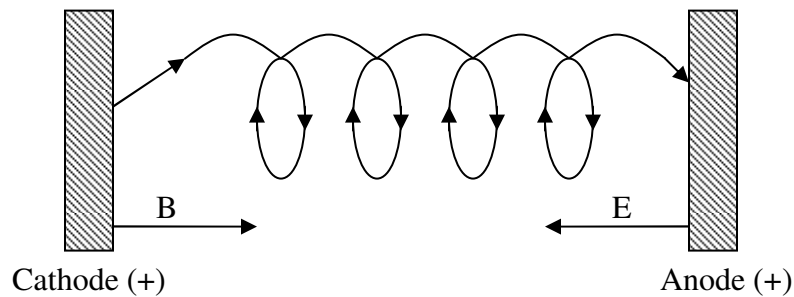
Figure 10. Helical orbit caused by the magnetic and electric fields.

The magnetron configuration used in the current research was a planar configuration. A planar configuration means that the cathode and anode surfaces are aligned parallel to each other. To create the magnetic field, small circular ring permanent magnets are placed on the back of the target. A schematic of the planar magnetron system is depicted in Figure 11. The figure is a cross section view of the real system, so the figure must be revolved 180° to represent the true system layout.
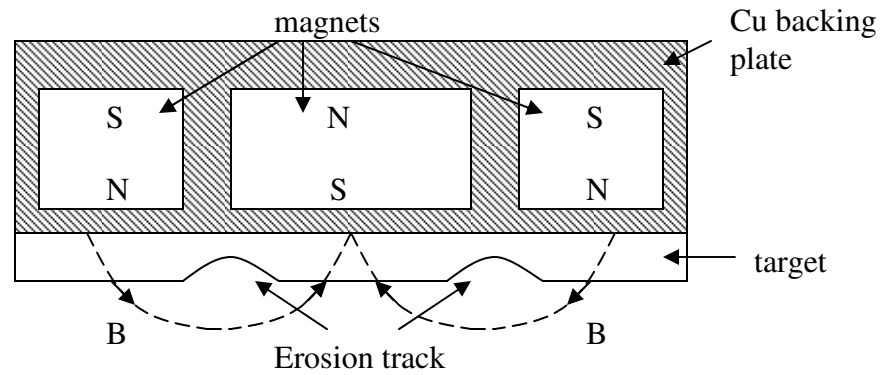
Figure 11. Planar magnetron setup with circular magnets.

Because of the magnetic and electric fields not being perpendicular everywhere across the cathode's surface, electrons will hop around the target plane, which induces a local current of electrons. This creates a region of high density plasma leading to higher sputtering rates in these areas and non-uniform erosion of the target. The non-uniform erosion observed in a circular planar magnetron is often described as a racetrack pattern in the target [22, 23]. The etch rate in the region of the racetrack is so high that the etch rate caused only by the electric field in the surrounding areas is usually ignored. Because film thickness uniformity is important, the surface of the target was scanned to better understand any effects that might be observed in film thickness profiles taken later. The erosion track of the tungsten target was measured using a Tencor P-20h profilometer. The profile of the surface was started at the center of the target, moving to the outer edge. Results from this scan can be observed in Figure 12. The erosion track on the target was measured to have a maximum depth of 230 μm at 1.6 cm from the target center. It is clearly seen in Figure 12 that nearly all of the sputtered material is from erosion track, which will limit the life of the target.

27
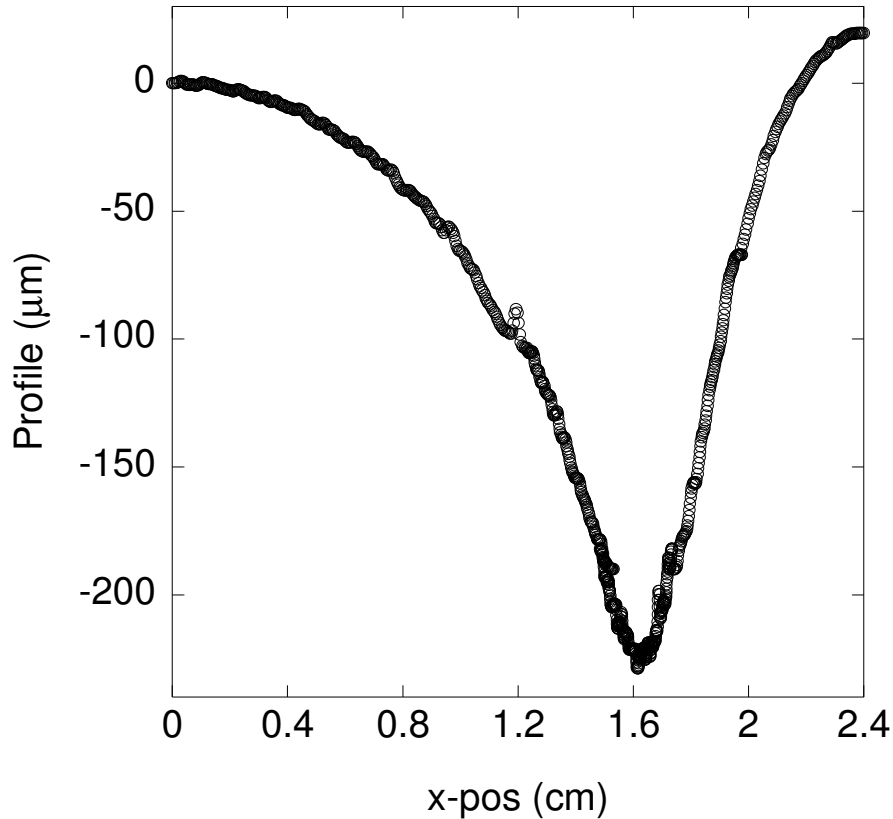
Figure 12. Profile of tungsten target erosion.

Turner et al. have observed that the sputtering rate and erosion profile may vary by a factor of 10 across the radius of the target due to the magnetic field profile used in a circular magnetron system [29]. They determined that the radial sputtering profile is primarily determined by the sheath thickness and that the uniformity of the sputtering profile increased as sheath thickness was decreased. It was also observed that the width of the radial sputtering profile decreased with an increasing magnetic field strength. Caution must be used when depositing films with a system configuration similar to the one shown in Figure 11, because the non-uniform sputtering of the target will lead to poor utilization of the target and non-uniform film thickness [29-33].

Film thickness uniformity over a large area is a basic demand in thin film technology. Therefore, profiling the sputter deposited tungsten film thickness was a

28

necessity. To accomplish this task, a 4" silicon wafer was centered in the middle of the substrate holder and was sputtered with tungsten for 60 min. Two different runs were performed to obtain the film thickness uniformity in the radial and circumferential directions. For both runs the current was set at 100 mA, the voltage was at 500 V and the gas pressure was approximately 4 millitorr. Glass slides were placed on top of the wafers in two different orientations covering the wafer from the center to outer edge (Figure 13). After film deposition the glass slides were removed and a profilometer was used to measure the film thickness. Step height measurements were taken in 2 cm increments.
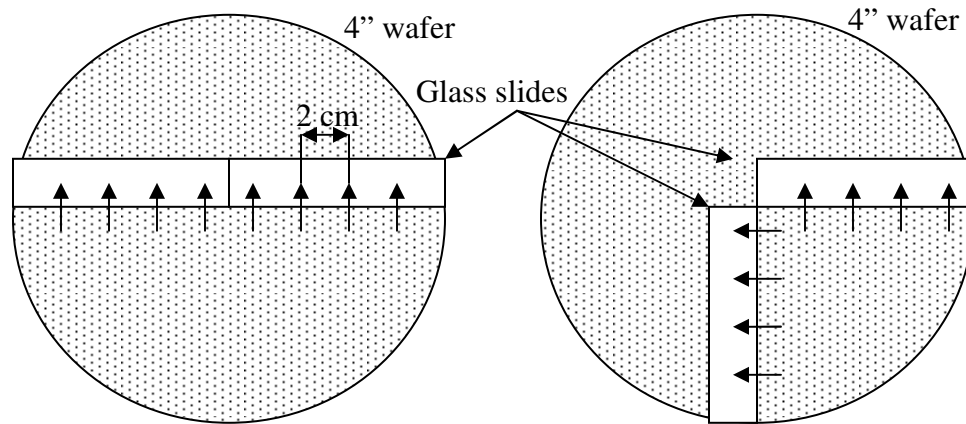
Figure 13. Setup for measuring the film thickness profile.

The results of the thickness profile taken across the diameter of a 4" wafer in 2 cm increments are plotted in Figure 14. The discontinuity in film thickness on the left hand side about 12 cm out from the center is probably not an effect of the sputtering system, but of the measurement process. The likely explanation for the discontinuity is that a shift must have been made with the wafer while taking the thickness measurements with the profilometer. There is a significant change in film thickness from the center of the wafer to almost the outer edge. In Figure 14 there was a maximum film thickness of

29

8580 Å at the wafer center and a minimum film thickness of 4580 Å at the outer left edge. That is approximately a 47 % difference in film thickness from the center of the wafer to the outer edge. In addition, there is approximately a 24 % difference in film thickness between the opposite edges of the wafers. The difference in edge thickness could be caused by the location of working gas in the chamber. The argon is introduced on one side of the chamber just above the height of the pedestal. This could produce a non-uniform flux in that location having an effect on sputtering rate and gas collisions.
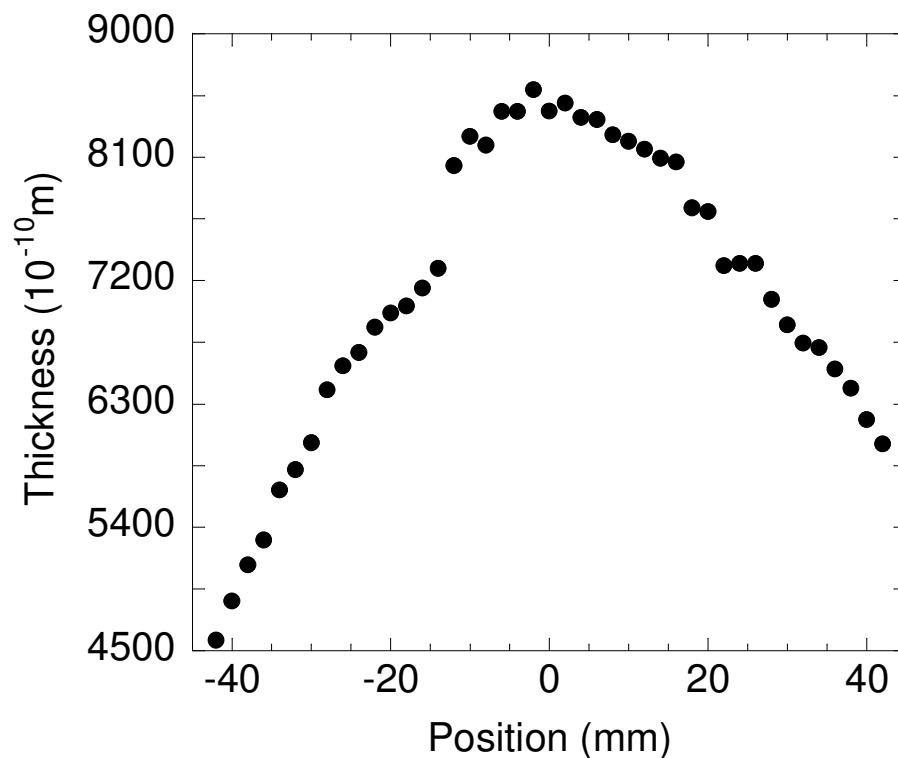
Figure 14. Film thickness measured across the diameter of the wafer.

The results of the film thickness measurements taken across the radius of a 4" wafer at a 90° orientation to each other are plotted in Figure 15. For this run there were no major discontinuities noticed like those in Figure 14, however there was still a significant change in film thickness from the center of the wafer to the outer edge. A maximum film thickness of 8260 Å was measured at the wafer center and a minimum

30

film thickness of 4550 Å at the outer edge. The percent difference in film thickness

between the center and outer edge of the wafer was calculated to be 45 % in this case.
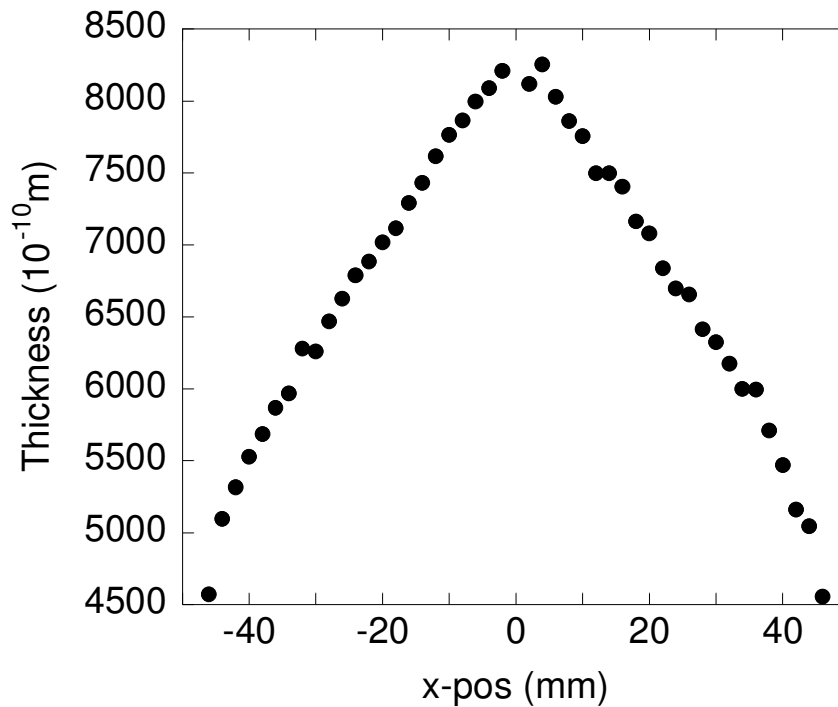
Figure 15. Film thickness measured in two radial directions.

The second run is a more likely indicator of the expected thickness profile

because no discontinuities in film thickness were noticed. There is a consistent trend

noticed from both of the runs which shows a significant change in film thickness across

the wafer diameter. With the maximum film thickness located in the center and the

minimum located at the wafers' outer edge. The 45 % difference in film thickness

between the center and outer edges of the wafer was larger than what was expected. A

theoretical thickness profile was calculated from observations made from the erosion

track profile in Figure 12, the sputtering system geometry and assuming a cosine

distribution [21, 34] for the direction of the sputtered atoms. Figure 16 is a plot

comparing the expected and experimentally measured thickness profile across a 4" wafer.

31

The film thickness has been normalized to be able to compare the two sets of data. The theoretical film profile resulted in a 33 % difference in film thickness from the center to the outer edge of a 4" wafer as opposed to the 45 % difference measured experimentally.
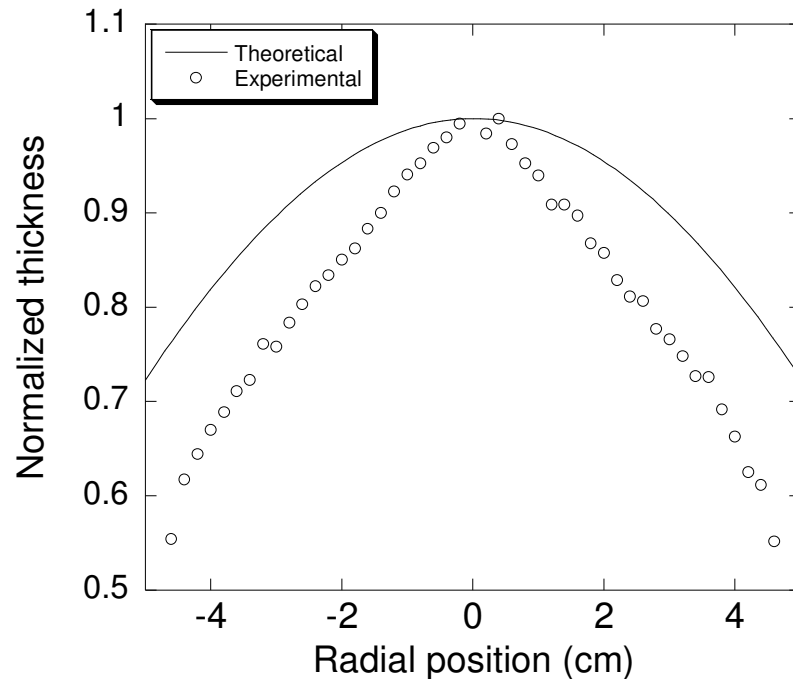
Figure 16. Predicted film thickness profile.

To calculate the theoretical profile, 100 % of the maximum value for the sputtering yield was applied to the radial position of the target between 1.1 and 1.8 cm. The sputtering yield was reduced as the radial position on the target decreased to match up the experimental profile measured from the used tungsten target. A more detailed explanation of the theoretical calculation can be found in Appendix A. The difference in the predicted thickness profile in Figure 16 and the experimentally observed profiles in Figure 14 and Figure 15 is probably the result of the assumptions made for the theoretical calculation. In order to simplify the calculation, it was assumed that target surface was perfectly flat, no collisions between the sputtered atoms and the ambient gas were taking place and there was no mobility of the sputtered atoms on arrival at the film surface. The

32

target surface will definitely affect the film thickness profile by obstructing the path of sputtered atoms. It can be expected that the erosion track will continually change over time. As the track gets deeper, the walls of the trench will block even more atoms sputtering out at larger emission angles. The film thickness and target profiles were taken after approximately 1 month of target use. It is unclear what the film thickness profile was for a flat target and how the deposition profile depends on target geometry.

Hong et al. have reported similar results using a planar circular type magnetron sputtering system in their experiments [31] as compared to the experimentally measured results here. In their experiments they sputtered a 2" target of chromium using a system of similar dimensions. When their substrate to target distance was 5 cm, they noticed a 25 % difference in film thickness between the center of the wafer and 3 cm out. Their results confirm what was plotted in Figure 14 and Figure 15. Furthermore, as they increased the distance between the substrate and the target they were able to get a more uniform film thickness across the diameter of the wafer.

Fancey's findings are also in agreement with Hong, where an increase in the distance between the target and the substrate will increase the film thickness uniformity [32]. An increase in target to substrate distance will increase the significance of gas scattering effects, therefore improving uniformity. However, it should be noted that by increasing the target to substrate distance, deposition rates may decrease and there may be some unwanted effects on film properties and microstructure. An alternative method for improving film thickness uniformity have been accomplished by Hong et al. by inserting a mesh into the chamber to enhance the scattering of gaseous atoms [33]. However, the most common method for achieving film thickness uniformity is by wafer

33

rotation. This is a frequent industry practice when a high level of film thickness uniformity is required.

2.3 Gas Pressure Effects

The working gas pressure is one of the most influential parameters in sputter deposition. Deposition rate, film uniformity, particle energy and residual stress are all dependent on the working gas pressure. This is due to the fact that gas pressure has a direct effect on the transport behavior of the sputtered atoms and back-reflected particles through the ambient gas. Predicting this transport process is very complex and has been attempted by many through the use of Monte Carlo models. These models have been used to simulate the transport of sputtered atoms and predict the effects on sputtered atom's energy, angular distribution and deposition uniformity [22, 24, 29, 30].

The first parameter tested here was the effect of argon gas pressure on the tungsten deposition rate. Argon gas pressure was tested in the range of 4 to 10 millitorr and the resulting deposition rates are given in Table 2. A minimum deposition rate of 80 Å/min was measured at an argon pressure of 4 millitorr, and it was found to increase to 123 Å/min when the pressure was increased to 10 millitorr.

Table 2. Effects of argon pressure on the deposition rate of tungsten films.

Time (min)	Current (mA)	Voltage (V)	Pressure (millitorr)	Deposition Rate (Å/min)
60	100	500	4	80
60	100	500	6	90
60	100	500	10	123

Comparable results have been reported by Nakano et al., who observed that in a DC system, the deposition rates of Al, Cu and Mo were proportional to an increasing gas pressure up to a maximum deposition rate found around 7.5 millitorr. The deposition rate

then decreased as gas pressure was increased beyond 7.5 millitorr [30]. The dependence of deposition rate on gas pressure can be attributed to two factors: 1) a change in target current and 2) a change in the thermalization profile. The effective electrical current density at the target, j, which is proportional to the etch rate, can be expressed as

$$j = n_e \cdot q \cdot \overline{v} \tag{9},$$

where n_e is the electron concentration, q is the electron charge and $\overline{v}$ is the electron velocity. The increasing gas pressure will initially increase the electron concentration which in turn results in more atomic ionization. The increase in ionization effectively increases the etch and deposition rates. A transition point in deposition rate will then be reached when the frequency of collisions between sputtered atoms and ambient gas is increased.

Both experimental and simulation results report a transition point that depends on the atomic mass of the target [30]. The atomic mass affects this transition point because the mass of the target atoms will determine how far the atoms travel before thermalization occurs. Thermalization in a plasma is when the high energy sputtered atoms and reflected Ar atoms reach thermal equilibrium with the ambient environment, this is achieved by collisions in the plasma. The distance for thermalization to occur is proportional to the target's atomic mass. At lower pressures, regardless of the target material, most of the sputtered atoms are still able to make it to the substrate with significant amounts of energy and there will be an increase in deposition rate up to the transition point. As gas pressure increases, so will the frequency of collisions between sputtered atoms and the ambient gas. As gas pressure continues to increase, there is a reduction in the mean free path of collision for the sputtered atoms. This results in the

35

thermalization profile converging on the target and at this point the deposition rate has hit its maximum and will start to decrease.

So far, the effects of collisions between sputtered atoms and ambient gas on film thickness uniformity and deposition rates has been discussed. The collisions can also be credited with playing a role in the existence of residual stresses. Many authors have reported the effects of gas pressure on residual stress in the sputter deposition of thin films [35-42]. Initial work on residual stress in thin films was motivated by the need to explain why cracks were observed in chromium thin films sputtered onto plastic automotive parts. Hoffman and Thornton were at the head of this research and produced many publications in this area during the 1960s and 1970s. Their research focused on the effects of sputter deposition on the microstructure of thin films and the causes of residual stress. Their findings showed that the residual stress in sputtered films had a strong dependence on the working gas pressure. Lower working gas pressures resulted in highly compressive residual stresses, up to 2 GPa [37]. As the gas pressure increased there was a sharp transition from compressive to tensile residual stresses over a small pressure range. If the gas pressure continued to increase, the tensile residual stresses would start to decrease in magnitude.

The results in Table 3 summarize the effects of argon pressure on residual stresses in sputter deposited tungsten films. All sputtering parameters other than gas pressured remained constant to ensure the test consistency and to separate out the effects of changing gas pressure on residual stress. The reported stress values in Table 3 were calculated using a curvature method that will be outlined in Chapter 3.

Table 3. Effects of argon gas pressure on tungsten residual stress.

Pressure (millitorr)	Stress (MPa)	Current (mA)	Voltage (V)	Time (min)
2	Delamination	100	500	60
4	-1500	100	500	60
6	-500	100	500	60
10	1000	100	500	60

The residual stresses measurements listed in Table 3 confirm what was reported by Hoffman and Thornton: substantial amounts of compressive residual stress are present in sputtered films at low working gas pressures and a transition to tensile residual stress was measured at higher working gas pressures. Figure 17 shows the quick transition from compressive to tensile residual stress over a short range of argon pressure. Reducing the argon pressure below 2 millitorr was challenging because it was difficult to maintain a plasma discharge and film delamination from the substrate was common. The 2 GPa of stress at 2 millitorr Ar pressure is only an estimate chosen by following the observed relationship of stress and gas pressure. Delamination of the tungsten films at approximately 2 millitorr was unavoidable. Gas pressures above 10 millitorr were not tested because the intended future use of the tungsten films required them to be in compression. Later, compressively stress tungsten films will be used in the superlayer indentation test for calculating film/substrate interfacial toughness and for forcing film delamination to create microchannels. Therefore, for the Ar pressure tests here, it was only necessary to know the transition point between compressive and tensile residual stresses.

37
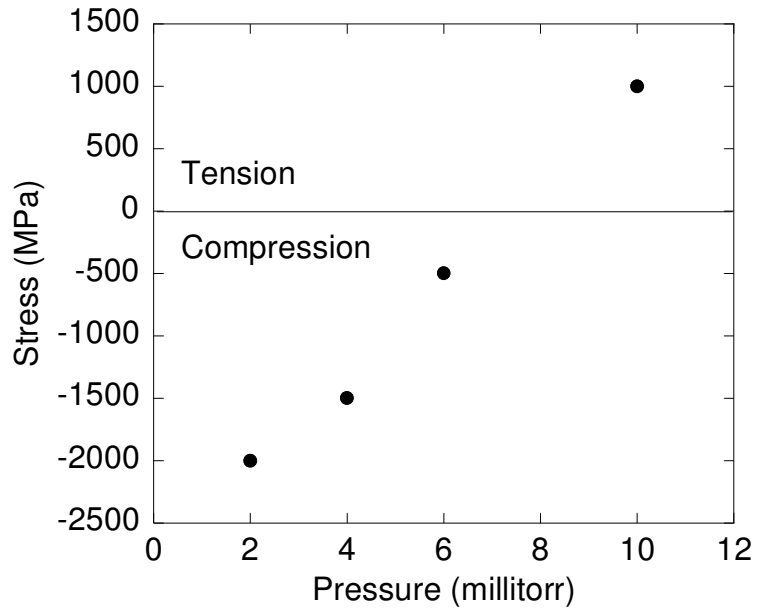
Figure 17. Residual stress dependence on argon pressure.

A summary of the Hoffman and Thornton findings can be found in Figure 18. There is a similar trend noticed in the results here and in Figure 18 a). It can be observed that at lower argon pressures the deposited films are in compression and then there is a quick transition to tensile stresses as the argon pressure increases. The transition point for tungsten with argon as the working gas was measured to be about 3 millitorr less here, than what was reported by Hoffman and Thorton (Figure 18 b)). The differences in transition points between their findings and the results here can be attributed to different sputtering system configurations and current and voltage settings [41]. An increase in voltage and current leads to reflected species with higher energies. Increases in current are more substantial with a cylindrical magnetron than compared to a planar magnetron and this would account for the lower transition pressure noticed here.

38
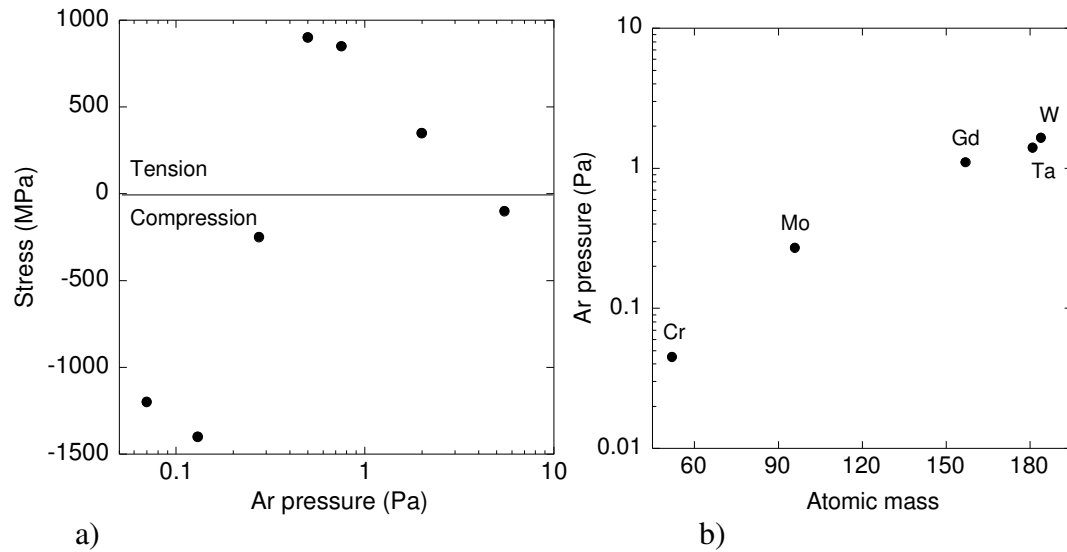
Figure 18. Hoffman and Thornton findings: a) Residual stress of Cr films b) Transition points for various targets (Graphs reproduced from [36, 37]).

Compressive stress at low gas pressures is primarily attributed to atoms and back-reflected neutral gas atoms reaching the substrate with substantial amounts of kinetic energy. As gas pressure is reduced, the gas scattering is reduced resulting in an increase of the normal flux component and the particle energy striking the film. This suggests an impact that is sufficient enough to disturb the previously condensed material, packing it together by "atomic peening". This atomic peening, or forward sputtering theory, suggests that atoms are displaced from their equilibrium positions through a series of primary and recoil collisions. As the collisions continue, the equilibrium positions are changed, resulting in a volumetric distortion.

Convincing evidence to support the idea of atomic peening was conducted by Hoffman and Gaerttner [43]. They measured the residual stress in evaporated chromium films, which had a unique system setup that allowed for the evaporation of chromium and introduction of an ion beam simultaneously. Normally evaporated films exhibit tensile residual stress, which is comparable to conditions observed in sputter deposition at high

gas pressures. During film deposition, Hoffman and Gaerttner simultaneously bombarded the film with a beam of accelerated inert gas ions. The independent control of metal and inert gas ions impinging upon the growing films enabled investigation of the influence of bombarding ions. They observed that with the addition of the ion beam, compressive residual stresses were present in the evaporated chromium films. The addition of the ion beam mimics conditions that would be expected in low pressure sputtering where a majority of the sputtered and back-reflected gas atoms reach the film with substantial amounts of energy. This suggests that the presence of compressive stress in sputtered films is a momentum and energy driven process.

Tensile stress will be expected in sputtered films at higher gas pressure due to the increase in collisions taking place in the ambient gas. As the gas pressure is increased during sputtering, gas scattering increases leading to a more significant oblique component of the particle flux. An increased oblique component will result in the particle energy and flux being attenuated. When the particle energy is fully reduced by gas scattering, thermalization has taken place. The terminal energy of a sputtered atom is predominately determined by the product of the gas pressure and target to substrate distance [25]. For most sputtering systems the minimum distance between the target and the substrate is 5 cm, which corresponds to nearly all the sputtered and back-reflected particles being thermalized at a sputtering pressure above 7.5 millitorr. An argon pressure of 7.5 millitorr was observed to be the transition pressure for tungsten in Figure 17.

As thermalization increases, there will be a transition between compressive to tensile stress. The sputtered atoms and back-reflected gas ions and neutrals will have

40

reduced amount of energy due to collisions with the ambient gas. This dramatically reduces the atomic peening effect that resulted in compressive stresses at lower gas pressures. Reduced energy in the sputtered atoms means that as the atoms reach the substrate surface, they will have less atomic mobility. As the film growth progresses through morphological stages (isolated atomic clusters, nuclei, island film, continuous film), interatomic attractive forces acting across the gaps between contiguous grains cause an elastic deformation of the grain walls. The grain boundary deformation is balanced by the intragrain tensile forces imposed by the constraint exerted by the adhesion of the film to the substrate. Hoffman and coworkers [44, 45] have related the intragrain strain energy to the difference in the surface energy of the adjacent crystallites and the energy of the resultant grain boundary. They proposed that the elastic strain, ε, in the film is related to the unstrained lattice constant, a, and the variation of the lattice constant, $(x$-$a)$, or to Δ and d which are the grain boundary relaxation distance and the final grain size, respectively. The elastic deformation, ε, is responsible for the macroscopically observed tensile stress, σ, which is given by

$$\sigma = \frac{E}{(1-v)} \cdot \varepsilon = \frac{E}{(1-v)} \cdot \frac{x-a}{a} = \frac{E}{(1-v)} \cdot \frac{\Delta}{d}$$

(10),

where E and ν are the film's Young's modulus and Poisson's ratio, respectively.

As the working gas pressure is increased further, the low energy sputtered atoms continue to produce tapered columnar structure growing side by side but separated by deep crevices and micropores [47-49]. The result of the tapered columnar structure is a less dense, discontinuous film that cannot support lateral tensile stress and that is why there is a reduction in tensile stresses at high gas pressures in Figure 18. In addition to the tensile stresses usually found in films sputter deposited at high gas pressures, because

41

of the tapered columnar structure, the films tend to have less optical reflectance and higher resistivities [40, 41].

2.4 Film Structure

Previously stated, there are primarily three steps in making a film. A source of film material is provided, the material is transported to the substrate and then the final step is deposition. So far the first two steps have been covered in relation to DC magnetron sputter deposition. The third step will now be discussed and a connection will be made with its effect on film structure. A thorough understanding of this step must be acquired because the film structure directly affects the thin film properties.

The process starts with the deposited atoms colliding with the substrate surface and starting off as isolated atomic clusters. The clusters will begin to coalesce to form larger islands and then the islands will join to form a film. The efficiency of the atoms to stick together will determine the microstructure. Figure 19 helps to define the different microstructures commonly observed when using PVD processes. One axis of the graph is the ratio of substrate temperature, T, to film melting temperature, T_m, and the other axis is the working gas pressure. Normally at low deposition temperatures the mobility of arriving atoms is limited. Therefore, the resulting film is expected to be less dense, with columnar growth structures separated by voids. This type of structure would account for zone 1 in Figure 19, consisting of tapered columns with domed tops defined by voided growth boundaries. As the temperature increases, the columns increase in width and are defined by metallurgical grain boundaries and this is zone 2 of Figure 19. The high temperature zone 3 of Figure 19 has a structure that consists of equiaxed grains, which increases in size in accordance with activation energies typical of bulk diffusion.

42
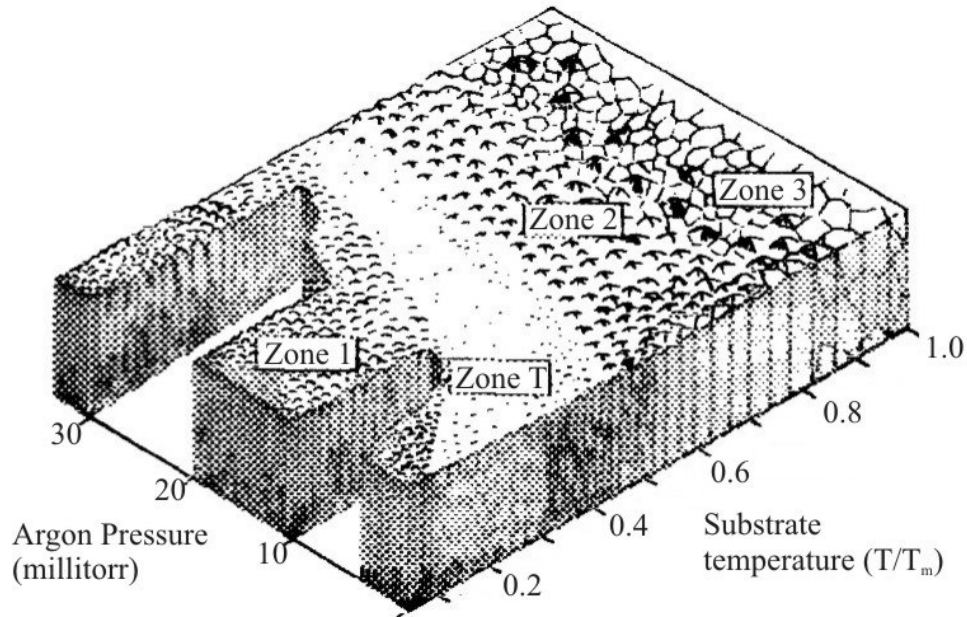
Figure 19. Microstructure zones from sputter deposition (Schematic reproduced from Thornton [47]).

The trend in device fabrication towards lower processing temperature means that coatings will often be deposited at substrate temperatures that are relatively low compared to the coating material melting point. Normally, this would lead to zone 1 columnar growth structure with voids and would be undesirable because this type of structure tends to have an anisotropic character in terms of magnetism and lateral current transport [50]. But for magnetron sputtering, where low working gas pressures are used, sputtered atoms reach the surface with high energies in the 10 – 40 eV range. These high energies lead to increased atomic mobility and the result is a denser film with smaller columnar grains represented by zone T in Figure 19. Along with the increased atom mobility, the atomic peening effect also plays a role in producing denser films.

To get a better picture of the effects of argon pressure on film properties surface, topography scans of sputter deposited tungsten films were taken and are presented in

43

Figure 20. It is observed that there are no noticeable differences in topography for the tungsten films deposited at 4 and 10 millitorr. Both films are thought to be representative of zone T in Figure 19 and were measured to have a surface roughness around 2 nm. The small oval shaped domes that are seen in Figure 19 are thought to be the tops of small densely packed columnar structures and were measured to be about 300 nm in width.
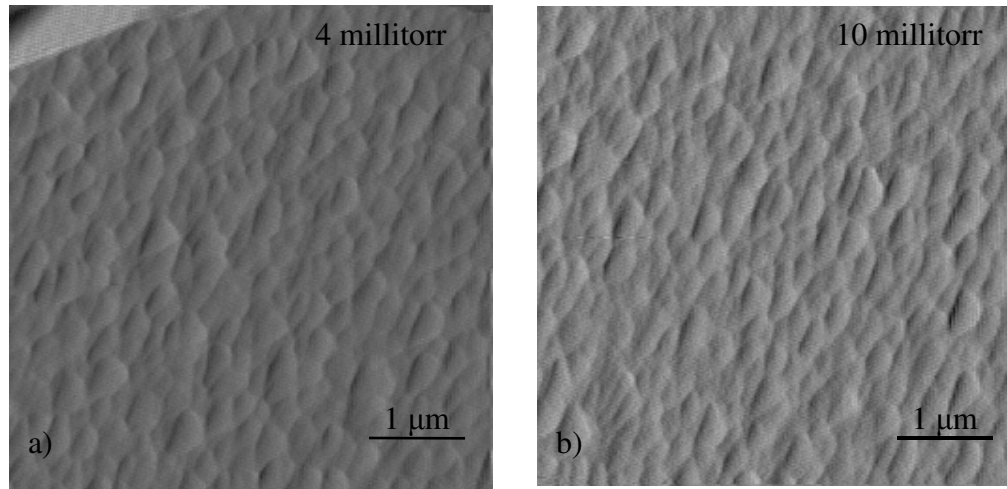
Figure 20. Surface scan of sputter deposited tungsten films; a) Argon pressure of 4 millitorr b) Argon pressure of 10 millitorr.

Topographic images of the two tungsten films did not reveal any noticeable difference between the films. Therefore, to further examine the tungsten films, it was necessary to test the mechanical properties of the films using nanoindentation. A test method was setup that performed a total of 40 indents per sample in different locations and varying loads. The method consisted of indenting each sample in 5 different locations across a 1 cm^2 area. Eight indents were performed at each location in a two rows by four columns pattern, with six microns separating each indent. The indentation load was varied between 1000 and 8000 µN with the loading segment times held constant at 10 seconds.

44

After examining the indentation results it was immediately noticed that there are slight differences in the load-displacement curves of the two tungsten films (Figure 21). The two indents shown in Figure 21 were performed to the same maximum load, with all the same loading conditions, but the indents reached different maximum depths. The tungsten film deposited at 10 millitorr argon pressure had a final indentation depth about 10 nm deeper than the tungsten film deposited at 4 millitorr argon pressure.
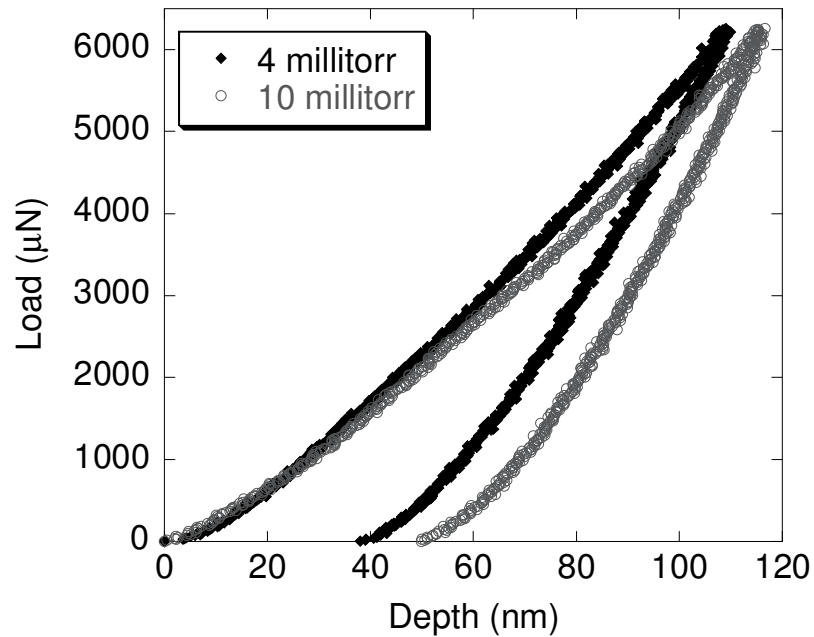
Figure 21. Comparison of the load-displacements curves for tungsten films deposited with different argon pressures.

Since there was a difference in final indentation depth, a difference in hardness of the two films would be expected and was measured (Figure 22). Hardness is calculated by knowing the maximum load P_{max}, and dividing it by the contact area of the indenter tip A_c:

$$H = \frac{P_{\max}}{A_c} \tag{11}.$$

45

Since the contact area will be a function of the depth of the indenter tip, it is understandable to see a difference between the two tungsten films after observing the difference in load-displacement curves. The tungsten film deposited at 4 millitorr was measured to have an average hardness 4 GPa higher than the 10 millitorr film. This difference in hardness is the result of different energies for the bombarding atoms and ions of the two films. The lower pressure film would be expected to see higher energy atoms and ions colliding with the surface causing more atomic peening of the film. This data could be beneficial if an application required a higher hardness film, but it also comes with the consequence of high amounts of compressive residual stress.
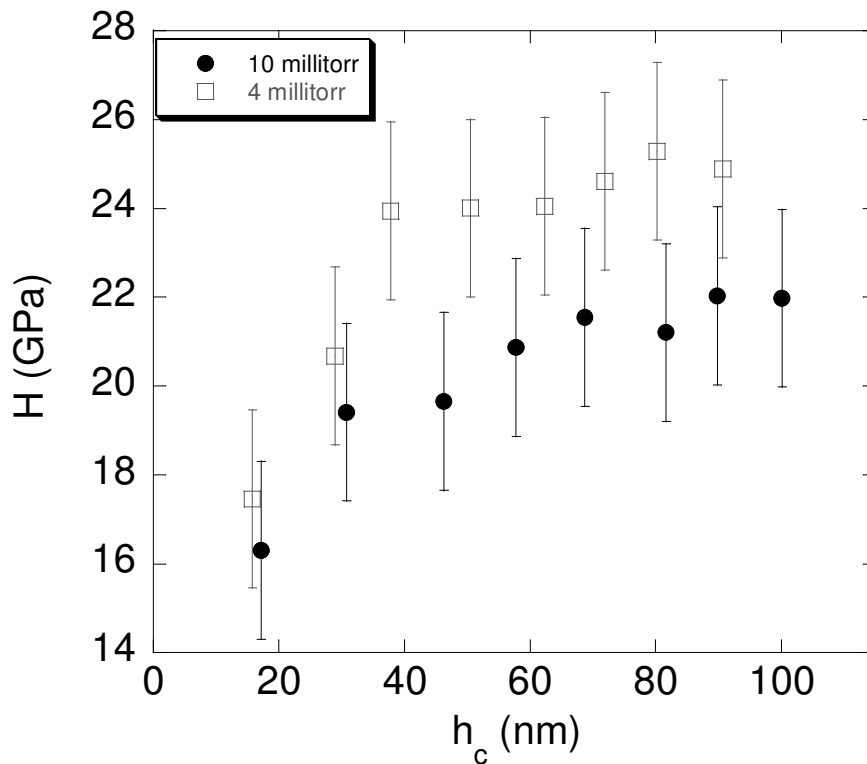
Figure 22. Hardness of tungsten films deposited at different argon pressures.

Along with hardness measurements the stiffness and modulus of the films were tested. Stiffness is plotted in Figure 23 and is defined as the change in load divided by the change in depth:

46

$$S = \frac{dP}{dh} \tag{12}.$$

The stiffness of both tungsten films matched up and showed no dependence on the argon pressure. Since the stiffness of the films was comparable, it's expected that the reduced modulus measured as a function of the indent depth, would also show no significant differences for the two tungsten films (Figure 24). The reduced modulus E_r can be expressed as the following:

$$E_r = \frac{\sqrt{\pi}}{\gamma \cdot 2} \frac{S}{\sqrt{A_c}} \tag{13},$$

where γ is a correction factor that depends on the strain imposed by the indenter and the Poisson's ratio of the sample. The reduced modulus takes into account any compliance of the indenter and it can be related to the sample's modulus by the following expression:

$$\frac{1}{E_r} = \frac{(1-v_s^2)}{E_s} + \frac{(1-v_i^2)}{E_i} \tag{14},$$

where E_s and v_s are the elastic modulus and Poisson's ratio for the sample, respectively. E_i and v_i are the same properties, but for the indenter tip which is usually diamond. Both films were measured to have a maximum reduced modulus of approximately 230 GPa for contact depths between 20 and 40 nm. The reduced modulus then decreased as a function of the contact depth to a minimum value of approximately 215 GPa at contact depths around 100 nm for both films.

47
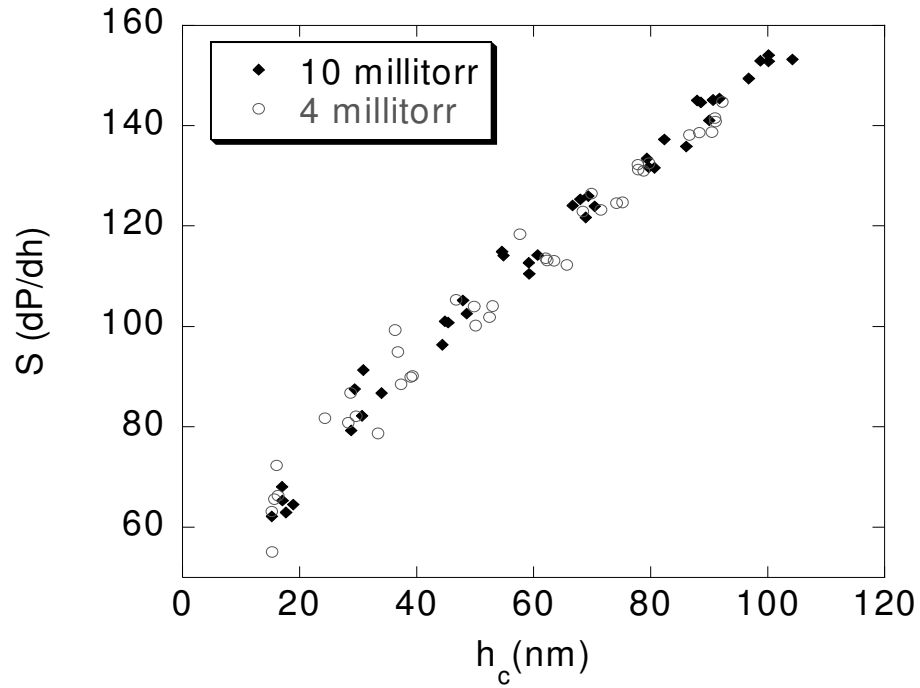
Figure 23. Stiffness of tungsten films deposited at different argon pressures.
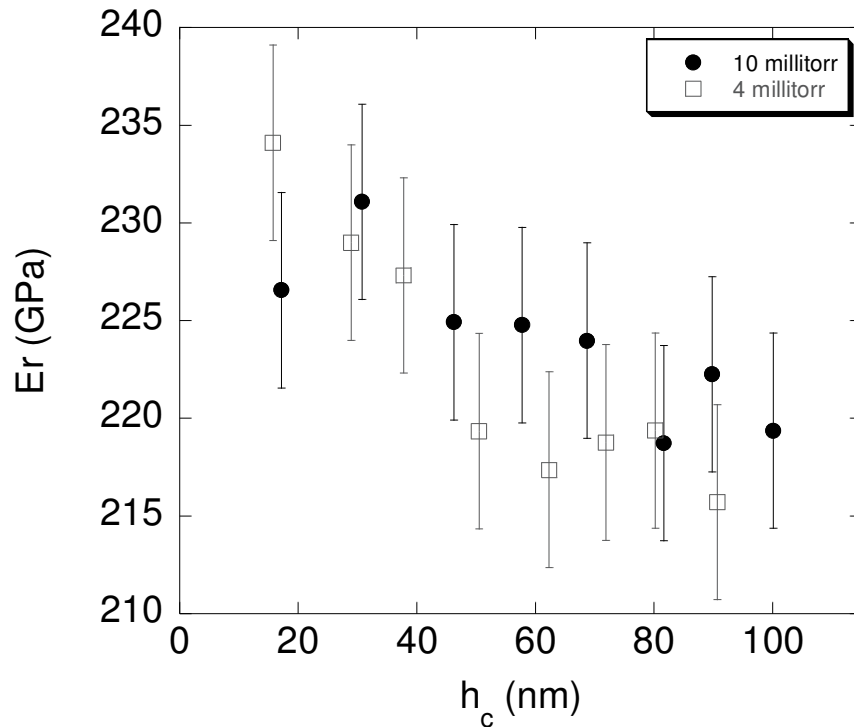
Figure 24. Reduced modulus of tungsten films deposited at different argon pressures.

48

The large variation in hardness and reduced modulus for both of the tungsten films in Figure 22 and Figure 24 is primarily thought to be the result of the sputtering system used. A dynamic environment exists inside of a DC magnetron sputtering system. Factors such as a non-uniform magnetic field, will lead to non-uniform sputtering rates, film thicknesses and particle energies across the sputtering target and substrate. These non-uniformities mean that this system is difficult to predict and it will be expected to see variations in film microstructure and residual stress across the area of a wafer. Some of the data variance at the shallower indentation depths is the result of the measurement technique and will be discussed later.

2.5 Summary of Sputtering Results

The basics of sputtering have been covered here, with more specific details focused on DC planar magnetron sputtering. Similar to other types of film deposition, sputtering has its advantages and disadvantages. One major advantage of this deposition method is that sputtering is not limited to one type of deposited material. Depending on the type of power source used, sputtering can deposit insulating materials and refractory metals that are normally a challenge for other deposition methods. By using magnetron sputtering, film deposition rates are relatively high and deposition temperature can be kept low. The disadvantages of magnetron sputtering should not necessarily be thought of as disadvantages, but things to be aware of. If film thickness uniformity is a major concern, special care must be taken in choosing the appropriate system setup and geometry. Options such as rotating the substrate/substrates, changing the anode to cathode distance, adjusting the magnetic field and inserting meshes are all possibilities

49

for improving film thickness uniformity. Depending on the system configuration, film thickness has been observed to vary by 45 % across the radius of a 4" diameter wafer.

It has been shown that working gas pressure affects the deposition rate, residual stress and microstructure of a film. The gas pressure influences the transport behavior of sputtered atoms through the ambient gas and onto the films surface. If gas pressures are low, there will be fewer collisions in the ambient gas. This allows for more energy upon impact of the film, resulting in denser films that will typically be in compression. The main theory behind the introduction of compressive stress at low sputtering pressures is atomic peening. When the gas pressure is low, sputtered atoms and back-reflected gas particles will reach the film surface without losing significant amounts of energy to collisions in the ambient gas. The high momentum/energy impacts result in an atomic packing of the film.

As gas pressure increases, there will be more collisions of the sputtered atoms and back-reflected gas particles with the ambient gas, resulting in less dense films that will typically be in tension. The arriving atoms have less atomic mobility resulting in a tapered columnar film structure, which is filled with micropores and voids separating the columns.

Chapter 3

Residual Stresses in Thin Films

3.1 Thin Film Residual Stress

Desirable or not, internal or residual stress is almost always going to be present in thin films. Stress may be present in thin films whether or not external loads are applied and may be due to a variety of reasons that are introduced during film deposition, which include: differential thermal expansion of the film/substrate, mismatches between the lattice parameter of the film and the substrate, atomic peening, incorporation of foreign atoms, microscopic voids, variation of interatomic spacing with crystal size, recrystallization processes, crystallite coalescence at grain boundaries and phase transformations [50-52]. To clarify between commonly used terms when discussing stress in thin films, residual stress, σ_r, will be used as a more inclusive term. It will include the contributions of both thermal stress, $\sigma(T)$, and intrinsic stress, σ_i. Thermal stress in thin films will develop because of differential thermal expansion of a substrate/film system. Differential thermal expansion of the film and the substrate is due to a mismatch in coefficients of thermal expansion (CTE). When a film/substrate composite experiences a change in temperature, the two different materials are going to expand or contract by different amounts. However, continuity of strain must be preserved, which means that both materials will be constrained, resulting in thermal stress. Intrinsic stress is defined as the internal stress created as a result of the growth

51

processes during film deposition. Therefore, the residual stress can be defined as the sum of the two types of internal stresses:

$$\sigma_r = \sigma(T) + \sigma_i \tag{15}.$$

Residual stress in films can be either compressive or tensile. If the stress is large enough, it could lead to fracture of the substrate, film or substrate/film interface. According to the theorem of minimum energy, the equilibrium state of an elastic solid body is when the potential energy of the system is at a minimum. For a system that is experiencing externally applied forces or residual stress, the system may find an equilibrium position if rupture has occurred reducing the potential energy of the system [53]. Summarizing the theorem of minimum energy, the strain energy caused by residual stress may be reduced by the rupture or delamination of the film. In extreme cases tensile residual stress may lead to film cracking and peeling away from the substrate [54] and compressive residual stress may lead to film buckling and delamination from the substrate (Figure 25).

a)   b)
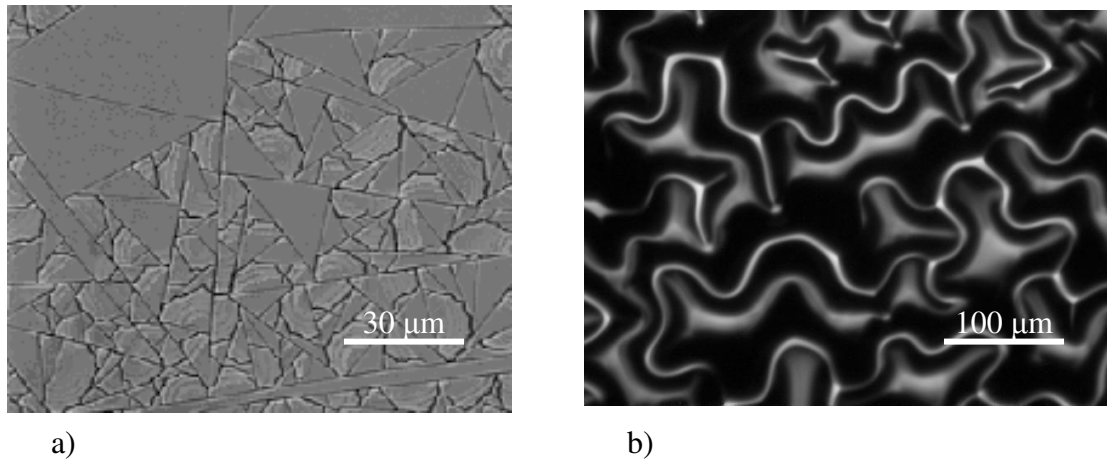
Figure 25. a) Low-k dielectric film in tension [54] and b) tungsten film in compression.

52

Besides the extreme cases just mentioned, residual stresses may also lead to the generation of crystalline defects, imperfection of epitaxial layers and the formation of film surface features such as hillocks and whiskers [11]. These less obvious results of residual stress may affect material properties such as magnetization, reflectivity and electrical conductivity [36, 51].

3.2 Measuring Residual Stress

Completely avoiding residual stresses in thin films is impossible to do. For many applications small amounts of residual stress may be tolerable and may not have any significant effects on the operation and reliability of the device. For ensuring device operation and for optimizing deposition parameters, it is necessary to measure the amount of residual stress in thin films. Techniques for measuring residual stress will be different from the techniques used for measuring the stress as the result of externally applied forces. For externally applied loads there will be a direct cause and effect that is in general, easily measured. For example, if an external force is uniaxially applied to an arbitrary body, the result will be a deformation of the body that is proportional to the applied force. The amount of deformation can be related to the initial dimensions of the body, and is defined as the strain, ε:

$$\varepsilon = \frac{l'-l_0}{l_0} = \frac{\delta}{l_0} \tag{16},$$

where l' and l_0 are the deformed and initial body lengths, respectively, and δ is the absolute deformation.

If the strain is kept within elastic limits, the body will return to its initial shape upon unloading and the material is said to be perfectly elastic. In most cases the strain

can be directly measured during loading and unloading by the use of extensometers or strain gages. By the use of Hooke's law, which defines stress as being proportional to strain, the stress can then be calculated. For residual stress in thin films, a simple measurement of the strain produced during deposition is not as straight forward. Residual stress produced during sputter deposition is an example where strain gages and extensometers cannot be used to get a direct measurement of strain.

One tell-tale sign of having large amounts of residual stress in a film is by observing the effects it has on its substrate. In extreme cases the film will spontaneously delaminate from the substrate, where in other cases there may be apparent bending of the film/substrate. In the mid 1800s to early 1900s, many scientists observed these unwanted results when electrolytically depositing metallic films [55, 56]. Since those early observations, calculating residual stress in films by measuring the change in curvature of the substrate before and after film deposition has been a popular method. The use of X-ray diffractometry has also become an accepted technique for determining residual stress in crystalline films where a direct determination of elastic strain is possible.

3.2.1 Curvature Method

The majority of formulas used in the determination of thin film residual stress by curvature techniques are variations of an equation first given by G. Stoney in 1909 [56]. The derivation of the formula is relatively straight forward and is based on a mechanics of materials approach. Hypothetically starting with a film under compressive residual stress, an exaggerated film/substrate pair would appear as shown in Figure 26. The compressive stress is the result of the film wanting to expand, but it is being constrained

54

by the substrate. Therefore, the system would be concave downward with a negative curvature.
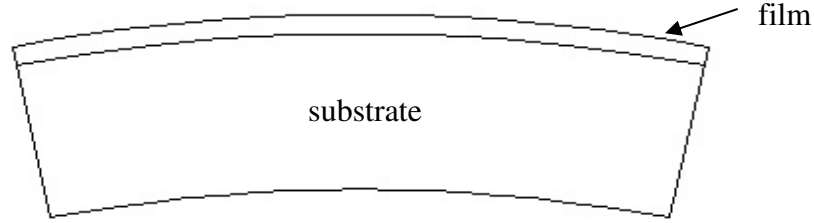
Figure 26. Schematic of film/substrate bending due to compressive residual stress in the film.

A solution for solving the stress in the thin film can be started by first maintaining mechanical equilibrium, which requires that the net force *F*, vanish on any film/substrate cross section:

$$F = \int_A \sigma \cdot dA \qquad (17),$$

where σ is the stress and *A* is the cross sectional area. A free body diagram of the system is represented in Figure 27, where statically equivalent combinations of forces and moments have replaced the interfacial set of forces. The force and moment of the film are represented by the symbols F_f and M_f, respectively, and F_s and M_s are for the substrate. The force F_f must be equal to the force F_s and can be imagined to act uniformly over the cross sectional area, *t·w* (*w* is the film width), giving rise to the film stress, σ_f. The moments are responsible for the bowing of the film/substrate system their sum must also be equal to zero, yielding the expression:

$$F_f\left(\frac{t}{2}\right) + F_s\left(\frac{d}{2}\right) = F_f\left(\frac{t+d}{2}\right) = M_f + M_s \qquad (18),$$

where *t* and *d* are the film and substrate thicknesses, respectively.

www.manaraa.com
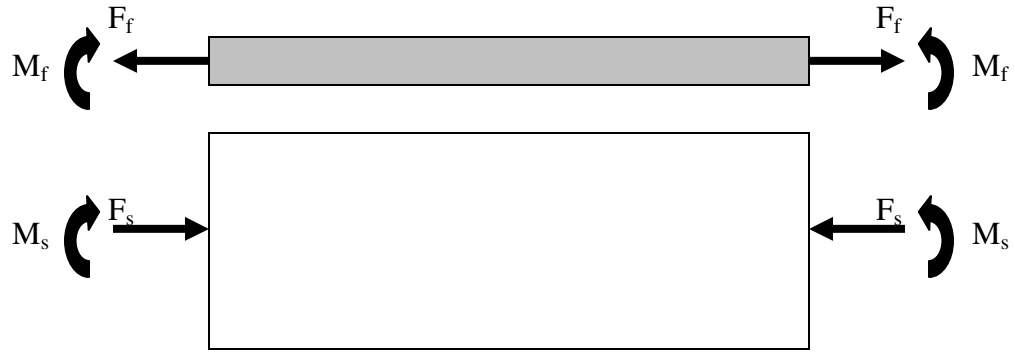
Figure 27. Free body diagrams of the film and substrate with indicated forces and moments.

Since the film/substrate pair is not restrained from moving, it will bend to counteract the unbalanced moments and it can treated as a beam with the curvature, k, where the curvature is defined as the following presented in Figure 28:

$$k = \frac{1}{R} = \frac{d\theta}{ds} = C\frac{d^2 y}{dx^2} \tag{19}.$$

$$C = \frac{1}{\left[1 + (dy/dx)^2\right]^{3/2}} \tag{20}.$$

For conditions of small defections (dy/dx << 1) it is assumed that $C = 1$ and the curvature can be approximated as:

$$k = \frac{d^2 y}{dx^2} \tag{21}.$$

56
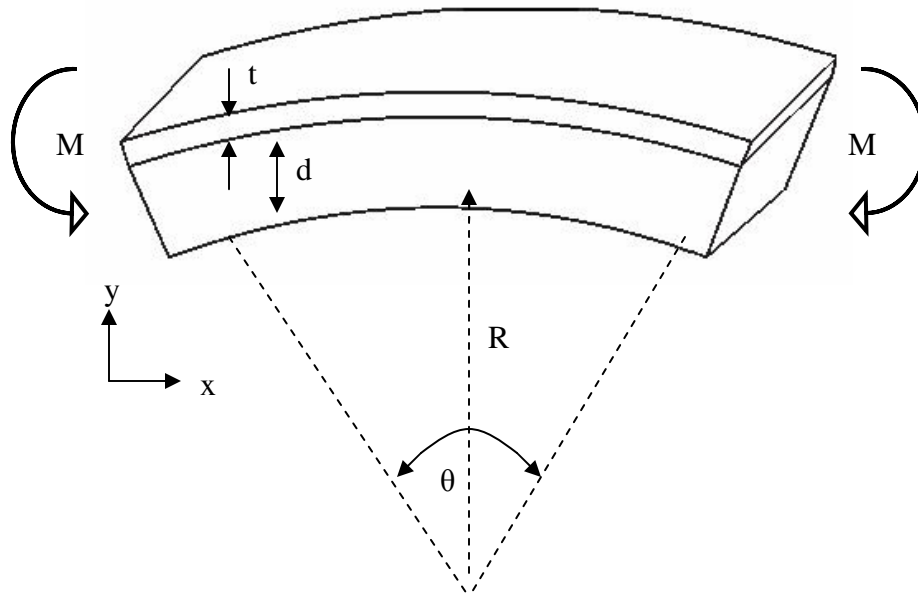
Figure 28. Elastic bending of a beam under an applied moment.

As the deflection increases the value of *C* will change and can no longer be assumed to be 1. Table 4 shows the change in *C* with an increase in the slope of a beam. An increase in the slope of the beam, dy/dx, corresponds to an increasing deflection. In one of the more extreme cases of wafer bowing seen later, dy/dx was measured to be 0.000583. Therefore, it was safe to assume *C* = 1 for all cases here.

Table 4. Small-deflection assumptions *C* = 1.

dy/dx	0.01	0.05	0.10	0.25	0.50	1.00	2.00
Θ (deg)	0.6	2.9	5.7	14.0	26.6	45.0	63.4
C	0.9999	0.9963	0.9852	0.9131	0.7155	0.3536	0.0894

The longitudinal strain will vary linearly with the distance from the neutral axis and is proportional to the curvature of the beam. By applying Hooke's law for the normal bending stress:

57

$$\sigma_m = E \cdot k \cdot y \qquad (22),$$

where E is the elastic modulus of the substrate material and y is the distance from the neutral axis. The bending moment corresponding to this stress distribution across the beam section will be:

$$M = \int_{-d/2}^{d/2} \sigma_m \cdot y \cdot dA = \int_{-d/2}^{d/2} E \cdot k \cdot y^2 \cdot dA = \frac{E \cdot k \cdot w \cdot d^3}{12} \qquad (23).$$

Extending this result for both the film and substrate:

$$M_f = \frac{E_f \cdot k \cdot w \cdot t^3}{12}, M_s = \frac{E_s \cdot k \cdot w \cdot d^3}{12} \qquad (24).$$

Substitution of this last expression back into equation (18) and assuming biaxial stress rather than uniaxial stress, where E is replaced with $E/(1-v)$ gives:

$$F_f \left(\frac{t+d}{2} \right) = \frac{E_f \cdot k \cdot w \cdot t^3}{12 \cdot (1-v_f)} + \frac{E_s \cdot k \cdot w \cdot d_s^3}{12 \cdot (1-v_s)} \qquad (25),$$

where v_f and v_s are the film and substrate Poisson's ratios, respectively. Since d is usually much larger than t, the film stress is solved to be:

$$\sigma_f = \frac{F_f}{t \cdot w} = \frac{E_s \cdot d^2 \cdot k}{6 \cdot (1-v_s) \cdot t} \qquad (26).$$

Equation (26) is the Stoney formula, where σ_f is calculated from the measured change in curvature before and after film deposition, knowing the film and substrate thicknesses and the substrate mechanical properties. Some care must be taken when using the Stoney equation for determining residual stress in the deposited film because the derivation of the formula used the following assumptions: 1) Both the film and substrate are homogeneous, isotropic and linearly elastic materials, 2) small deformation is present in the substrate (dy/dx << 1), 3) uniform curvature with the system's curvature

58

components being equi-biaxial, 4) uniform film and substrate thickness with $t_f << t_s$, 5) the film stress states are equi-biaxial while the out of plane stress and shear stresses are zero and 6) perfect adhesion between the film and the substrate.

3.2.2 Stress Calculation Assuming Uniform Curvature and Film Thickness

There are many tools that work well for calculating residual stress in thin films based on the curvature method previously discussed. For many of the tools available, the assumptions used when deriving the Stoney formula are also made for the stress calculation. For example, the user will be asked to input the substrate and film thicknesses and the substrate mechanical properties E and ν. From there it is assumed that materials are isotropic and homogeneous and that the thicknesses are uniform. The only measurement that is taken by the equipment will be the curvature before and after film deposition. The method used for measuring the curvature will vary from manufacturer to manufacturer and include optical, mechanical, magnetic and electrical methods.

A Flexus 2-300 is one of the tools used here, which utilizes an optical method for measuring the curvature in order to calculate the thin film residual stress. It uses a single laser and a series of mirrors and optics to split the beam into two parts and direct them down at the sample surface. If the sample surface is optically smooth, the two beams will be reflected off the sample surface and detected by two light sensors that record the beams' position. As the curvature of the sample changes, the position of the reflected light beam on the light sensor will also change. By knowing the geometry of the system, presented in Figure 29, the curvature can be calculated for the sample. The curvature is straightforward to calculate by knowing two distances: 1) the distance between the wafer

59

and light detectors and 2) the distance between the two points where the laser beam hits the wafer. From there, the angles α and β in Figure 29 can be determined, which can be related to the slope of the wafer at the two points.

$$\alpha = \frac{\pi}{2} - \tan^{-1}(slope\_A) \qquad (27),$$

$$\beta = \frac{\pi}{2} - \tan^{-1}(slope\_B) \qquad (28).$$

With those two angles known, the angle Φ can be found, which is used with the distance between the two laser beams, D, to calculate the radius of curvature:

$$\Phi = \pi - \alpha - \beta \qquad (29),$$

$$R = \frac{\Phi}{D} \qquad (30).$$

This geometric proof is only valid for small angles Φ, where the straight line D can be assumed to be equal to the arc length.
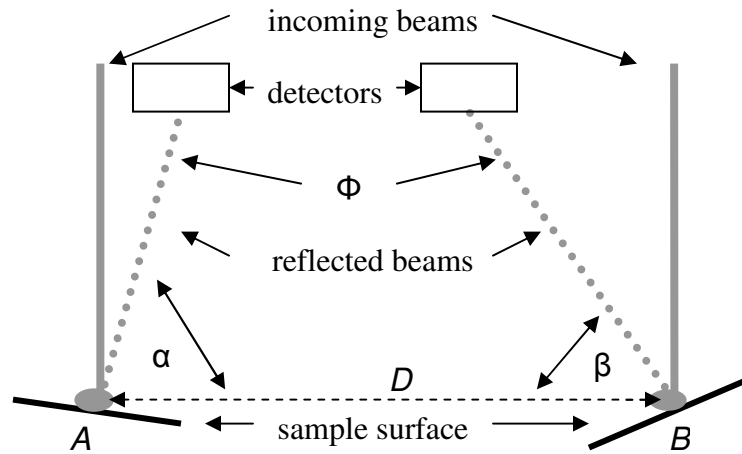
Figure 29. Geometry of the Flexus 2-300 curvature calculation.

The sample holder for the Flexus 2-300 requires 4" or 6" wafers and it can be rotated in 45º increments. It also has a heating table built into the sample holder so that thermal stress can be calculated. Since the radius of curvature is found by using two

60

points from the wafer and geometric relations of the system, the Flexus cannot account for changes in the curvature across the wafer. Therefore, a uniform film thickness and curvature is assumed at each 45º increment of rotation. At best, an average stress can be reported by averaging the stress calculated from the four different possible directions of rotation. In the case of axisymmetric curvature and stress, the curvature and stress only depend on the radial position. Therefore, no changes in curvature and stress will be noticed in the circumferential direction, which corresponds to the rotation of the wafer on the Flexus stage. So it would be possible to have the residual stress be reported equal for all four stage rotations, even though the residual stress is non-uniform in the radial direction.
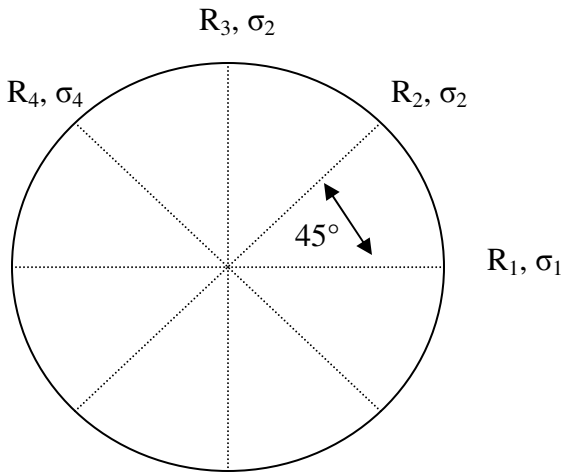
Figure 30. Flexus 2-300 stage rotation.

In general, the Flexus system is reliable and simple to use, but is limited if there are significant non-uniformities of film thickness, radius of curvature and residual stress. The user is confined to assuming uniformity which may be very costly in the end when considering the future application of the film/substrate combination. Given these limitations a different method for measuring the radius of curvature was needed.

61

3.2.3 Accounting for Non-uniformities

Unfortunately, there are many thin film deposition methods currently used that make it difficult to agree with all the assumptions used in the Stoney equation. For example, depending on the system parameters of magnetron sputter deposited films, film thickness, quality and deposition rates may be difficult to keep uniform across the area of a substrate. Magnetron sputtering systems have found wide application in commercial coating processes, particularly for the deposition of thin metallic films. Their acceptance is due to the possible combinations of high current densities at moderate voltages and reduced gas scattering of the sputtered atoms at low operating pressures, which results in higher depositions rates than non-magnetron systems. However, magnetron systems do have some disadvantages when it comes to film thickness uniformity. It has been widely studied that film thickness uniformity can be affected by non-uniform magnetic fields, gas pressure, target to substrate distance and shealth thickness in magnetron systems [28-33].

In order to maintain the desired film properties, non-uniformities in film thickness and stress must be first quantified and then controlled through the deposition process. With such non-uniformities being present, the traditional approach of using Stoney's formula may not be adequate. In order to compensate for non-uniformities in film thickness and curvature, a localized approach using the Stoney formula has been attempted. Instead of ignoring the assumptions made in the derivation of the Stoney equation, the Stoney equation was applied to smaller areas of the wafer where variations in curvature and film thickness were minimal. Therefore, the Stoney equation assumptions would be satisfied in the localized areas.

62

To carry out this localized approach, samples were profiled before and after film deposition using a Tencor P-20h profilometer. Initial tests were performed on 4" (100) silicon wafers that were later coated with tungsten films using a DC magnetron sputtering system. The goal of the initial tests was to determine whether or not there was uniformity in the radius of curvature across a wafer. Uniformity was not expected because it had already been observed that film thickness varied radial when using the CRC-100 sputtering system (Figure 15).

The total scan length of the initial wafer profiles was 6 cm taken at 15° increments. This was done to map the changes in curvature over a large portion of the wafer surface. The scan speed was 2 mm/sec with a sampling rate of 50 Hz. The scan speed and the sampling rate were chosen to ensure clean data and to keep the total number of data points within a reasonable size ($\approx$ 1000 pts.). Since the profilometer stage was flat, the wafers were setup on a tripod configuration using 3 steel balls mounted to the profilometer stage. This configuration ensured that the wafers would not rock on the stage because of their curvature. Modifications had to be made to the profilometer stage in order to achieve a repeatable placement of the wafers before and after film deposition. To do this, metal stops were mounted to the profilometer stage so that the wafer placement would be confined in two directions. Two stops were placed close together in order to mate up with the flat side of the wafer and maintain rotational confinement and a third stop was used to maintain directional confinement. The setup and stage layout for scanning 4" wafers can be seen in Figure 31.

63
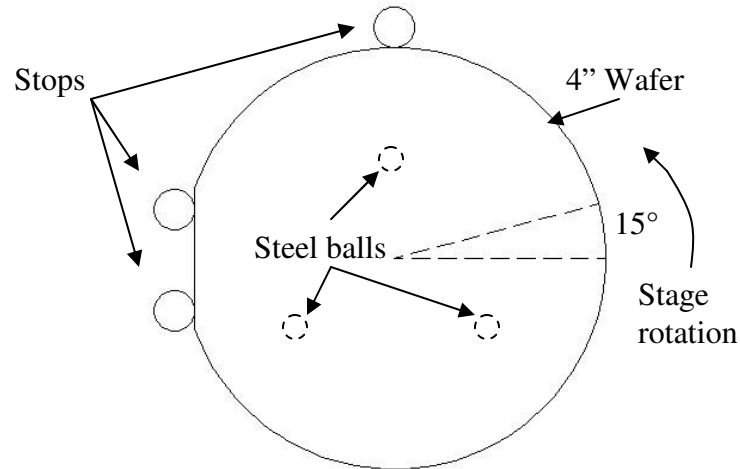
Figure 31. Profilometer stage layout for 4" wafers.

A profile taken from a wafer before and after film deposition is shown in Figure 32. The scan was started 3 cm to the left of the wafer center, with the scan direction moving to the right, crossing through the center of the wafer and having a total scan length of 6 cm. Deflection of the wafer in the y-direction after film deposition appears more extreme than what the true deflection is because of the placement of the coordinate origin in Figure 32. This is the result of the profilometer software automatically assigning the x and y-coordinates, $(0, 0)$, at the starting point of the scan. The way in which the coordinates are defined by the profilometer is of no consequence in the determination of the film's residual stress since a change in curvature is required when using the Stoney equation. For this example a tungsten film was sputter deposited at a low argon pressure (4 millitorr), introducing a significant amount of compressive residual stress. The final wafer shape is bowed concave downwards because of the compressive residual stress, resulting in a negative curvature. The x-axis was also adjusted in Figure 32 to place the center of the wafer at an x-position equal to zero.

64
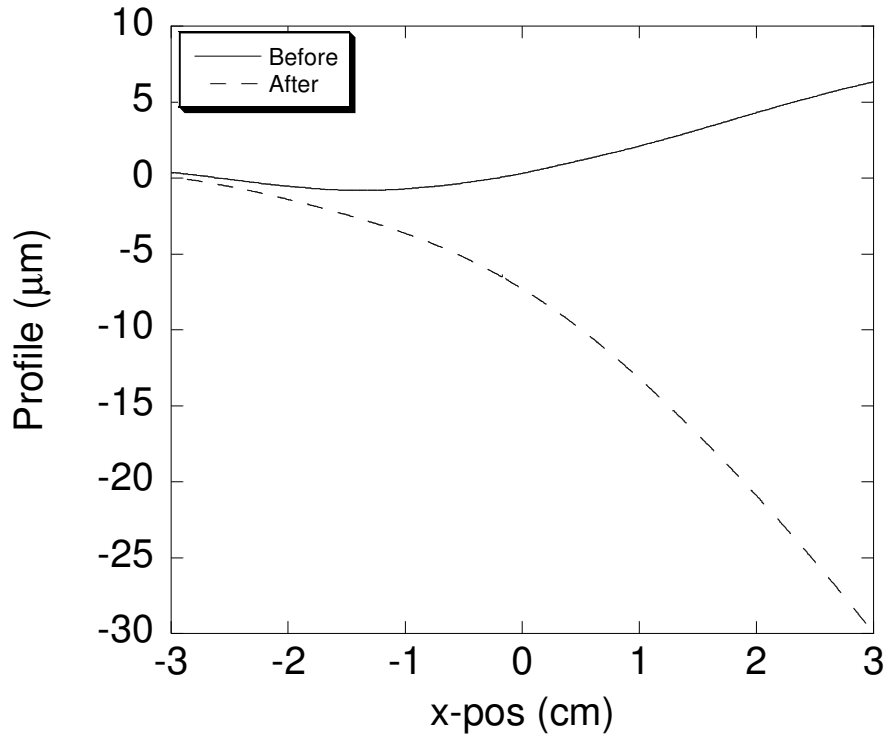
Figure 32. Profiles of a wafer before and after film deposition.

With a relatively small maximum displacement, the second derivative of the profile can be considered equal to the curvature without introducing a significant amount of error (Table 4). To continue with the localized approach, the profiles in Figure 32 where broken into 20 segments of 3 mm lengths. Each 3 mm length was curve fitted with a second order polynomial (Figure 33). A second order polynomial was sufficient for the 3 mm profile lengths and a correlation coefficient > 0.9999 was consistent for all segments. The second derivative of the curve fit was taken to be equal to the curvature of the segment. The difference in curvature before and after film deposition was used in the calculation of the residual stress in the film segment using equation (24).

65
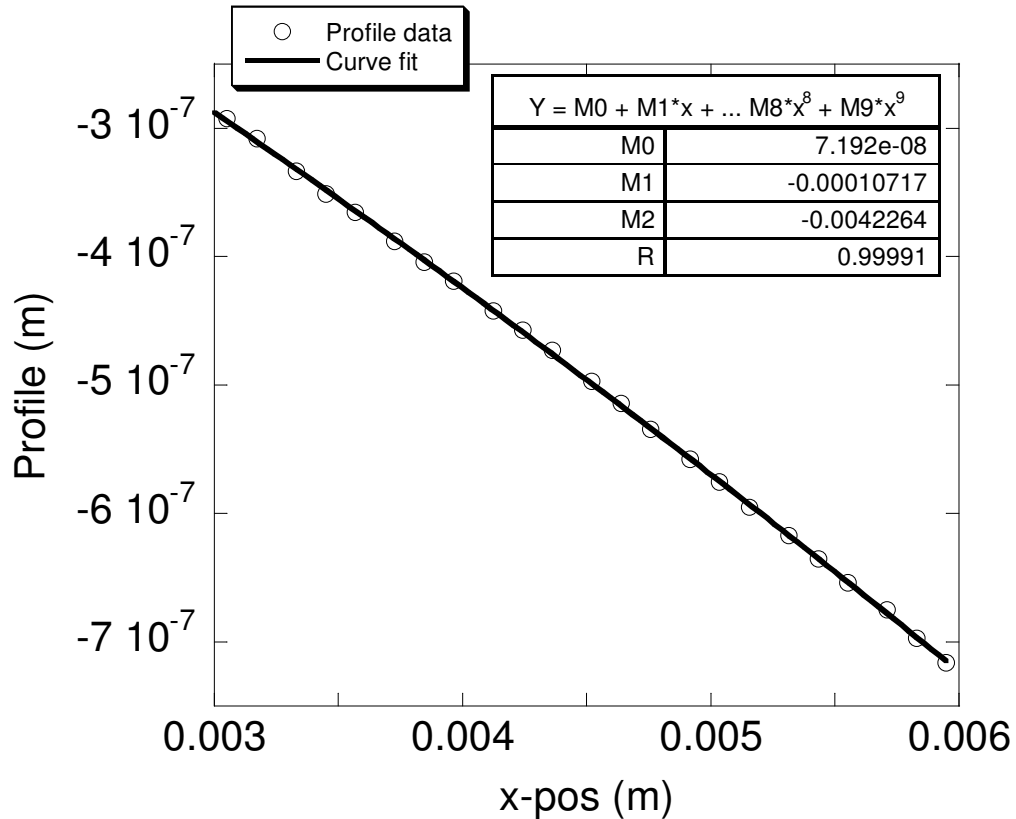
Figure 33. Finding the curvature of 3 mm segments.

The change in curvature from before and after film deposition across the wafers
was more significant than originally hypothesized. A plot in the change of curvature for
a tungsten film deposited at 4 millitorr Ar pressure is shown in Figure 34. The error bars
in Figure 34 represent the deviation in curvature measured as the wafer was rotated at 15°
increments. The deviation from the average value is less than 10 % and can be primarily
attributed to the center of wafer not being aligned with the center of the sputtering target
during film deposition. A small deviation could also be expected from the center of
rotation during profiling being slightly off from the center of the wafer. With that in
mind, it can be established that the curvature is axisymmetric and is a function of the
radial position. Any deviation observed in the circumferential direction is thought to be

66

the result of the off-centered wafer placement during film deposition and profile measurement.
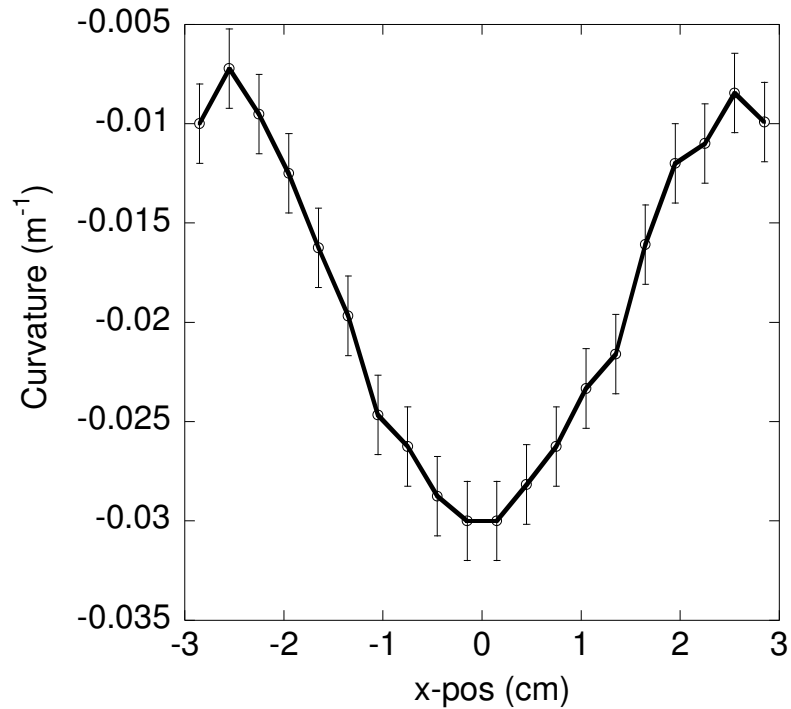
Figure 34. Change in wafer curvature after film deposition at 4 millitorr Ar pressure.

A maximum absolute value of the curvature change occurs at the wafer center in Figure 34 and then decreases with an increasing radial position. Figure 35 is a plot in the change of curvature for a tungsten film deposited at an Ar pressure of 10 millitorr. As observed in Figure 34, there is a maximum absolute value of the curvature change at the center of the wafer. An interesting transition occurs in Figure 35 where there is a point of inflection and the curvature changes from a positive to negative as the radial position is increased. This transition indicates that there is a change from tensile to compressive residual stress. The transition in curvature adds to the dynamic nature possible by magnetron sputtering systems that was confirmed in Chapter 2 of the manuscript.

67
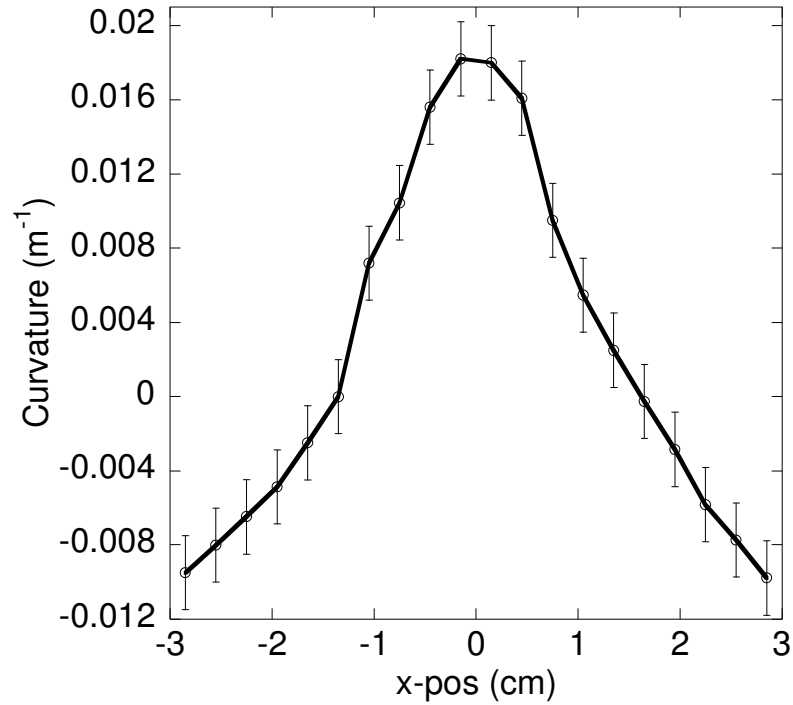
Figure 35. Change in wafer curvature after film deposition at 10 millitorr Ar pressure.

Before the residual stress could be calculated, the change in film thickness had to be accounted for. The film thickness profile was found earlier to be axisymmetric and only dependent on the radial position. In order to assign a film thickness to each of the individual profile segments, a fourth order polynomial was fitted to the film thickness profile data obtained from the sputtering experiments (Figure 36). This allowed for the film thickness to be calculated at any radial position, assuming that the shape of the profile does not change from experiment to experiment. The center point of each localized segment was used for calculating its film thickness, and was assumed uniform for the entire segment. The film thickness difference across a 3 mm segment was found to vary by less than 1 % at the center portion of the wafer, up to approximately 4 %, 4 cm out from the wafer center (Figure 36).

68

$Y = M0 + M1*x + ... M8*x^8 + M9*x^9$	
M0	7.9638e-07
M1	5.9621e-09
M2	-2.09e-06
M3	-5.9581e-08
M4	2.9184e-06
R	0.99059
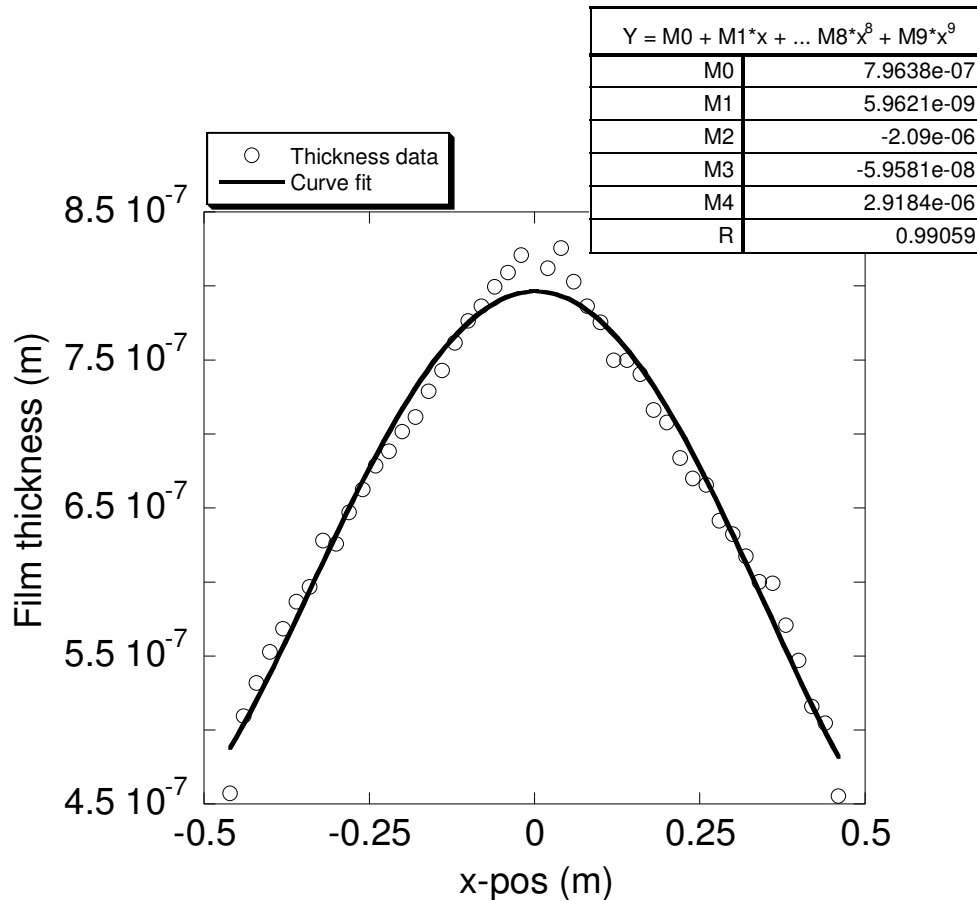
Figure 36. Fourth order polynomial used to fit the thickness profile.

To account for differences in film thickness between sputtering runs, a small piece of a glass slide was placed on the outer edge of the 4" wafers before film deposition. After film deposition the glass piece was removed and a profilometer was used to measure the step height in film thickness at the outer edge of the wafer. Differences measured in the outer edge film thicknesses compared to the fitted thickness profile could be adjusted for by changing the M0 term in the fourth order polynomial shown in Figure 36. M0 is the constant in the polynomial equation and allows for the curve adjustment in the y-direction. By accounting for film thickness differences this way, the profile shape is assumed to be constant, which is a source of small error in calculating film thickness.

69

By using the approach outlined above, each segment will have a unique curvature and film thickness, which is only dependent on its radial position. Equation (26) was applied to each segment to calculate the residual stress in the film. Results of using the localized approach are shown in Figure 37 and Figure 38. As observed in the curvature figures, error bars are used to show the variation in residual stress measured at the different 15° rotation increments. Figure 37 is a plot of the residual stress calculated in a tungsten film that was deposited at 4 millitorr Ar pressure. A maximum residual stress of approximately -1500 MPa is located at the center of the wafer, which coincides with the maximum change in curvature plotted in Figure 34. As the radial position is increased, there is a sharp decrease in residual stress which hits a minimum of approximately -600 MPa at a radial position of 3 cm.

Figure 38 is a plot of the residual stress calculated in a tungsten film that was deposited at 10 millitorr Ar pressure. A maximum tensile residual stress of approximately 1000 MPa is located at the center of the wafer, which coincides with the maximum positive change in curvature plotted in Figure 35. As the radial position is increased, there is a sharp transition in residual stress towards compressive stress. A maximum compressive residual stress was calculated to be approximately -800 MPa at a radial position of 3 cm.
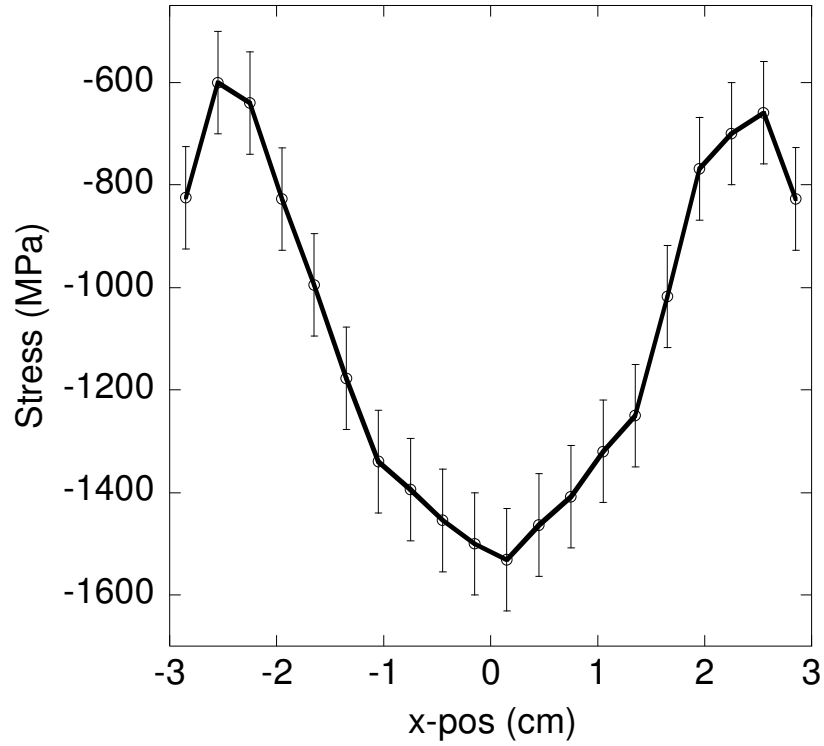
Figure 37. Residual stress in a tungsten film deposited at 4 millitorr Ar pressure.
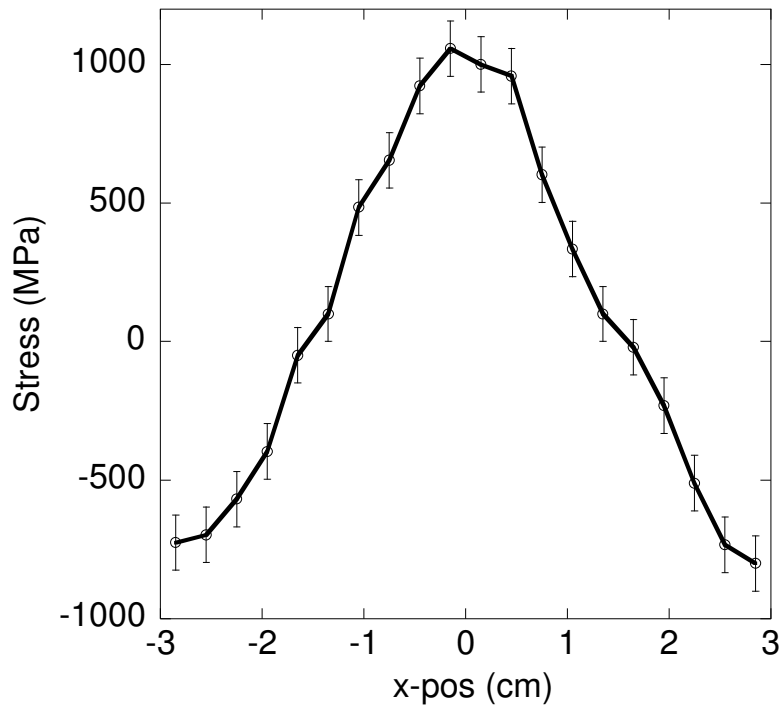
Figure 38. Residual stress in tungsten film deposited at 10 millitorr Ar pressure.

71

After examining the results plotted in Figure 34 thru Figure 38, there are two significant effects to be noticed. First, it was observed that the film thickness, change in curvature and residual stress were all axisymmetric about the wafer center. There was some deviation in the rotational direction, but that would be expected with a slightly off-centered film deposition and wafer prolife. Therefore, the deviation is thought to be caused by experimental setup and could be reduced with future modifications to wafer placement. Second, there was a significant change in stress as a function of the radial position, which in one case changed from tensile to compressive.

Because of these observations, it was decided to make changes to the profiling method. To further examine the change in curvature and residual stress at larger radial positions, the total scan length was increased to 8 cm. Along with an increased scan length, the scan speed was increased to 5 mm/sec to keep the total number of data points at 1000. Due to the axisymmetric results observed, the rotation increment was increased to 45°. The individual segment size was also increased from 3 to 4 mm, while the total number of segments for each scan was kept at 20. These changes allowed for a larger profile of the wafer to be taken without collecting as many data points as in the initial tests.

Along with a change in the profile method, a change in Ar pressure was made for the next test. Previous trials resulted in tungsten films that were predominately either in compressive or tensile residual stress. Therefore, an Ar pressure of 6 millitorr was chosen to try and deposit a film with little or no residual stress present. As before, the sputtering current was kept at 100 mA, the voltage was 0.5 kV and the deposition time was 60 minutes. Figure 39 displays the change in curvature results for a tungsten film

deposited at 6 millitorr. Similar to the 10 millitorr film, there is a combination of both positive and negative curvatures. A negative curvature was measured within approximately 1 cm of the center of the wafer and then at larger radial positions there is a transition to a positive curvature. At approximately 2 cm out, the curvature hits a maximum and then starts to decrease in magnitude with an increasing radial position. As expected, the residual stress follows the same pattern as the change in curvature across the wafer (Figure 40). There is a maximum compressive stress of approximately -450 MPa at the wafer center decreasing to zero stress approximately 1 cm out from the center. A maximum tensile stress of about 900 MPa was calculated between 2 and 3 cm out form the center.
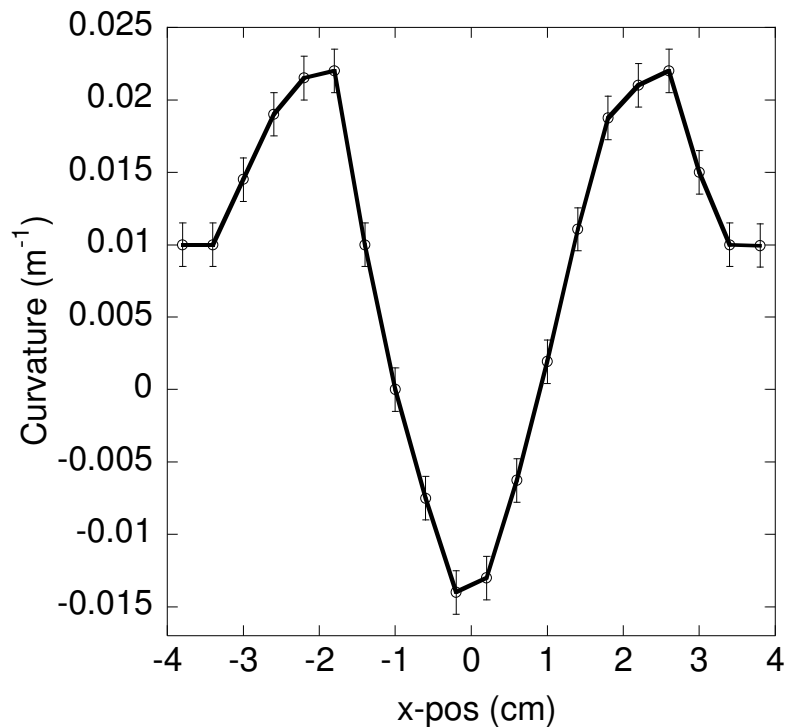
Figure 39. Change in wafer curvature after film deposition at 6 millitorr Ar pressure.

73
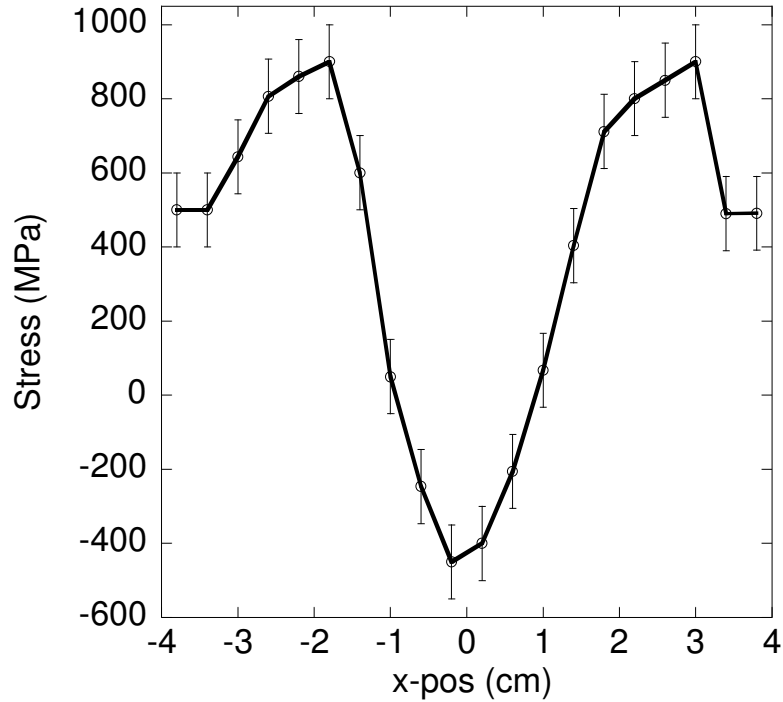
Figure 40. Residual stress in tungsten film deposited at 6 millitorr Ar pressure.

Addition proof of the residual stress axisymmetric state seen in Figure 34-Figure 40, can be observed in Figure 41, where spontaneous delamination of a tungsten film happened immediately after sputter deposition. The tungsten film in Figure 41 was deposited at 2 millitorr Ar pressure, with a sputtering current of 100 mA, a voltage of 0.5 kV and a deposition time of 60 minutes. It was deposited onto a 4" (100) silicon wafer and it was estimated to have maximum compressive stress around 2 GPa. Delamination was noticed within seconds of the power being turned off and it occurred while the system was being vented. Complete delamination of the film was confined to about a 1.25" diameter area, where delaminations of various morphology can be observed heading in all directions. Continuing from approximately 1.25" from the wafer center to about 2"out, telephone cord delaminations take over and extend outward in the radial direction.

74
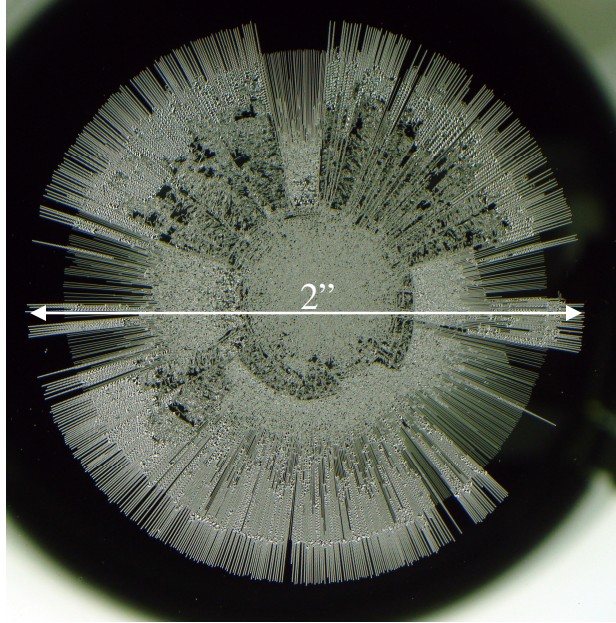
Figure 41. Delamination of a tungsten film deposited at 2 millitorr Ar pressure.

To test the effect of segment size selection on the curvature and residual stress results, a comparison was performed on the tungsten film deposited at 4 millitorr in one of the scan directions. One trial was with the segment size increased to 10 mm, which resulted in the profile being broken down into 6 segments. The stress calculation method remained the same as in the 20 segments procedure, where a film thickness was calculated at the center of segment and assumed to be uniform. A second trial was performed where the curvature was continuously defined across the wafer by fitting a fourth order polynomial to the profile data. This allowed the curvature to be defined at any radial position because the second derivative did not reduce the curvature fit down to a constant. By using the continuous curvature profile in conjunction with the thickness variation, the stress was calculated continuously across the wafer by using equation (26). The results are presented in Figure 42.
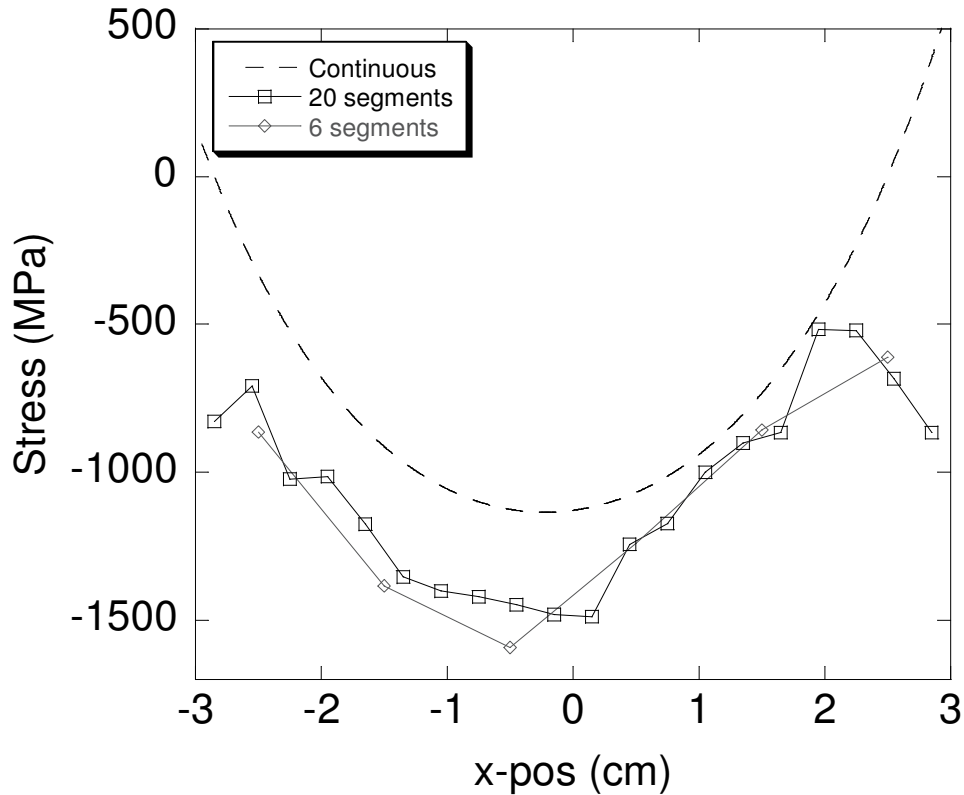
Figure 42. Effects of using different segment sizes on the stress results.

There was not a significant difference observed in the stress results when using 3 and 10 mm segment sizes. For both segment sizes a maximum compressive stress of approximately 1500 MPa was calculated in the center of the wafer and a minimum compressive stress of approximately 800 MPa was calculated at the outer segments. The biggest difference in stress results was observed when the continuous calculation method was used. It resulted in a maximum compressive stress of about 1000 MPa at the center, which is 30 % less than what was calculated with the 3 and 10 mm segment sizes. Even larger differences in the calculated residual stress were observed at the outer edges of the scan. For the continuous calculation there was a transition from compressive stress to tensile stress, which was not observed using the 3 and 10 mm segment sizes. The reason for the discrepancies at the center and the outer edges is due to the fourth order

76

polynomial deviating from the experimental data at those locations. This was not noticed

at first because the fourth order polynomial selected had a correlation coefficient of

0.99969. It wasn't until a closer look was taken at the sections in question and a

deviation in the curve fit and experimental data was noticed (Figure 43).

$Y = M0 + M1*x + ... M8*x^8 + M9*x^9$	
M0	7.6233e-06
M1	2.3317e-05
M2	-0.010591
M3	-0.027774
M4	2.5381
R	0.99969
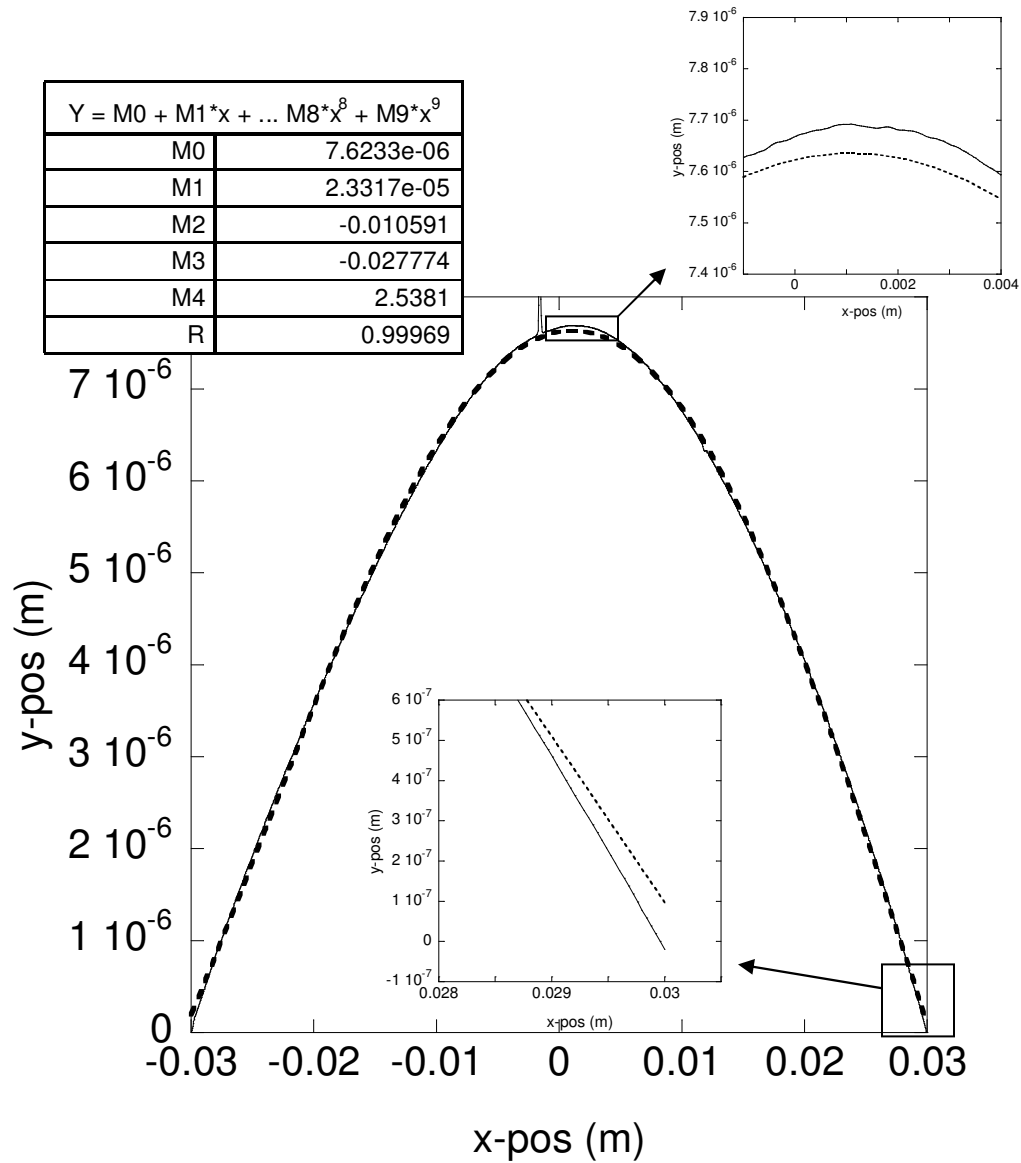
Figure 43. Deviations of fourth order polynomial curve fit from experimental data.

Even though there is only a 10 % difference in the y-position noticed in Figure 43,

it is the second derivative that is used in calculating stress. Therefore, the difference in

77

stress is caused by taking the second derivative of a curve fit that is inaccurate at certain locations. It is concluded that separating the profile scans into small segments is the best way to quantify changes in residual stress. Keeping the segment size small allows for accurate determination of the curvature and film thickness at the individual segments' locations.

To substantiate the stress results calculated using the Stoney equation on multiple segments, X-ray diffraction was also performed to calculate the residual film stress. Similar to the previous methods, the stress can not be directly measured. With X-ray diffraction the change in lattice plane spacing is measured and is related to the film stress.

3.2.4 X-ray Diffraction

By understanding the diffraction geometries between an X-ray beam and a material, X-ray radiation can be used to measure the spacing between lattice planes in crystalline materials. When external loads are applied or residual stress is present in these materials, they will deform in response to the loads or residual stress. This strain will result in a change of the lattice planes spacing and have an effect on the diffraction geometry. With the assistance of X-ray diffraction, the change in interplanar spacing acts as an internal strain gage. By scanning the X-ray detector over a range of 2θ angles (Figure 44), the interplanar spacing d can be found with the use of Bragg's law:

$$(\lambda = 2 \cdot d \cdot \sin \theta)\qquad\qquad(31)$$

where λ is the X-ray wavelength.

78
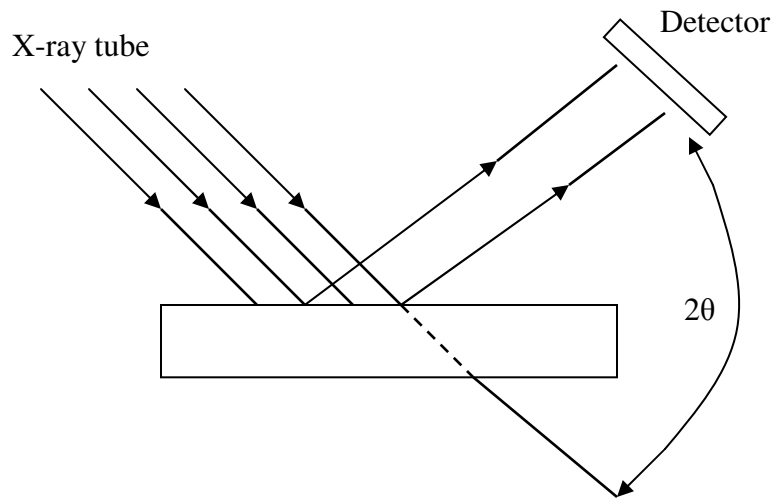
Figure 44. Schematic of the diffractometer setup.

The use of X-ray diffraction for residual stress measurements can be made with the conventional powder X-ray diffractometer. It is generally intended for polycrystalline materials with random grain orientation and well defined elastic constants. Ordinarily a high Bragg angle plane is chosen and strain measurements are made at several arbitrary Ψ angles (Figure 45) ranging from 0 to 90º. This method of measuring the interplanar spacing at various Ψ angles is referred to as the $\sin^2\Psi$ technique and has been used by many researchers for calculating the residual stress in thin films [57-61]. By using the theory of elasticity, along with the lattice planes spacing measurements, the stress (residual or applied) acting on the lattice planes can be determined.

By using the transformation of strain in a three dimensional body, the principal strains in the film can be solved for. To start, a coordinate system for the specimen must be defined and is shown in Figure 45. The specimen coordinate system is defined by the axis S_i, with S_1 and S_2 positioned on the specimen surface and S_3 is normal to the specimen surface. A reference coordinate system related to the X-ray equipment must

79

also be defined and it is referred to as the laboratory system. It is defined by L_i, where L_3 is in the direction normal to the family of planes (hkl) and makes an angle Ψ with S_3. L_1 and L_2 are on the plane defined by S_1 and S_2 and make an angle Φ with S_1 and S_2, respectively. It is important to have a clear definition of the specimen and laboratory coordinate systems because their relationships are needed for the transformation of strain.
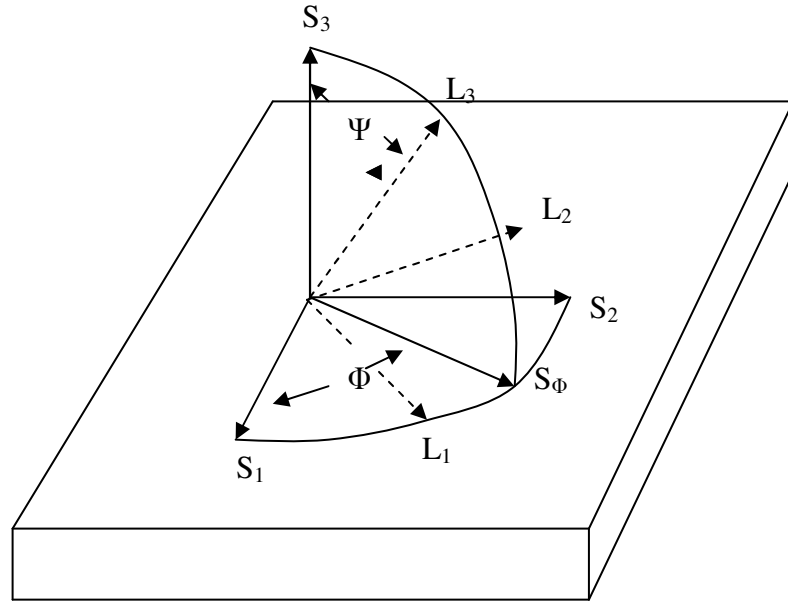
Figure 45. $\mathrm{Sin}^2 \psi$ technique.

Once the lattice spacing, $d_{\Phi\Psi}$, is obtained from the position of the diffraction peak for a given reflection (hkl), the strain along the L_3 direction may be obtained from:

$$(\varepsilon_{33})_{\Phi\Psi} = \frac{d_{\Phi\Psi} - d_0}{d_0} \tag{32},$$

where d_0 is the unstressed lattice spacing. The strain, $(\varepsilon_{33})_{\Phi\Psi}$, may be expressed in terms of the strains in the sample coordinate system by utilizing the transformation rule for second rank tensors:

$$(\varepsilon_{33})_{\Phi\Psi} = a_{3k} a_{3l} \varepsilon_{kl} \tag{33},$$

80

where a_{3k} and a_{3l} are the direction cosines between L_3 and S_k and S_l, respectively. To remain consistent from here on, the suffix notation will be used to describe the Cartesian tensors. To find the direction cosine matrix for this case, the individual rotations need to be determined first. The first individual rotation is by Φ about the S_3 axis, and is given by the matrix *A3*:

$$A3 = \begin{vmatrix} \cos\Phi & \sin\Phi & 0 \\ -\sin\Phi & \cos\Phi & 0 \\ 0 & 0 & 1 \end{vmatrix} \tag{34},$$

and the second individual rotation will be Ψ about the S_2 axis and is given by the matrix *A2*:

$$A2 = \begin{vmatrix} \cos\Psi & 0 & -\sin\Psi \\ 0 & 1 & 0 \\ \sin\Psi & 0 & \cos\Psi \end{vmatrix} \tag{35}.$$

The complete direction cosine matrix for the new coordinate system is the product of the individual rotations given in equations (34) and (35):

$$a_{ik} = A2A3 \tag{36},$$

$$a_{ik} = \begin{vmatrix} \cos\Phi\cos\Psi & \sin\Phi\cos\Psi & -\sin\Psi \\ -\sin\Phi & \cos\Phi & 0 \\ \cos\Phi\sin\Psi & \sin\Phi\sin\Psi & \cos\Psi \end{vmatrix} \tag{37}.$$

Substituting for a_{3k} and a_{3l} in equation (33) and using the double angle formula for sine and cosine ($\sin 2t = \sin t \cos t$) to simplify the expression, $(\varepsilon_{33})_{\Phi\Psi}$ can be solved for:

$$(\varepsilon_{33})_{\Phi\Psi} = \frac{d_{\Phi\Psi} - d_0}{d_0} = \begin{aligned} &\varepsilon_{11}\cos^2\Phi\sin^2\Psi + \varepsilon_{12}\sin 2\Phi\sin^2\Psi \\ &+ \varepsilon_{22}\sin^2\Phi\sin^2\Psi + \varepsilon_{23}\sin\Phi\sin 2\Psi \\ &+ \varepsilon_{13}\cos\Phi\sin 2\Psi + \varepsilon_{33}\cos^2\Psi \end{aligned} \tag{38}.$$

This is the fundamental equation of X-ray strain determination and is a linear equation of six unknowns that may be solved if $d_{\Phi\Psi}$ is solved in six independent directions. When analyzing polycrystalline materials, it is possible to obtain a diffracted beam at all Ψ tilts ($-90° \rightarrow 90°$) and there will be three types of $d_{\Phi\Psi}$ versus $\sin^2\Psi$ behavior (Figure 46).
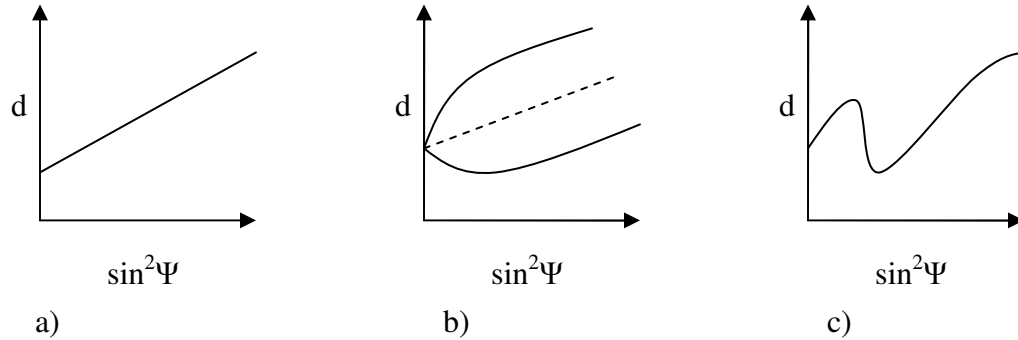
Figure 46. Types of d versus $\sin^2\Psi$ plots observed in residual stress analysis from polycrystalline materials: a) equi-biaxial stress, b) shear strains are non-zero and c) anisotropic elastic constants.

Figure 46 a) depicts a linear d versus $\sin^2\Psi$ behavior that can be expected when the shear strains are zero. When the shear strains are non-zero, d measured at positive and negative Ψ will be different, causing a split in the data which is shown in Figure 46 b). If there is a presence of a non-homogeneous stress/strain state or anisotropic elastic constants, there will be an oscillation in the d versus $\sin^2\Psi$ plot similar to that depicted in Figure 46 c).

Once the strains are obtained, the stresses in the S_i coordinate system may be calculated from the general form of Hooke's law:

$$\sigma_{ij} = C_{ijkl}\varepsilon_{kl} \tag{39},$$

where the elastic coefficients, C_{ijkl}, are referred to the S_i coordinate system. The stresses in any other coordinate system may be determined from the transformation rule for second rank tensors:

$$\sigma'_{mn} = a_{mi} a_{nj} \sigma_{ij} \tag{40}.$$

The inverse of equation (39) can be used to express the strains in the specimen coordinate system:

$$\varepsilon_{ij} = S_{ijkl} \sigma_{kl} \tag{41},$$

where S_{ijkl} are the elastic compliances. By substituting equation (41) into equation (38) the stresses can be linked to the measured diffraction data. It must be noted that the elastic compliances are also referred to the S_i coordinate system and must be obtained from the elastic constants referred to the unit cell axes. For anisotropic crystals the elastic compliance will be dependent on the crystal axis direction and this will be especially important in textured film [58, 59, 62]. This can be neglected in bulk materials because isotropic behavior is obtained when the individual crystallites are oriented throughout space with equal directional probability.

Residual stress measurements of tungsten films were of interest here, therefore crystalline structure had to first be confirmed. The tungsten film had the normal θ-2θ ($\Psi = 0$) scan performed to confirm that it was polycrystalline (Figure 47). It can be observed in Figure 47 that several 2θ peaks are present, which indicate random crystal orientation. Therefore, the $\sin^2\Psi$ technique can be applied and based on the axisymmetric results found using the curvature technique in the previous section, a $\sin^2\Psi$ plot similar to the one depicted in Figure 46 a) is likely.

83
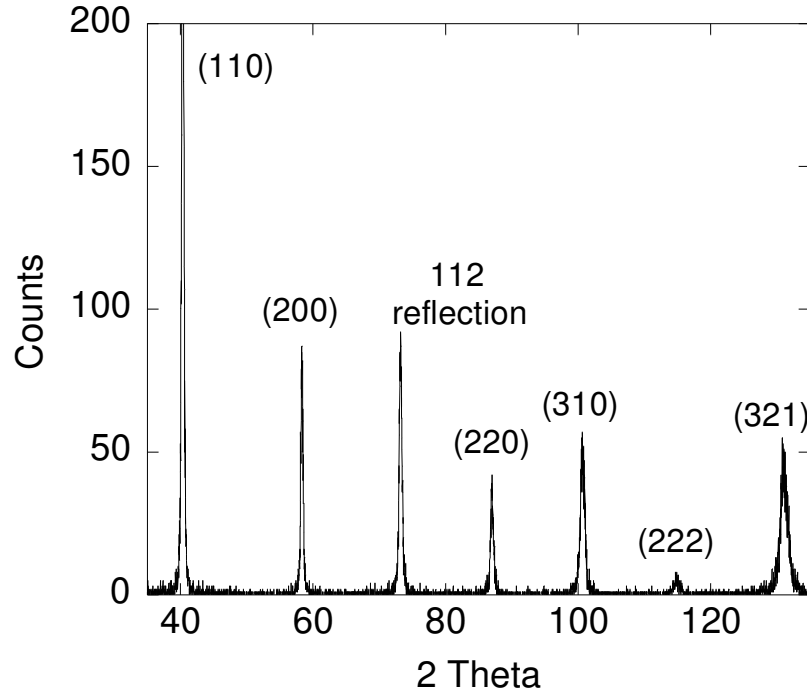
Figure 47. 2 Theta scan of tungsten film.

The 40° peak was chosen first for the $\sin^2\psi$ technique on because it is the highest intensity peak corresponding to (110) planes spacing. Next the elastic constant in the (110) direction had to be solved for. Since tungsten has a BCC crystal structure, there are only three independent compliance values, and they were found to be $S_{11} = 0.26$ x 10^{-11} Pa^{-1}, $S_{12} = -0.07$ x 10^{-11} Pa^{-1}, $S_{44} = 0.66$ x 10^{-11} Pa^{-1} [63]. With the plane direction chosen and the corresponding compliance values of the crystal axes gathered, the compliance value in a new direction can be solved for using the following equation:

$$S'_{ijkl} = a_{im}a_{jn}a_{ko}a_{lp}S_{mnop} \qquad (42),$$

where a_{im}, a_{jn}, a_{ko} and a_{lp} are from the transformation matrix given in equation (40) which defines the orientation of our new coordinate system in relation to the specimen coordinate system (Figure 48).
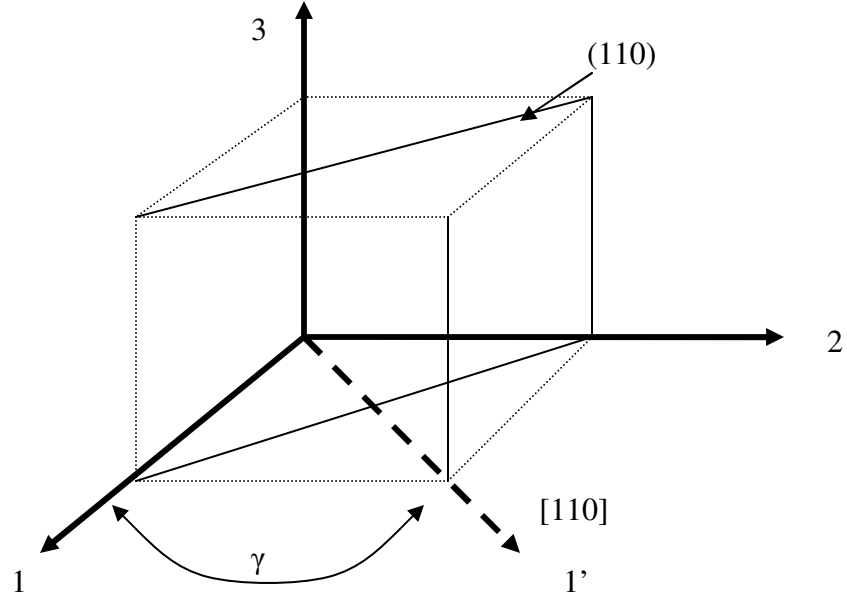
Figure 48. (110) plane and [110] direction of the new compliance value.

$$a_{ij} = \begin{vmatrix} \cos\gamma & \sin\gamma & 0 \\ -\sin\gamma & \cos\gamma & 0 \\ 0 & 0 & 1 \end{vmatrix} \qquad (43).$$

Solving for the compliance value in the direction normal to the (110) plane and

contracting the tensor notation to matrix notation:

$$S_{11}^{'} = S_{11}(\cos^4\gamma + \sin^4\gamma) + 2S_{12}(\cos^2\gamma\sin^2\gamma) + S_{44}(\cos^2\gamma\sin^2\gamma) \qquad (44),$$

$$\frac{1}{E_{(110)}} = S_{11}^{'} = S_{11} = 0.26 \cdot 10^{-11} Pa^{-1} \qquad (45).$$

Equations (44 and 45) confirm that tungsten is isotropic and there is no directional

dependence in the <110> direction. Therefore, 384 GPa can be used for the Young's

modulus of tungsten [63] and equation (38) becomes:

$$\varepsilon_{ij} = \frac{1+v}{E}\sigma_{ij} - \delta_{ij}\frac{v}{E}\sigma_{kk} \qquad (46),$$

where δ_{ij} is Kronecker's delta defined as:

85

$$\delta_{ij} = \begin{cases} 1, & i = j \\ 0, & i \neq l \end{cases} \tag{47}.$$

If the film is in a biaxial stress state and equation (47) is substituted into equation (38), the follow expression is derived:

$$\frac{d_{\phi\psi} - d_0}{d_0} = \frac{1+v}{E}\sigma_\phi \sin^2\psi - \frac{v}{E}(\sigma_{11} + \sigma_{22}) \tag{48}.$$

Equation (48) is a form of the traditional X-ray residual stress equation and it predicts a linear variation of d versus $\sin^2\Psi$. The stress in the S_Φ direction can be obtained directly from the slope of the line fitted to the experimental data measured at various Ψ if E, v and the unstressed plane spacing, d_0, are known. Equation (48) is simplified further by assuming a state of equi-biaxial stress where $\sigma_{11} = \sigma_{22}$:

$$d_\psi = d_0 \frac{(1+v)}{E}\sigma \sin^2\psi + d_0(1 - \frac{2v}{E}\sigma) \tag{49}.$$

Figure 49 is a plot of a 2θ scan, ranging from 39 to 41°, with Ψ being increased from 0 to 30°, in 10° increments. The film irradiated in Figure 49 was an 800 nm thick tungsten film that was deposited at 6 millitorr. Three things can be observed in Figure 49: 1) there is a shift in the 2θ peak with an increase in Ψ, 2) there is a reduction in the intensity of the peak with an increase in Ψ and 3) there is a broadening of the peak with an increase in Ψ.

1200

1000

800

600

400

200

0

Counts

Psi = 0
Psi = 10
Psi = 20
Psi = 30

39   39.5   40   40.5   41

2 Theta
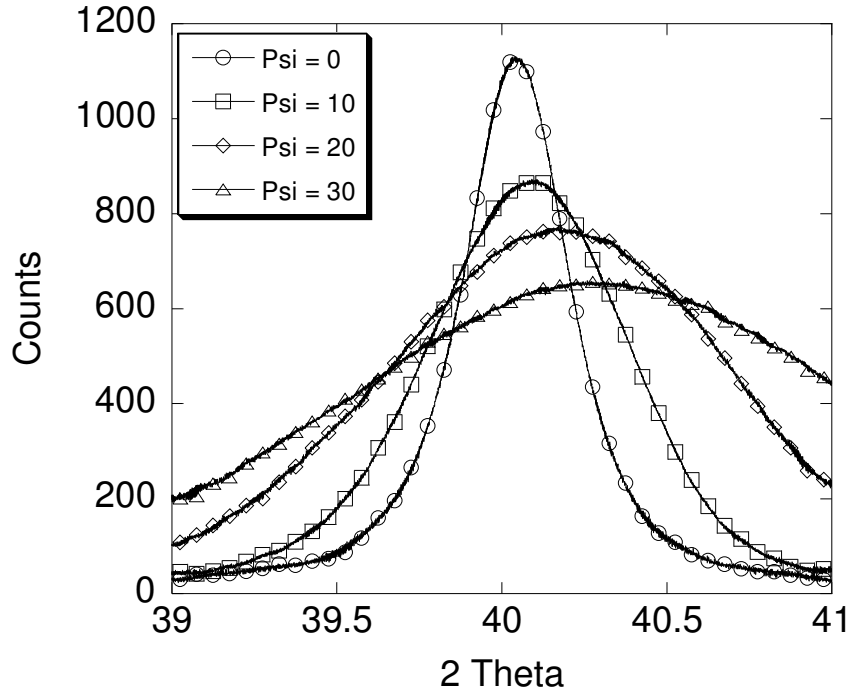
Figure 49. Peak shift with changing ψ angle for the 6 millitorr tungsten film.

The shift in the 2θ peak is a result of the lattice plane spacing being strained and indicates the presence of residual stress. The shift of the peak position to the right in Figure 49 means that d_Ψ is decreasing in length with an increase in the Ψ angle (Figure 50). Figure 50 is a representation of different grain orientations and depicts the effect of compressive residual stress on the (110) plane spacing. At larger angles of Ψ there is a decrease in the (110) plane spacing compared to the unstressed d spacing. At smaller angles of Ψ there will be an increase in d_Ψ compared to the unstressed spacing due to the Poisson's effect. Therefore, the peak positions shifting to the right signify that compressive residual stress is present in the film.

87

$$d_{\psi=0°} > d_{\psi=45°} > d_{\psi=90°}$$
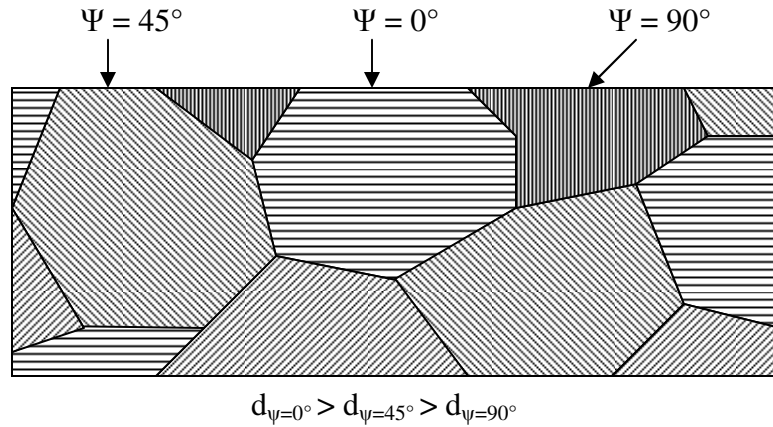
Figure 50. Change in d-spacing with a change in ψ.

The decrease in intensity is expected because an increase in the Ψ angle will result in a reduction of diffracted X-rays reaching the detector. This reduction in diffracted X-rays is the result of a changing tilt of the sample surface, which leads to two problems: 1) the tilt of the surface creates a larger beam size and 2) tilting of the sample surface increases the percentage of the X-rays that will be reflected off the surface. Both of these results will lead to a decrease in the intensity of the diffracted X-rays.

The peak broadening observed in Figure 49 has two major contributors: 1) the presence of non-uniform strain or stress on the macroscopic and microscopic scale and 2) size effects of the crystallites or grains. Macroscopic stress will be defined here as the stress that extends over a distance that is large relative to the grain size of the material, whereas microscopic stress will cover sizes equal to or smaller than the grain size [64-66]. The effect of macroscopic stress on peak broadening is easy to envision when the beam area is considered along with the non-uniform curvature measured earlier on the tungsten samples (Figure 34 and Figure 35). By knowing the geometry of the system being used, the X-ray beam area can be calculated. For the Philips X'Pert Pro the X-ray

beam length was calculated to be 16.33 mm when $\omega = 20°$, by use of the following

equation:

$$L = \frac{R \cdot \sin\omega \cdot \sin\delta}{\left[\sin^2\omega - \sin^2\left(\frac{\delta}{2}\right)\right]} \qquad (50),$$

where R is the radius of the goniometer, δ is the incident beam divergence and ω is the

angle between the incident beam and the sample surface. The width of the beam was

calculated to be 19.08 mm by the following equation:

$$W = (M - 3) + \alpha(R - f) \qquad (51),$$

where M is the mask size, α is the angle of the soller slits and f is the distance from the

middle of the X-ray tube to the crossed slits. The beam area ($A^{'} = A/\cos\Psi$) will have a

further increase in size when the Ψ angle is increased. This is a fairly large X-ray beam

area and should be considered when analyzing the X-ray results for residual stress. Using

the wafer curvature method for calculating stress, it was observed that the stress could

vary by a few hundred mega-Pascals across a 1 to 2 cm length. With that in mind, a

significant change in d_Ψ would be expected across the beam area and would help explain

the peak broadening.

The effects of microscopic stress are a little less obvious to picture and can vary

from point to point within the crystal lattice altering the lattice spacing. The microscopic

stress may vary within the grain due to defects introduced during deposition. This could

include trapped foreign atoms and forward sputtering effects. The source of trapped

foreign atoms would be from the Ar working gas used during sputter deposition of the

tungsten films. The atomic peening and forward sputtering effects could also create a

89

gradient in strain through the film thickness, additionally contributing to peak broadening.

Small grain size will also cause a broadening of the diffracted beam. The Scherrer formula can be used to estimate the average size, *D*, of very small grains by measuring the breadth width at half the maximum intensity, *B*:

$$D = \frac{K \cdot \lambda}{B \cdot \cos\theta}$$ (52),

where θ is the peak position, λ is the X-ray wavelength and *K* is dependent on the shape of the grains and is normally chosen to be 0.9 or 1.0 [67]. By measuring the breadth width at half the maximum intensity for the $\Psi = 0°$ peak in Figure 49, the average grain size, *D*, was calculated to be 223 Å using the Scherrer formula. Due to the reduction in peak intensity and increase in peak broadening at larger Ψ angles, measurements were normally performed at $\Psi < 45°$.

Before the calculation of residual stress was made using the peak positions observed in Figure 49, a biaxial state of stress had to be confirmed. To do this, measurements were taken at equal positive and negative Ψ angles. If the film is in a state of biaxial stress, the d-spacing at negative and positive Ψ angles should be the same. The results of this test can be observed in Figure 51, confirming that the film is in a state of biaxial stress. If the residual stress of the film had not been biaxial, the plot would have formed an ellipse, similar to what was depicted in Figure 46 b).

90
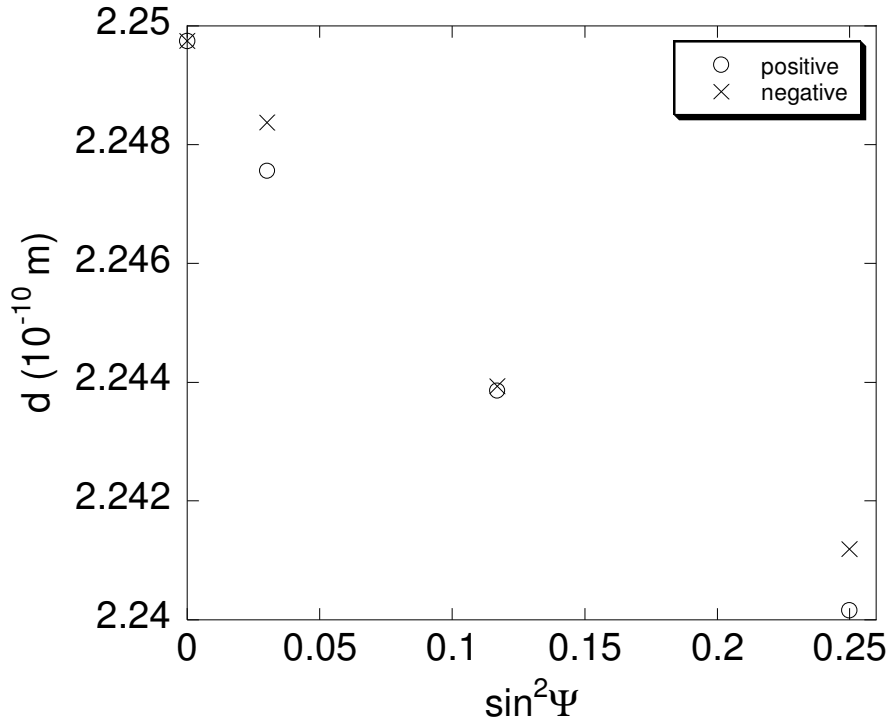
Figure 51. Sin²Ψ technique performed in the positive and negative Ψ directions.

To accurately determine the position of the peaks in Figure 49, there are several methods to choose from [68, 69]. Some common methods include half-value breadth method, centroid method, Gaussian fit and parabolic fit. No matter what method is chosen for the peak position determination, consistency must be established during the $\sin^2\Psi$ test when measuring the shift in 2θ. Figure 52 demonstrates the Gaussian and parabolic fit method for determining the 2θ peak position. Only the top 15% of the peak intensity is used for determining the peak for both methods. For this case, the parabolic fit had a correlation coefficient of 0.99084 and the Gaussian fit had a correlation coefficient of 0.99265. Both methods found the identical 2θ peak of 40.046°

91
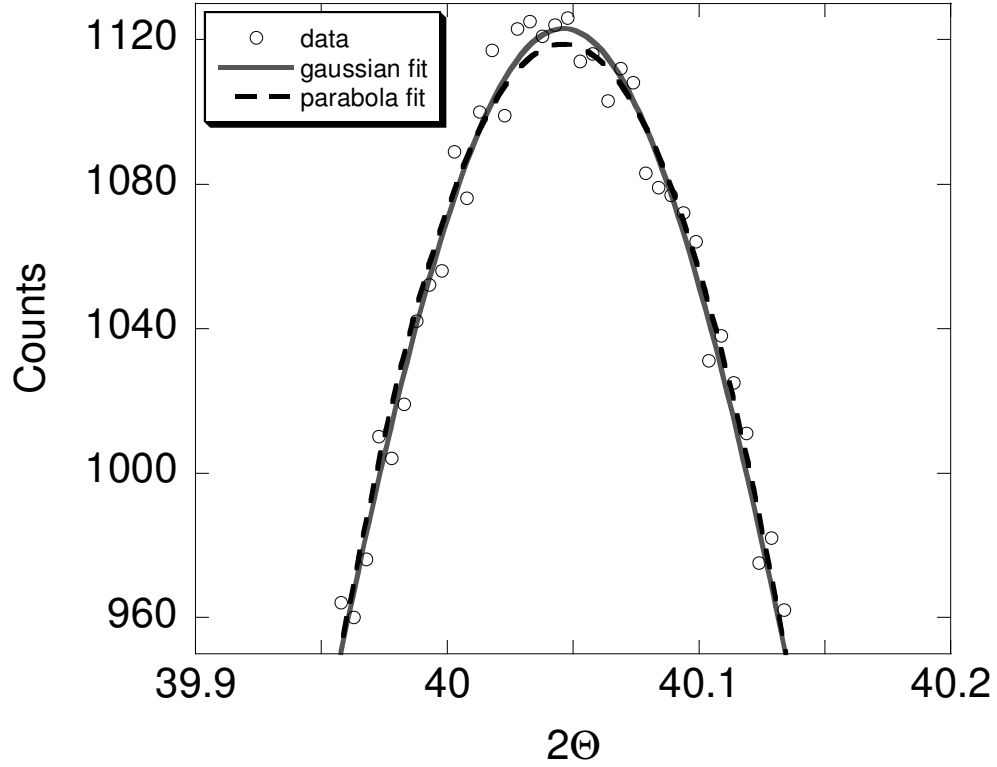
Figure 52. Peak determination by fitting a parabola.

After the 2θ peaks are found, the lattice plane spacing is calculated using Bragg's

law and is plotted against $\sin^2\Psi$. The slope of the plot in Figure 53 is equal to:

$$\frac{\partial d_\Psi}{\partial \sin^2 \Psi} = \left(\frac{1+v}{E}\right)\sigma_\Phi \cdot d_0 \qquad (53),$$

which can be rearranged to solve for the stress σ_Φ. As predicted from equation (41), for

an isotropic film that is in a state of biaxial stress, there is a linear relationship between

d_Ψ and $\sin^2\Psi$. Normally the lattice spacing measured at $\Psi = 0$ is substituted for d_0

because the unstressed lattice spacing may not be known. For most elastic materials the

elastic strains may introduce at most, 0.1% difference between the true value of d_0 and d_Ψ

at any angle Ψ. Since d_0 is a multiple to the slope, the total error introduced by this

assumption in the final stress value is less than 0.1 % [69]. Determination of d_0 can also

92

be made by knowing the lattice parameter of the material and what type of unit cell it has. For the case of a cubic unit cell:

$$\frac{1}{d_{(hkl)}^2} = \frac{h^2 + k^2 + l^2}{a_0^2} \tag{54},$$

where *h*, *k* and *l* represent the Miller indices of the adjacent planes being considered and a_0 is the lattice parameter. The lattice plane spacing for (110) planes in tungsten, with a lattice parameter of 3.1652 Å [70], was calculated to be 2.2381 Å. The unstressed lattice plane spacing can also be found with the use of equation (49) from the $\sin^2 \Psi$ technique. For $\Psi = \Psi *$, $d_{\psi*} = d_0$, and assuming equi-biaxial stress, equation (49) becomes:

$$\sin^2 \Psi = 2 \frac{v/E}{(1+v)/E} \tag{55}.$$

The $\Psi *$ angle (41°) can then be solved for by inputting the values of the Young's modulus and the Poisson's ratio for tungsten, and would be the Ψ angle where d_Ψ is equal to the unstressed *d* spacing.

The $\sin^2\Psi$ tests that were initially conducted on the (110) peak for the tungsten samples all resulted in extremely high values of residual stress. This is due to the fact that the planes spacing will be measured less accurately at smaller 2θ angles [67]. The decreased accuracy at lower 2θ angles is the result of the X-ray beam being out of focus. The higher 2θ angles had originally been avoided because of low intensity and broadened peaks. Since the (110) peak resulted in erroneous stress results the $\sin^2\Psi$ test was conducted on the (321) peak at $2\theta = 131°$. Figure 53- Figure 55 are the results of the $\sin^2\Psi$ test on tungsten films deposited at 4, 6 and 10 millitorr.
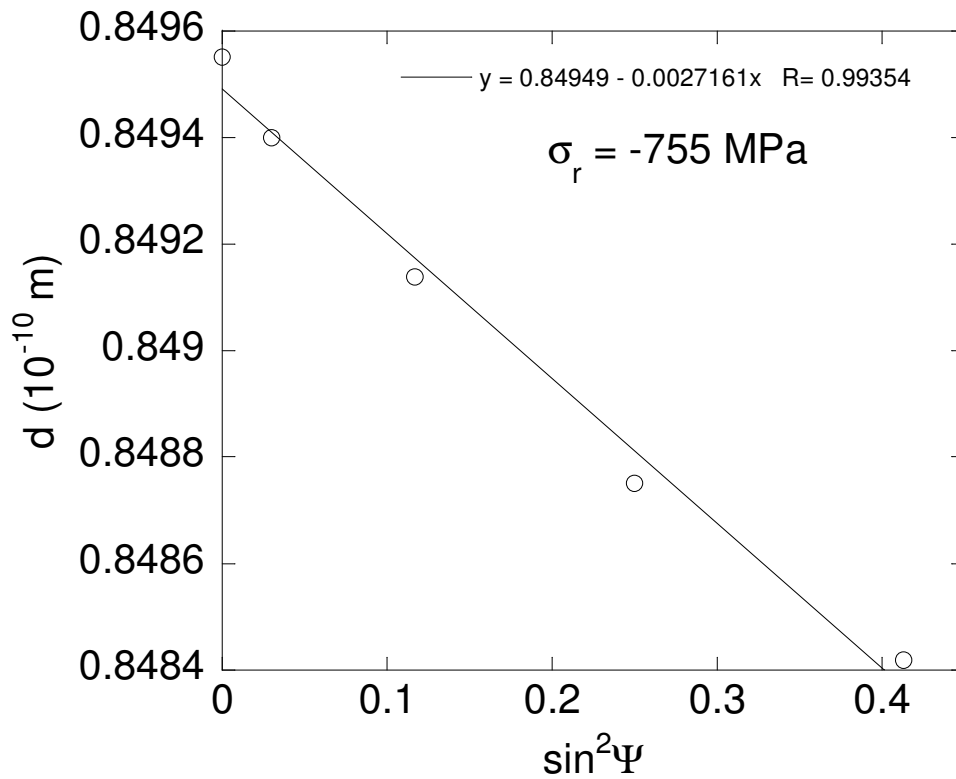
93

Figure 53. Sin$^2\psi$ plot for tungsten film deposited at 4 millitorr Ar pressure.

Figure 54. Sin$^2\psi$ plot for tungsten film deposited at 6 millitorr Ar pressure.
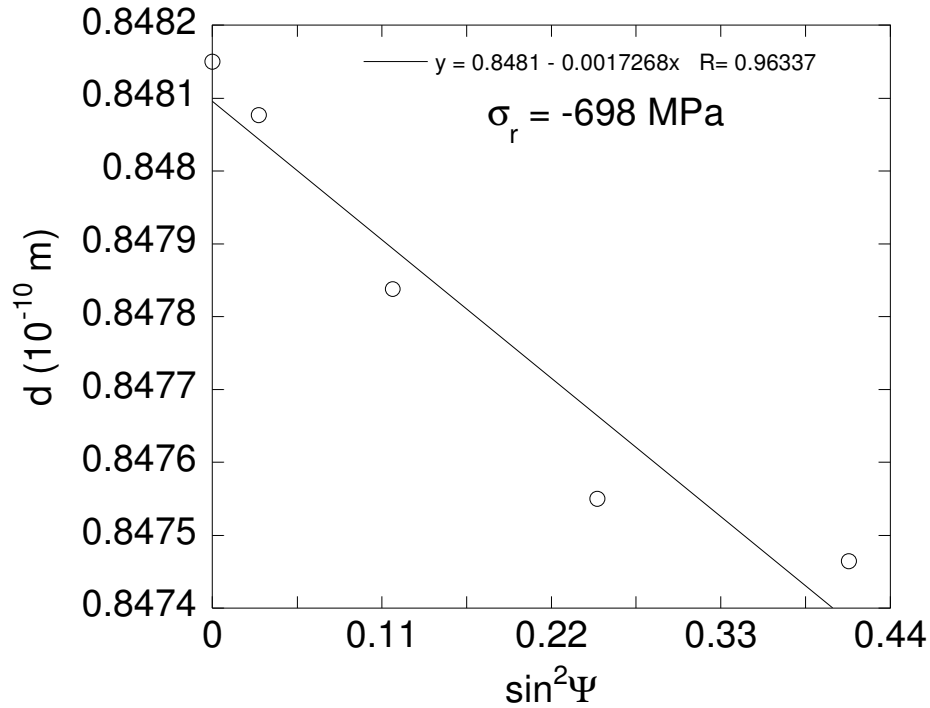
94

Figure 55. Sin²ψ plot for tungsten film deposited at 10 millitorr Ar pressure.

The X-ray beam was focused on the wafer center for the tungsten film deposited

at 4 millitorr Ar pressure. It resulted in a negative slope indicating compressive residual

stress with the results presented in Figure 53. The -1.76 GPa of stress calculated using

the $\sin^2\Psi$ technique is approximately 200 MPa higher than what was calculated using the

curvature technique. The results of the tungsten film deposited at 6 millitorr Ar pressure

are presented in Figure 54. Again, there is a decrease in the interplanar spacing with an

increase in the Ψ angle, which again indicates compressive residual stress. As before the

X-ray beam was focused on the wafer center and the residual stress was calculated to be -

755 MPa, which is approximately 200 MPa higher than the curvature results. The results

presented in Figure 55 are for the tungsten film deposited at 10 millitorr Ar pressure, but

unlike the two other samples the X-ray beam was not focused on the center of the wafer.

The sample had been scribed and broken into two halves for mechanical testing with the

95

Hysitron nanoindenter. Therefore, the $\sin^2\Psi$ test was performed on the remaining half of the wafer with the X-ray beam focused approximately 2 cm from what would have been the wafer center. The residual stress at that location was calculated to be -698 MPa, which is close to what the curvature technique resulted in at the same location.

3.3 Summary of Stress Measurements

The stress results from three different techniques for measuring film stress have been compiled in Table 5. The first column lists the three different tungsten films that were analyzed. All deposition parameters were held constant for the three films, except for the Ar pressure. The second column lists the results using the Flexus 2-300, which is based on measuring a change in curvature before and after film deposition, assuming uniform film thickness and curvature. The stress results listed for the Flexus 2-300 are an average residual stress from 4 measurements taken at 0°, 45°, 90° and 135° stage positions. The results of using the Tencor profilometer are listed in column three of Table **5** 5. The reported values are the stress results calculated at the center and outer edge of the profiles. The values are also an average residual stress taken by rotating the wafer in the circumferential direction. For the tungsten films deposited at 4 and 10 millitorr, the wafers were rotated in 15° increments, whereas the 4 millitorr tungsten film was rotated by 45° increments. The third column lists the results from the $\sin^2\Psi$ technique using X-ray diffractometry. Only one measurement for residual stress was reported for each sample. For the tungsten films deposited at 4 and 6 millitorr Ar pressure the X-ray beam was focused on the wafer centers and for the tungsten film deposited at 10 millitorr Ar pressure the X-ray beam was focused 2 cm from the wafer center.

Table 5. Stress measurement results.

Wafer	Flexus (MPa)	Profilometer (MPa) (Center to Edge)	XRD (MPa)
W 4 millitorr	-893 ± 5	-1500 to -500	-1760 (center)
W 6 millitorr	257 ± 23	-450 to 900	-755 (center)
W 10 millitorr	190 ± 47	1200 to -1000	-698 (R = 2cm)

At first glance, the stress results from the Flexus and the Tencor profilometer do not agree. This would be expected when considering the procedures used for calculating the change in curvature before and after film deposition. The Flexus used two points on the wafer to calculate a single value of curvature for the entire wafer. The points it used for calculating a change in curvature were 1.25 cm from the center of the wafer. If the same points were chosen from the profilometer results for the change in curvature, identical results would be obtained, with both pieces of equipment measuring a change in curvature of 0.025 m^{-1} at 1.25 cm from the wafer center for the tungsten film deposited at 4 millitorr Ar pressure. Figure 56 is a plot of the change in curvature results from the Tencor profilometer with the curvature highlighted at a radial position of 1.25 cm. If the same film thickness and substrate properties were used at this point, the stress results would also be the same since both methods are based off the Stoney equation. A similar procedure for the tungsten films deposited at 6 and 10 millitorr can be conducted to compare the change in curvature and stress calculations when using the Flexus and Tencor tools.

97
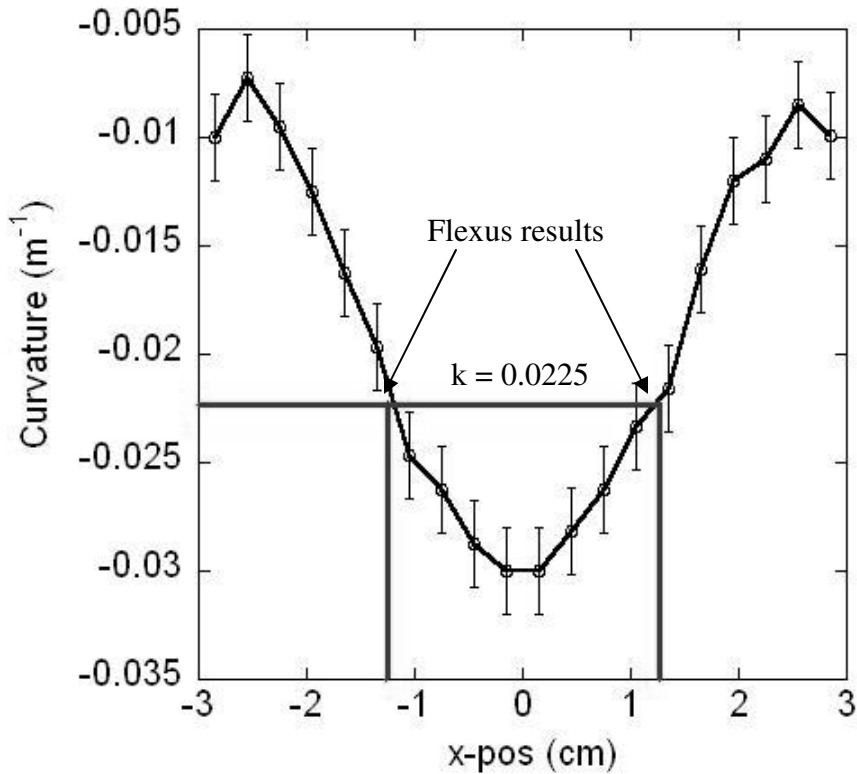
Figure 56. Comparing the curvature found with the Flexus and Tencor tools for the tungsten film deposited at 4 millitorr Ar pressure.

When comparing the curvature methods to the X-ray analysis for calculating residual stress, the results did not compare for small 2θ angles, but better results where obtained at larger 2θ angles. When applying the $\sin^2\Psi$ technique to a larger 2θ angle (131°), the residual stress was calculated to be higher than the wafer curvature techniques by up to 200 MPa. The disagreement in results is thought to be caused by two reasons. First, the segment approach using the Stoney equation is slightly off from the actual stress. Second, the equipment setup with the X-ray diffraction measurements can be improved. The main improvement would be to decrease the spot size of the X-ray beam. A smaller spot size would reduce the peak broadening and complications caused by the curvature of the wafer. Because of the large beam area and curvature of the wafer, the diffracted beam is actually a sum of peaks (Figure 57). Each of these individual peaks

98

are the result of local strains in the film. Therefore, the measured peak shape will depend on the range of local strains, which is dependent on the area of the beam. That is thought to be the primary reason why there is an increase in peak broadening with an increase in Ψ.
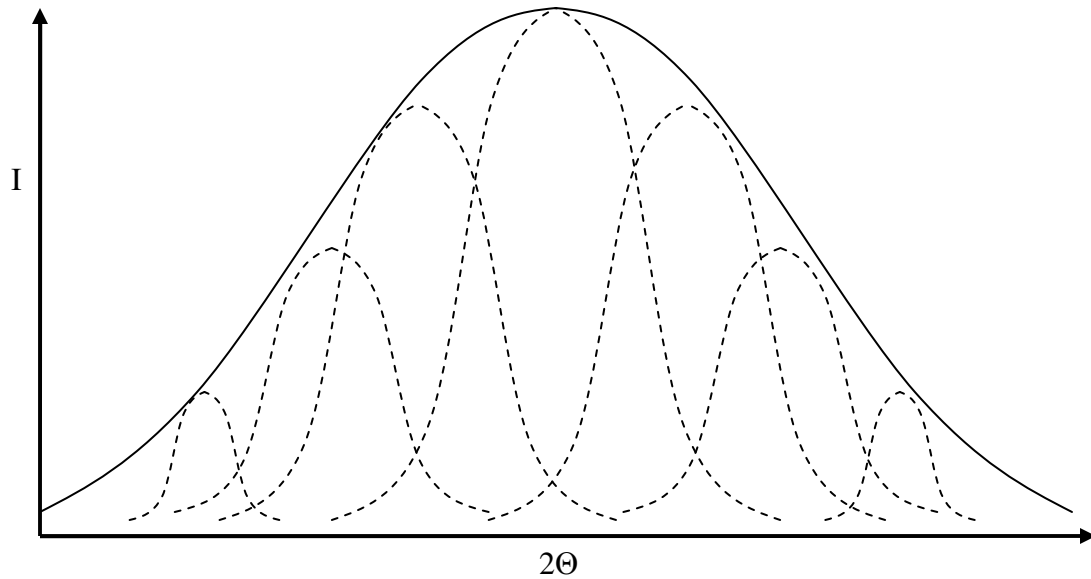
Figure 57. A diffraction peak made up of many peaks.

The curvature of the sample will also create errors in the peak positions due to small misalignments of the instrument and the specimen. One of the first adjustments to be made when loading a sample in the Philips XRD, is finding the correct z-height of the stage. The correct z-height will place the sample surface in the diffractometer center plane. The samples analyzed were centered in middle of the XRD stage to find the correct z-height. However, this guarantees that only the portion of the wafer that is in the XRD stage center is in the diffractometer center plane. Due to the curvature of the wafers and the size of the X-ray beam, most of the sample surface is slightly displaced from the diffractometer center plane. This will result in alignment issues in both the θ

99

and Ψ axes of rotation. In order to correct this problem, the beam area was reduced in size. Reduction of the beam area was possible by reducing the slits size and the angle of the divergence and receiving slits. However, by reducing the mask size and the divergence and receiving slit angles, the intensity of the diffracted beam was also reduced to the point where peak determination was not possible. In general, the accuracy in determining the peak position is proportional to the peak intensity.

To improve the chances of successfully using X-ray diffraction for calculating residual stress in future experiments, a combination of a smaller X-ray beam area and a higher intensity beam should be used. Beam sizes on the order of 100 μm or less in diameter would be ideal, and are normally called mircobeams. Beams with diameters on the order of 10 μm are routinely used with synchrotron radiation, and beams smaller than 1 μm in diameter have been obtained. Along with reduced beam divergence, synchrotron radiation has several advantages over tube sources for X-ray diffraction. The intensity of X-rays delivered is far greater than that of other sources and synchrotron radiation can be tuned to the most advantageous X-ray wavelength needed for the particular application. An alternative to using synchrotron radiation would be to still use a monochromatic beam, but use a collimator or microfocus tube to help reduce the X-ray beam size. The draw back of using collimators is that they will produce an X-ray beam that is weak, requiring very long exposure times. Microfocus tubes can help by reducing the focal spot size during X-ray generation, which results in a higher intensity.

100

Chapter 4

Thin Film Mechanical Testing

4.1 Nanoindentation

Nanoindentation is a convenient and widely used method for testing thin film mechanical properties at the submicron level. It is possible because of high resolution testing equipment that can simultaneously measure force and displacement during an indent (Figure 59). The load-displacement data obtained during one or more cycles of loading and unloading can be used to derive a variety of mechanical properties, including hardness and elastic modulus. The hardness of a material, H, is given by:

$$H = \frac{P_{\max}}{A_c} \tag{56},$$

where P_{max} is the peak indentation load and A_c is the projected contact area under that load. There will be some compliance of the indenter that must be accounted for when using indentation, therefore a reduced modulus is determined and it can be related to the sample's elastic modulus through the following expression:

$$\frac{1}{E_r} = \frac{(1-v_s^2)}{E_s} + \frac{(1-v_i^2)}{E_i} \tag{57},$$

where E_s and v_s are the elastic modulus and Poisson's ratio for the sample. E_i and v_i are the same properties, but for the indenter tip material, which is usually diamond. The reduced modulus E_r is normally expressed as the following:

101

$$E_r = \frac{\sqrt{\pi}}{\gamma \cdot 2} \frac{S}{\sqrt{A_c}} \qquad (58),$$

where S is the stiffness and γ is a correction factor that depends on the strain imposed by the indenter and the Poisson's ratio of the sample. Stiffness can be thought of as the slope of the initial portion of the unloading curve (Figure 58):

$$S = \frac{dP}{dh} \qquad (59),$$

where P is the load and h is the indenter depth. Some indentation depths that must be defined and are shown in Figure 58 are the maximum indentation depth, h_{max}, the contact depth, h_c, and the final indentation depth, h_f.
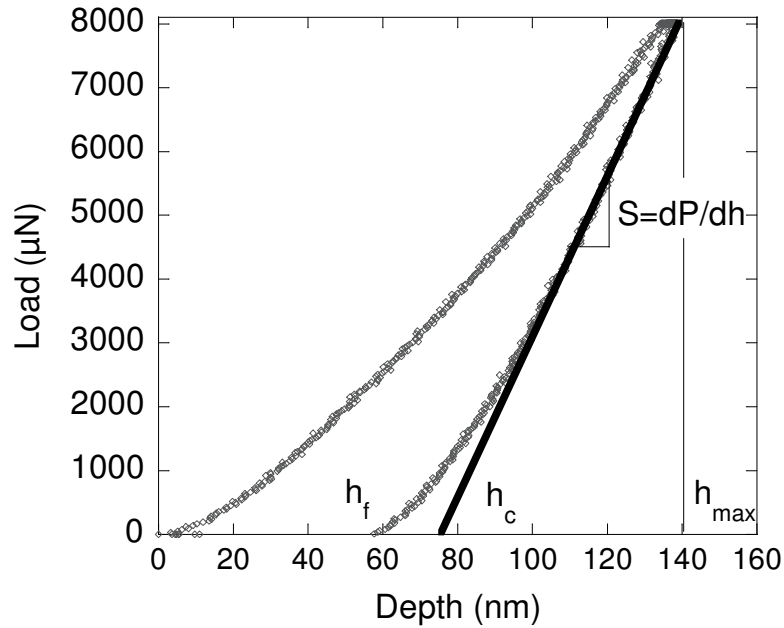
Figure 58. Load-displacement data for an indent into tungsten.

For cones and pyramids, the correction factor γ is given as:

$$\gamma = 1 + \frac{1 - 2v}{4(1 - v)} \cot \psi \qquad (60),$$

where v is the Poisson's ratio of the material and ψ is the indenter half angle. For spheres:

$$\gamma = 1 + \frac{2(1-2v)}{3\pi(1-v)}\frac{a}{R} \tag{61}.$$

Equation 58 has its origins in elastic contact theory and is appropriate for any indenter that can be described as a body of revolution of a smooth function and is not limited to a specific geometry.

Figure 59 is a plot of four different types of materials that were indented to approximately the same maximum load. It can be seen that the load-displacement curves are quite different for the four different materials. The difference in the load-displacements curves is the result of different mechanical properties. In the case of sapphire, which has a high modulus and hardness, the loading and the unloading portions of the curve matched up resulting in a perfectly elastic indent. In comparison the low-k film has a relatively low modulus and hardness which results in large amounts of plastic deformation for the same maximum load. The amount of elastic recovery is seen in the load-displacement curve as the difference between the maximum indentation depth and the final indentation depth. Along with determination of thin film hardness and elastic modulus, additional film properties such as adhesion and fracture toughness can be determined using nanoindentation.
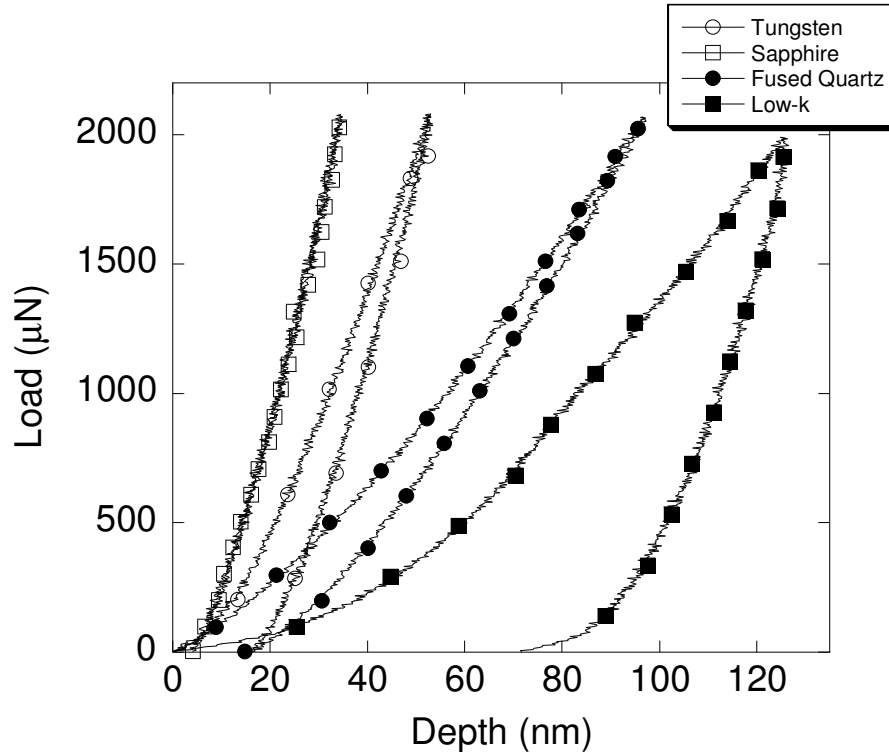
Figure 59. Load-displacement plots for different types of films.

The contact mechanics of nanoindentation can be quite complex, therefore, a detailed understanding of the information contained in the loading and unloading curves is required. The complexity of indentation is the result of both elastic and plastic deformation occurring during loading, as well as the non-uniformity of stress and deformation fields in the vicinity of contact. For this reason, many of the methods used for assessing mechanical properties by nanoindentation are empirical. One such example is the determination of the tip area function. Similar to hardness tests done at the macroscopic level, nanoindentation also requires knowledge of the residual indent impression for determining mechanical properties. However, because of the nanometer-scale of the indents, direct imaging of the residual impression is not possible or inconvenient at the least.

104

Due to the complexities discussed previously, extraction of the necessary information from the indentation data requires proper calibration of the equipment and knowledge of the materials being analyzed. This is of particular importance when the indentation depth is reduced to the sub 100 nm range. The tip contact depth and the contact area are two parameters on the equipment's side of the analysis that require close attention. On the material's side, the sample's surface roughness, existence of additional surface layers such as oxides or contaminates, sink-in and pile-up must be taken into consideration. Until proper equipment calibration is performed, a thorough understanding of the indentation process is acquired and material effects are factored in, proper analysis of the mechanical properties will be impossible. With that in mind, the first place to start will be discussing the main steps in proper equipment calibration and understanding some of the assumptions made during the analysis of the unloading portion of the load-displacement curve.

4.2 Indentation Calibration and Analysis

No matter what type of experiment is being conducted, or what physical quantity is being measured, proper calibration of the testing equipment must be the first step in the process. If the final result depends on measuring multiple quantities, proper calibration is even more crucial to avoid an accumulation of error. Nanoindentation is such a case where multiple quantities are needed for the final determination of mechanical properties. So far it has been mentioned that determination of the reduced modulus and hardness are based on the analysis of the load-displacement curves. It will be shown that they are specifically dependent on accurate knowledge of the load, displacement and indenter

contact area. If any of the three are inaccurate, it can be expected that there will be errors in the reported values of a material's reduced modulus and hardness.

A Hysitron Triboindenter was used for the indentation tests, which has a transducer that is based on a three-plate capacitive design that provides excellent resolution of force and displacement (Figure 60). An indenter tip is screwed into a tip holder, which is located on the center plate of the transducer. The center plate is spring mounted to the transducer housing. The indentation force is electrostatically actuated by applying a DC bias to the bottom plate of the capacitor. This creates an electrostatic attraction between the center plate and the bottom plate, pulling the center plate and the indenter tip downward.
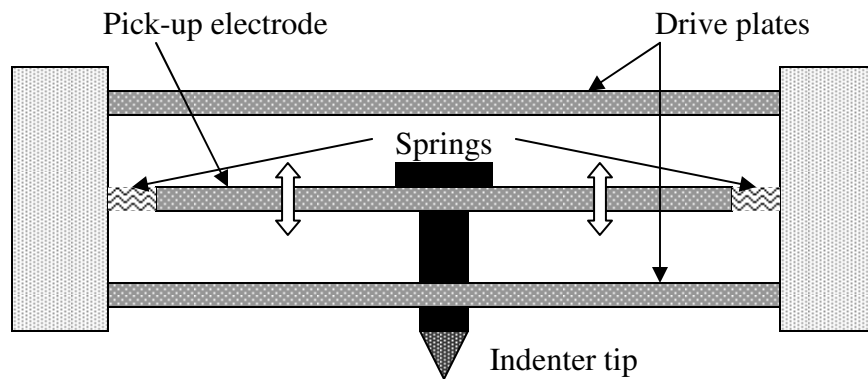
Figure 60. Schematic of the TriboIndenter transducer.

The indenter force can be calculated from the magnitude of the voltage applied using the following expression [72]:

$$F = F_E V^2 \qquad (62),$$

where F_E is the electrostatic force constant which depends on the area, A, of the plates, the spacing, d, between the center and the outer plates and k is the dielectric constant of the air between the plates [73]:

106

$$F_E = \frac{k}{2}\frac{A}{d^2} \tag{63}.$$

The maximum force that can be applied by the transducer is about 10 mN, with a 1 nN resolution. The displacement of the tip is measured by the transducer's center plate which acts as a pickup electrode. The two outer plates, or drive plates, are driven by AC signals 180° out of phase with each other. Because the outer plates are 180° out of phase, the electric field potential is a maximum at the drive plates and zero at the center where the signals' opposite polarity cancel each other. Since the plate spacing is relatively small compared to the lateral dimension, the electric field potential varies linearly between the plates. The displacement is easily determined since the pickup electrode is at the same electric potential as the electric field between the outer plates. The maximum displacement of the transducer is 20 µm, with a 0.04 nm resolution.

Due to its capacitor-based operation, it is critical to calibrate the transducer before each use. Temperature and humidity changes will affect the capacitance properties of the transducer. Therefore, an air indent is performed prior to operation, which determines an electrostatic force constant and a displacement scale factor. The electrostatic force constant relates the force output of the plate to an applied voltage and the displacement scale factor relates the displacement of the center plate to a measured voltage output. Accurate calibration of the two constants is necessary for correct determination of the load-displacement curve. Along with transducer calibration, the material stiffness, tip area function and machine compliance need to be determined for proper analysis of the reduced modulus and hardness.

4.2.1 Indentation Stiffness

As previously described in equation 58 of Chapter 2, the reduced modulus depends on the unloading stiffness and the contact area. The stiffness has been defined as the slope of the initial portion of the unloading curve in equation 59 and was shown in Figure 58. The unloading portion of the load-displacement plot is of interest because it only consists of the elastic recovery. Oliver and Pharr have shown that a power law relationship describes the top portion of the unloading data through the expression [74]:

$$P = \alpha(h - h_f)^m \tag{64},$$

where P is the indentation load, h is the displacement, h_f is the final displacement after complete unloading, α and m are constants that depend on the indenter geometry and the material being tested.

The top 65 % of an unloading curve from a 5300 μN indent performed on fused quartz has been fitted with the Oliver-Pharr power law relationship in Figure 61. The final values of h_f, α and m have been determined from regression analysis of the experimental data, giving a correlation coefficient of 0.99942. The unloading stiffness, S, can then be established by differentiating equation 64 and evaluating it at the maximum penetration depth, h_{max}:

$$S = \frac{dP}{dh} = m \cdot \alpha(h - h_f)^{m-1}\Big|_{h=h_{\max}} \tag{65}.$$
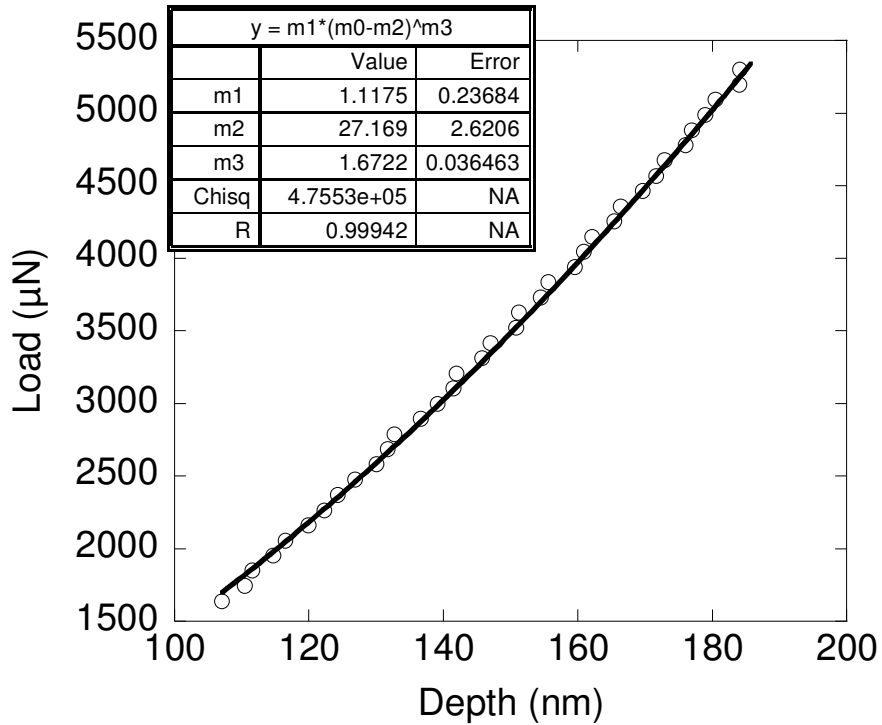
Figure 61. Oliver-Pharr power law fit for the top 65 % of an unloading curve from fused quartz.

Pharr and Bolshakov used finite element simulations to reproduce the experimentally observed unloading behavior [75]. From those simulations a better understanding of the origin of the power law exponents has been obtained. It is based on the concept of an "effective indenter shape", with the indenter geometry determined by the shape of the plastic hardness impression formed during loading. Their model provides the means by which the material constants in the power law fit can be related to more fundamental material properties such as the elastic modulus and hardness. With the stiffness analysis now outlined, the only remaining variable for determining the reduced modulus is the indenter contact area.

4.2.2 Tip Area Function

Due to the small scale of nanoindentation, imaging of residual contact impressions is inconvenient at the least, therefore the determination of a tip area function as a function of indentation depth is necessary. The contact area at peak load is used in calculating both the hardness and the reduced modulus. It is determined by the geometry of the indenter and the contact depth h_c, which is defined in both Figure 58 and Figure 62. The contact depth is the difference between the maximum displacement, h_{max}, which is experimentally measured, and the displacement of the surface at the contact perimeter, h_s, which can be extracted from the load-displacement data.
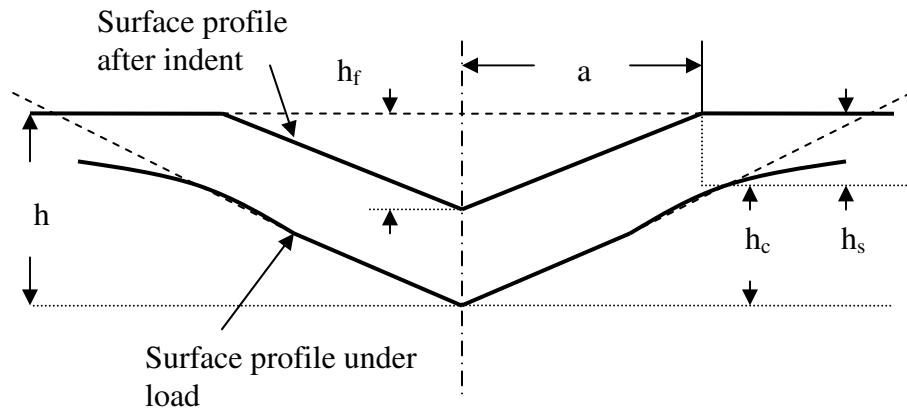
Figure 62. Schematic of indentation geometries.

The displacement of the surface at the contact perimeter depends on the indenter geometry and for conical indenters Sneddon found this to be [76]:

$$h_s = \frac{(\pi - 2)}{\pi}(h - h_f) \tag{66}$$

Since Sneddon's solution applies only to the elastic component of the displacement, the quantity (h-h_f) is used rather than h by itself. Additionally, Sneddon's force-displacement relationship for the conical indenter yields:

110

$$(h - h_f) = 2\frac{P}{S} \qquad (67).$$

By substituting equation 67 into equation 66 and because the contact area of interest is determined at the peak load, the following expression for h_s is derived to be:

$$h_s = \eta\frac{P_{max}}{S} \qquad (68)$$

where the constant η depends on the indenter geometry. The indenter geometry constant has been determined to be 0.72 for conical tips, 0.75 for Berkovich tips and 1.0 for a flat punch [74 - 76]. Combining equation 68 with the definition of the contact depth, h_c, the following equation is derived:

$$h_c = h_{max} - \eta\frac{P_{max}}{S} \qquad (69).$$

An extended explanation of the contact depth was necessary to show that its derivation is empirically based, and any significant changes in tip geometry must be accounted for. For example, a cube corner tip will have a different contact depth than a conical tip even if they are indented to the same maximum depth. This is important to note since the tip area function is defined in terms of the contact depth.

The tip area function is found experimentally by carrying out indents to various contact depths on a standard reference sample. Fused quartz is a common choice and is assumed to have a constant modulus and hardness as a function of depth. Determination of the area function should be confined to the depth range of the intended indents in the sample of interest, with numerous indents performed. Typical experiments conducted here to determine the area function included a total of 50 indents, broken up into 5 groups, performed at various locations on a fused quartz sample with the contact depth

111

ranging from 10 to 200 nm. The 5 groups of indents had the same load range and were intended to make sure that there was repeatability between the groupings. A Berkovich indenter was used for all the modulus and hardness tests here, and it has an ideal area function of $A(h_c) = 24.5 \cdot h_c^2$. The ideal area function will provide an accurate description of the contact geometry at larger contact depths, but will be grossly inaccurate at shallow indents.

A comparison of the ideal and experimentally determined contact area for a Berkovich indenter is shown in Figure 63. It's not until after a contact depth of approximately 220 nm is reached that the experimentally determined contact area matches up with the ideal contact area. With the Berkovich geometry, inaccuracies will arise at the identer tip point, where manufacturing of a perfectly sharp tip is impossible. In reality, the indenter tip is blunted and can be described as having a radius. Oliver and Pharr have suggested the use of an eight parameter function to compensate for the differences between the ideal and actual tip geometry [74]:

$$A(h_c) = 24.56 \cdot h_c^2 + C_1 \cdot h_c^1 + C_2 \cdot h_c^{1/2} + C_3 \cdot h_c^{1/4} + \ldots\ldots + C_8 \cdot h_c^{1/128} \qquad (70),$$

where *C1* through *C8* are constants that will be found through experimental fitting with a reference sample. The first term describes the perfect Berkovich geometry with the others describing the blunting of the tip.
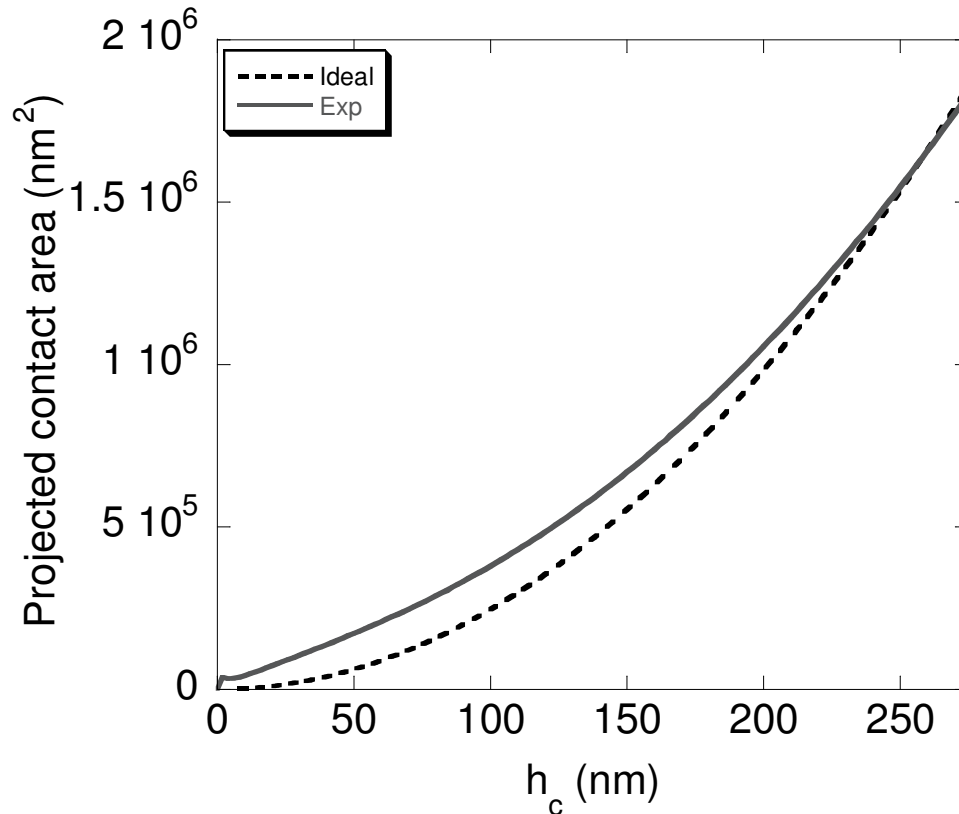
Figure 63. Ideal and experimentally measured Berkovich tip contact areas.

4.2.3 Finding the Tip Radius

One of the most crucial requirements in nanoindentation methods is knowledge of

the indenter tip geometry. Many challenges are presented at shallow indentation depths

due to deviation from the ideal tip geometry. These deviations become increasingly

apparent because an error in contact area will directly affect the reduced modulus and

hardness calculations. So far a method for determining a tip area function has been

presented, which attempts to deal with these deviations. Through the use of atomic force

microscopy observations, the tip of a Berkovich indenter has been considered to have a

spherical shape [77]. The spherical tip shape comparison has been further backed by

finite element simulations [78-80]. An attempt is made here to confirm the validity of

113

treating the tip of the Berkovich indenter as a sphere by applying Hertzian contact theory, where the radius of the tip can be solved for by starting with the following equation:

$$P = \frac{4 \cdot E_r \cdot a^3}{3 \cdot R}$$ (71),

where, E_r is the reduced modulus of the material being indented, a is the contact radius of the indenter and R is the indenter tip radius. It is more useful to relate the load, P, to the indentation depth, h, by eliminating a and getting a relationship between P and h in terms of only the reduced modulus and geometry:

$$P = \frac{4}{3} E_r R^{1/2} h^{3/2}$$ (72).

Using the Hertzian contact theory, indents were performed on a fused quartz sample using both a Berkovich and cube corner indenters. The manufacturer quoted the Berkovich indenter to have a tip radius between 100 and 200 nm and the cube corner tip radius is quoted to be around 50 nm. The indent loads were kept within a range that would result in a perfectly elastic contact. To achieve a perfectly elastic indent, the loading and unloading portions of the load-displacement curve should coincide. This would result in a final contact depth, h_f, of zero. Figure 64 is the load-displacement curve of a 210 µN indent in fused quartz with a cube corner tip. The experimental data is plotted as the open circles and the Hertzian contact with a tip radius of 90 nm was plotted as the solid black line in Figure 64. It can be observed that by assuming a tip radius of 90 nm for the cube corner indenter, the Hertzian contact theory matched up with the experimentally observed data. The same procedure was performed in Figure 65 for the Berkovich indenter, where a tip radius of 170 nm matched up with the experimentally

114

obtained data. For both figures only a percentage of the data points have been plotted, but both show the loading and the unloading data.
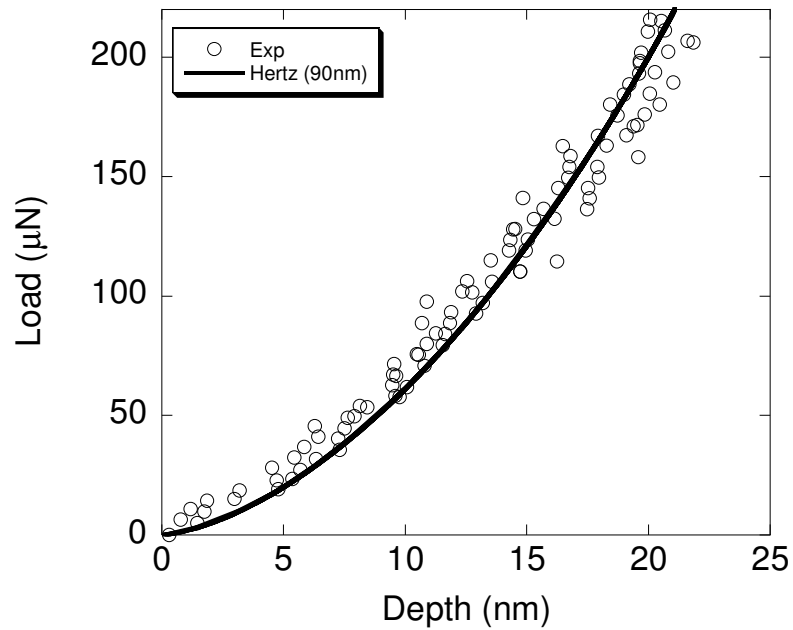
Figure 64. Hertzian contact fit for a cube corner tip.
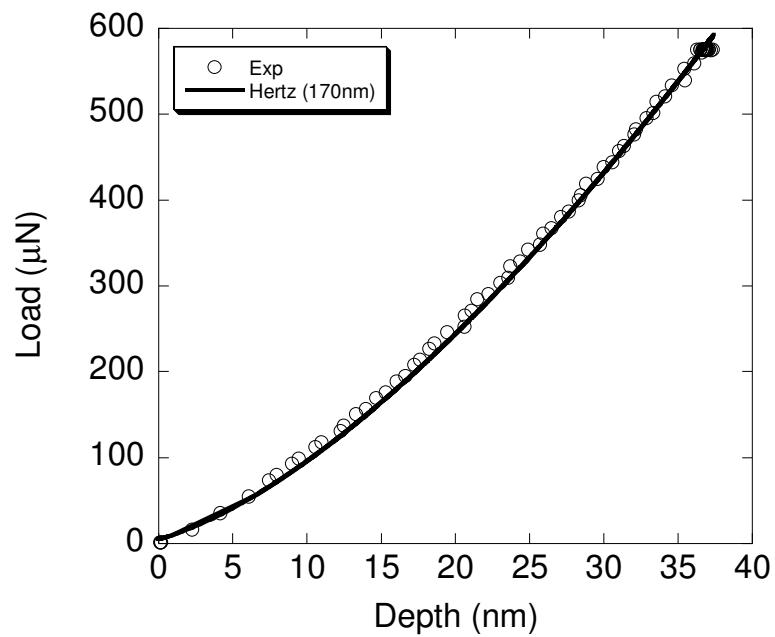
Figure 65. Hertzian contact fit for a Berkovich tip.

115

An alternative way to confirm the tip radius of the indenter is by utilizing an area function that was developed by Thurn and Cook [81]. They developed a two parameter function corresponding to the effective tip radius and effective cone angle of the indenter. They found that the projected area of a tip can be given by a "simplified area function":

$$A(h_c) = \frac{\pi \cdot h_c^2}{\cot^2 \psi} + 4 \cdot R \cdot \pi \cdot h_c + 4 \cdot R^2 \cdot \pi \cdot \cot^2 \psi \qquad (73),$$

where h_c is the contact depth, R is the tip radius and ψ is the included half angle of the equivalent cone. The first term of the expression relates to the ideal cone shape and in the case of a Berkovich tip, ψ would be 70.3°, and is equal to the ideal Berkovich area function, where $A(h_c) = 24.56 \cdot h_c^2$. The remaining terms account for the tip rounding. The final term is a constant that prevents the contact area from going to zero as the contact depth approaches zero. Figure 66 is a plot of the experimentally measured contact area for a Berkovich indenter and the two parameter area function from Thurn and Cook. Using a tip radius of 170 nm that was determined using the Hertzian contact theory, along with the included angle, $\psi = 70$, the experimentally measured contact area and expression developed by Thurn and Cook have been compared. One immediate benefit of using equation 72 over equation 69 for modeling the contact area is seen when the contact depth approaches zero. Equation 69 forces the contact area to be zero, at zero contact depth, which creates an inconsistency in the area function at contact depths below 10 nm. Thurn and Cook's model handles the shallow contact depths better by starting with an initial contact by the use of the final term in equation 69. Although the Thurn and Cook model was preferred here at shallower contact depths, significant deviation from the experimentally measured contact area was observed at larger indentation depths.

116
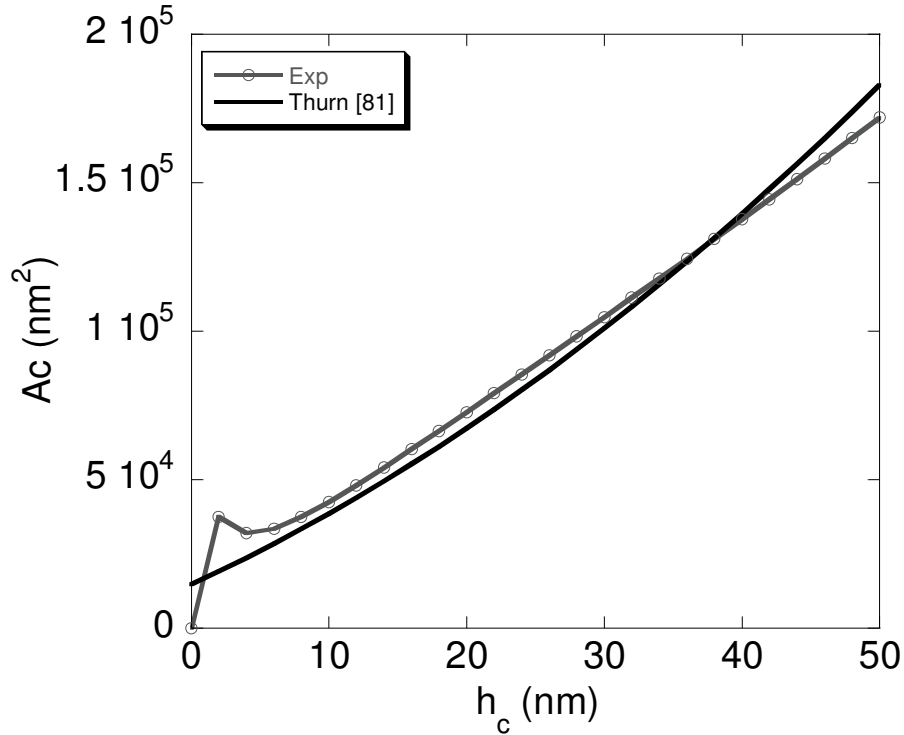
Figure 66. Comparison of Thurn and experimentally measured area function at shallow depths.

The discontinuity in the area function at shallow indentation depths created by equation 69 could explain why there is a larger variation in calculated hardness in this region. Difficulties in compensating for the spherical tip geometry using equation 69 could also explain why the hardness often initially increases with the indentation depth in the nanometer regime. Figure 67 is a plot of hardness results as a function of contact depth for a 200 nm thick gold film on silicon. The hardness was calculated to be 2 GPa at a contact depth of 15 nm and it plateaus out at a maximum hardness of 3.5 GPa starting at a contact depth of 100 nm. Xue et al. have developed a model to explain the depth dependence of the nano/micro indentation hardness based on a theory of strain gradient plasticity [82]. This result contradicts many observations at the microindentation scale, where the hardness decreases with an increase in indentation depth [83, 84]. The main

117

contributor suspected in those cases is geometrically necessary dislocations (GNDs) that accumulate underneath an indenter, providing additional work hardening of the material. It is thought that the density of GNDs is inversely proportional to the indentation depth, causing increased hardness at shallower contact depths.

With the complexity of the indenter tip described and its possible effects on modulus and hardness covered, the only calibration procedure remaining is the machine compliance. So far it has been observed that the load and displacement are continuously being measured during indentation. It must be pointed out that some of the displacement will be contributed by the equipment and it must be accounted for. If not, it will be shown that inaccuracies in the reduced modulus and hardness will occur.
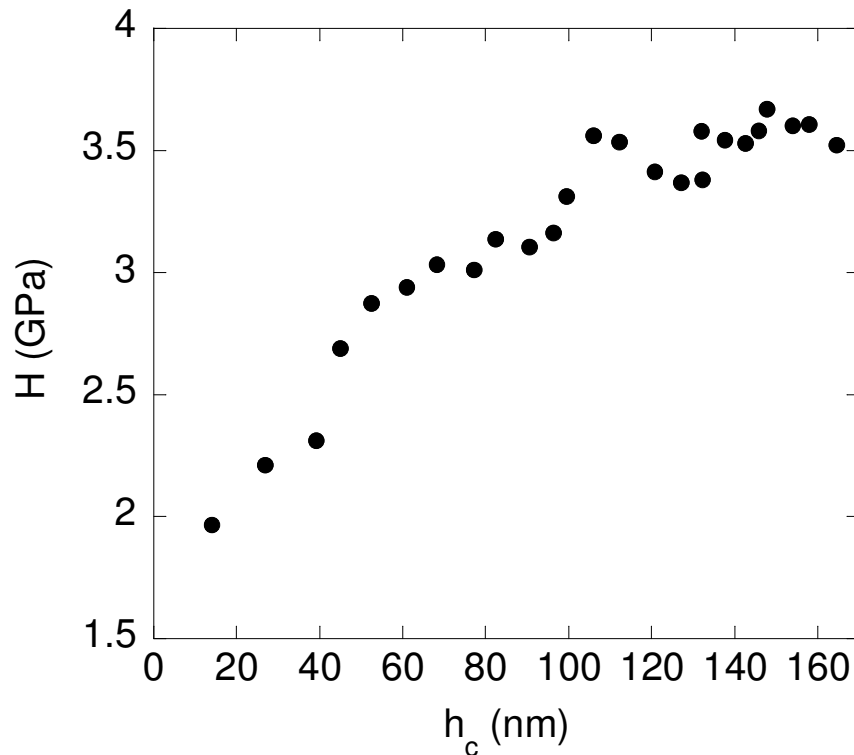
Figure 67. Increase in hardness for a 200 nm gold film as a function of contact depth.

4.2.4 Machine Compliance of the Indenter

The total amount of compliance experienced during indentation will be a combination of two constituent parts, the specimen and the testing equipment. The contribution of the equipment (machine) compliance is especially important when conducting deep indents and analyzing high modulus materials. The significance of not accounting for machine compliance on a high modulus material can be observed in Figure 68. In Figure 68 indents were executed to a range of loads in an 850 nm tungsten film. There is approximately a 50 GPa difference in the reduced modulus when not compensating for machine compliance.
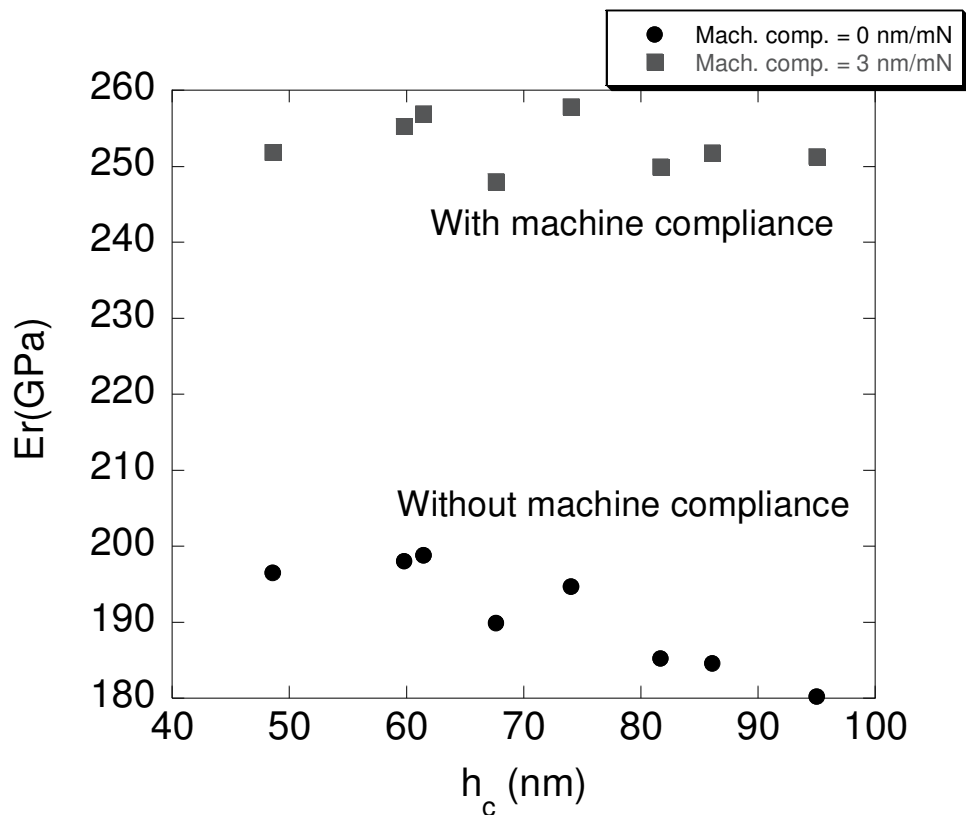
Figure 68. Effect of machine compliance on high modulus material.

Using an incorrect machine compliance may go unnoticed for some time depending on the types of materials that are being tested. Fused quartz is a typical

reference sample used for calibrating the tip area function, but it is relatively compliant compared to many other materials. When only examining the results for the reduced modulus of fused quartz, inaccurate machine compliance may go unnoticed as can be seen in Figure 69. It's not until the hardness data is analyzed will discrepancies appear for fused quartz (Figure 70). Not only are the hardness values overestimated when using the wrong machine compliance value, but the hardness data shows a more significant change as a function of the contact depth.
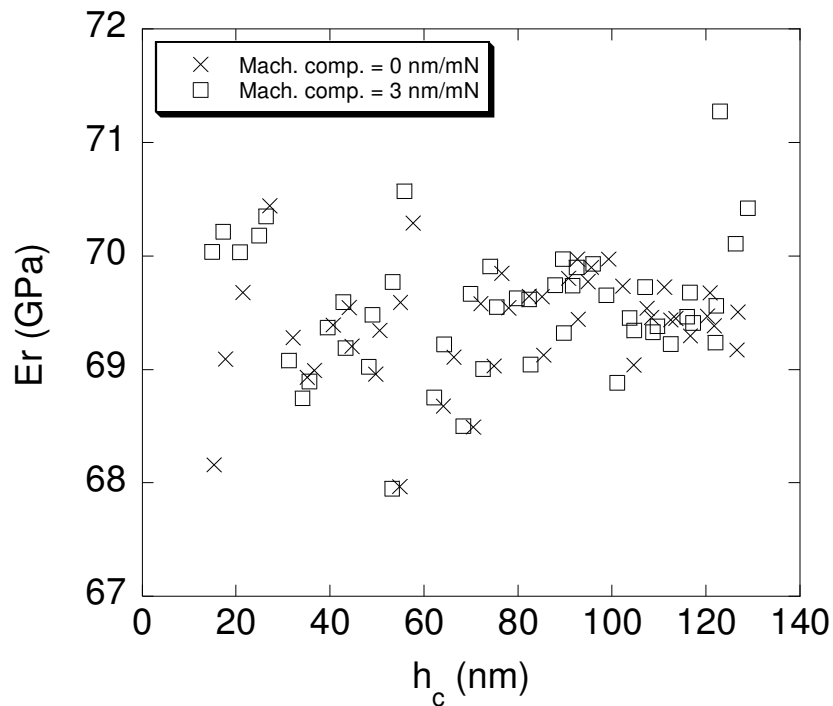
Figure 69. The effect of machine compliance on the reduced modulus of quartz.

One way to initially determine the correct machine compliance when testing fused quartz is by an iteration method. The objective of the method would be to adjust the value for machine compliance until the calculated hardness values start to level off at deeper contact depths. In general, an indentation depth that is less than 1/3 of the tip radius will show considerable change in hardness. This effect can be seen in Figure 70

120

when using the correct machine compliance of 3 nm/mN. By compensating for machine compliance the hardness of fused quartz starts to level off after the first 50 nm of contact depth. The manufacturer suggests that the hardness of fused quartz should be between 9 and 13 GPa when using a Berkovich indenter. Over time the tip will continue to wear down, which increases the tip radius and results in a higher value of hardness.
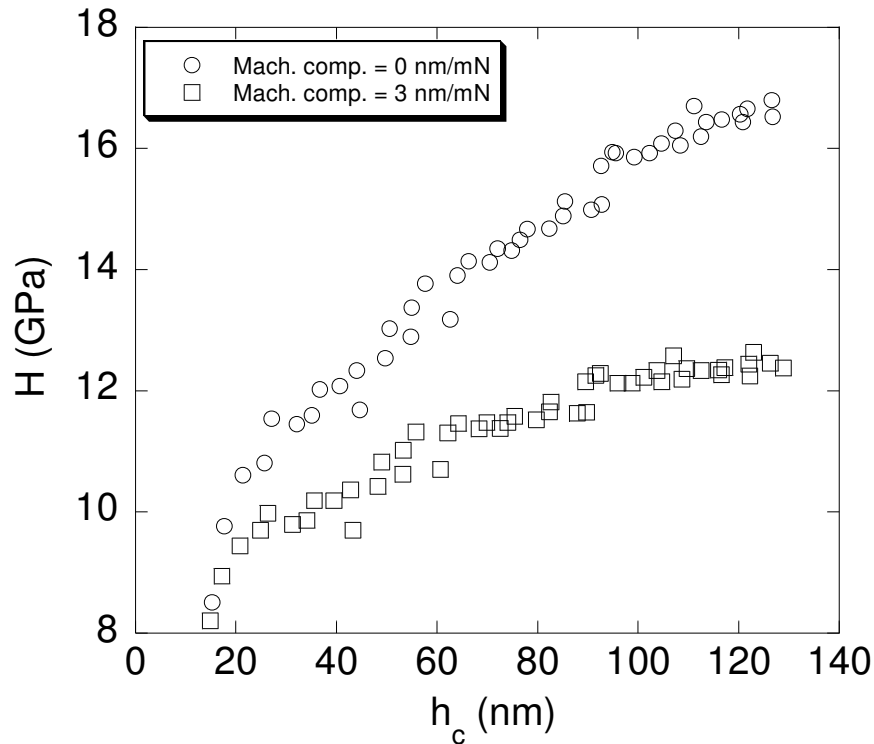
Figure 70. The effect of machine compliance on the hardness of fused quartz.

A more conclusive way to determine the machine compliance is by modeling the load frame and the specimen as two springs in series, in which case:

$$C = C_s + C_m \tag{74},$$

where C is the total measured compliance, C_s is the sample compliance and C_m is the machine compliance. Since the sample compliance during elastic contact is given by the inverse of the contact stiffness, S, equation 55 and equation 74 combine to yield:

121

$$C = C_m + \frac{\sqrt{\pi}}{2 \cdot E_r} \frac{1}{\sqrt{A_c}} \qquad (75).$$

If the reduced modulus is constant, a plot of C versus $A_c^{-1/2}$ should be linear for a given material and C_m can be found as the y-axis intercept (Figure 71).
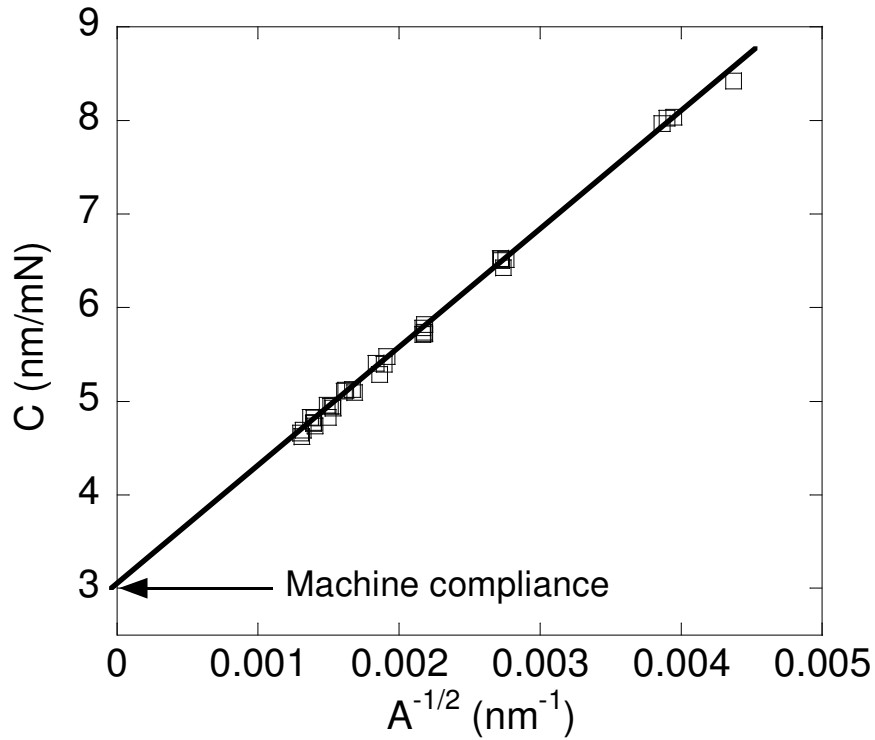
Figure 71. Machine compliance check.

With the proper machine compliance determined, all the necessary equipment calibrations have been covered. Proper equipment calibration is often taken too lightly, resulting in poor confidence in the final data. Sometimes the testing of new materials will lead to unique results that the user has not seen in the past. Before a hypothesis can be drawn relating the results to material properties, the user must be sure that the results are not equipment related. It is also possible to see some material effects that result in misleading results.

122

4.3 Material Effects

Along with the equipment effects already discussed, calculation of a film's modulus and hardness will also be affected by film and substrate material effects. When reporting thin film modulus and hardness, it is common to report them as a function of the contact depth. Very rarely will the thin film modulus and hardness be constant through the range of contact depth. This lack of consistency through a range of contact depths is more than likely caused by material effects, assuming that all equipment calibration has been done correctly. One possible material effect was mentioned in section 4.2.3, where the hardness changed at various contact depths due to the density of geometrically necessary dislocations [83, 84]. The influence of geometrically necessary dislocations is not being disputed, but the variation of hardness as a function of depth could also be caused by other more obvious reasons. Going back to the definition of hardness, which is load divided by the contact area, and taking into consideration that the contact area is dependent on the contact depth, material effects such as pile-up and sink-in will change the final results for reduced modulus and hardness. Pile-up and sink-in will produce an actual contact depth that differs from the instrumentation found contact depth, resulting in the wrong analysis of hardness.

In addition to pile-up and sink-in, there are other material effects to be considered. Many of these, such as mismatches between substrate and film properties [85, 86], will lead to misleading reduced modulus and hardness results that show a strong dependence on the contact depth. To avoid this, most tests are kept to indentation depths less than 20 % of the total film thickness. The only material effect that will be focused on here is pile-up, with the others being left for future research.

4.3.1 Pile-up During Indentation

Pile-up and sink-in are two material-based responses that will create errors in the reported contact area used for calculating the reduced modulus and hardness using nanoindentation. A generalization can be made that pile-up occurs during indentation of soft films and that sink-in occurs during indentation of hard films. The Oliver-Pharr method for determining the contact depth in equation 69 only accounts for small amounts of sink-in. Their method is accurate for a large number of materials, but will lead to inaccuracies when indenting soft or very hard films.

For a soft film, as the indenter is driving further into the film some of the displaced material will pile-up around the sides of the indenter. This results in an underestimation of contact depth and area, and an overestimation of the hardness and reduced modulus. An example of pile-up is shown in Figure 72 and Figure 73. These images were obtained after a 1600 μN indent had been made in a 200 nm thick gold film on a silicon substrate. Figure 72 gives a 3-dimensional view of the gold surface where the residual indentation imprint and surrounding pile-up can be seen. In Figure 73 the topographical heights were measured and a maximum pile-up height of 34.6 nm was found for the 1600 μN indent. These AFM-like images were made using the same equipment used to produce the indent. This is possible because the Hysitron transducer is mounted to piezoelectric material that allows scanning in the surface plane, while the capacitive based transducer measures topographic changes.

124
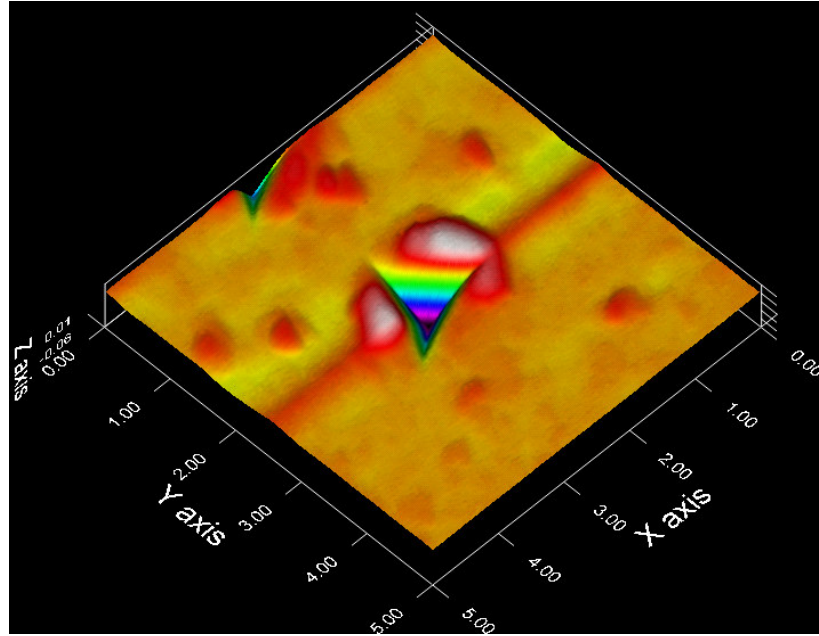
Figure 72. Topographic scan showing pile-up from a 1600 μN indent in gold.
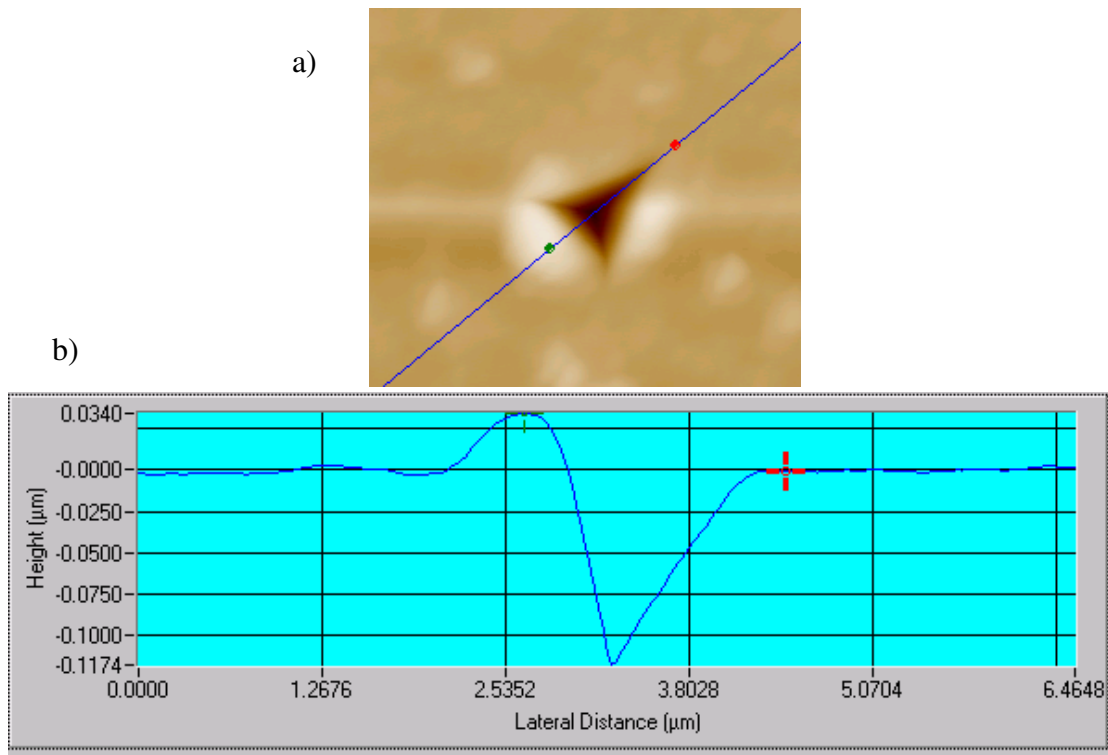
Figure 73. Pile-up measurement from a 1600 μN indent in gold: a) topographic image and b) line profile taken across the indent.

125

Bolshakov and Pharr simulated the effects of pile-up and sink-in on the accuracy of the calculated reduced modulus and hardness using FEM [87, 88]. Their simulations found that as the result of pile-up, the hardness and modulus may be overestimated by as much as 50 %. The ratio of the final displacement to the maximum displacement, h_f/h_{max}, which can be measured experimentally, is a useful indicator of when pile-up may be a significant factor (Figure 74). They found that an h_f/h_{max} ratio of 0.7 is the critical point when pile-up will start to be an influencing factor, especially if the material does not work harden.
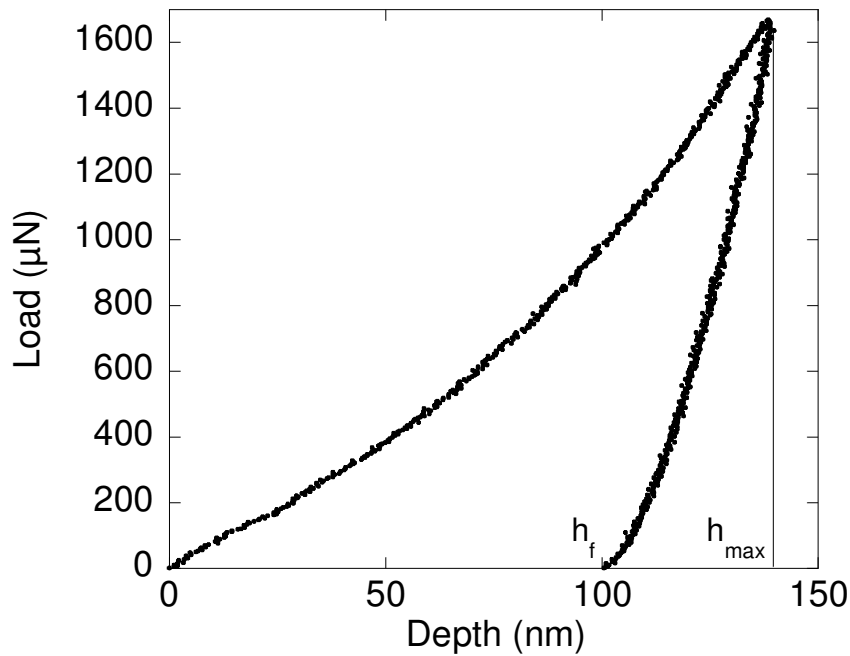
Figure 74. Load-displacement plot of a 1600 μN indent in 200 nm thick gold film.

To apply their findings to the gold results found here, Figure 74 is a plot of the load-displacement curve from a 1600 μN indent. The maximum displacement was measured to be 138 nm and the final displacement upon unloading was 100 nm. This results in an h_f/h_{max} ratio of 0.7246, which is just above the critical point that Bolshakov and Pharr found in their FEM simulations. Unfortunately, one can not predict if a

material work hardens solely on the load-displacement data. With that said, no evidence was found in the literature on whether or not pure gold work hardens. Therefore, it must be assumed that the film does not work harden and the hardness and reduced modulus values of gold will be overestimated.

In Figure 75 the ratio of h_f/h_{max} has been plotted as a function of the maximum indentation load, P_{max}. It can be observed that the experimentally found h_f/h_{max} ratio for the 200 nm thick gold film quickly approaches the Bolshakov and Pharr ratio of 0.7. Therefore, pile-up should be expected to affect the determined values of reduced modulus and hardness for the 200 nm thick gold film.
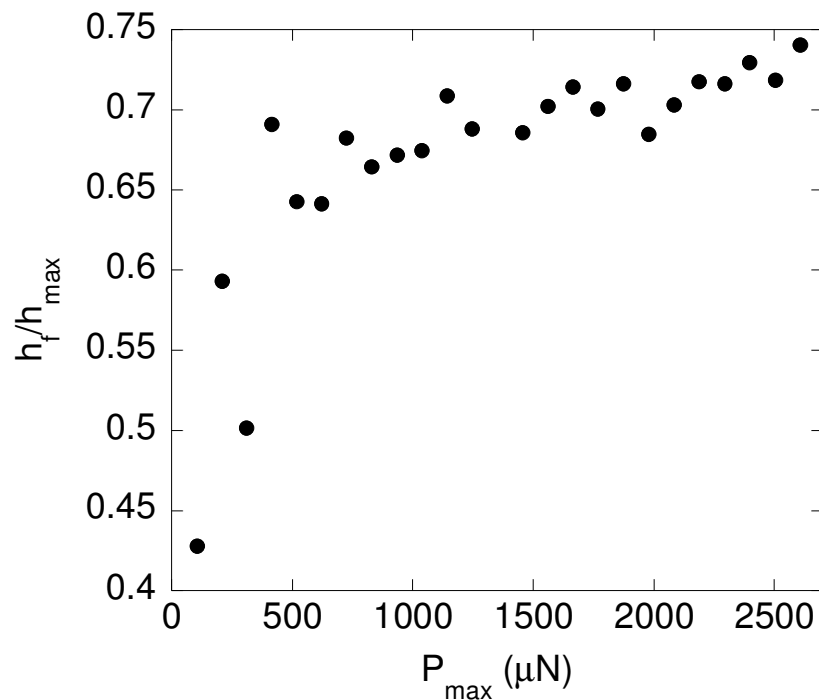
Figure 75. The ratio of h_f to h_{max} versus the maximum indentation load for a 200 nm thick gold film.

In Figure 76 the height of the pile-up has been plotted as a function of the maximum indentation load. The results were obtained by scanning the residual indentation impressions after each indent, similar to the pictures shown in Figure 72 and

127

Figure 73. There appears to be a fairly linear relationship between the amount of vertical pile-up and the maximum indentation load. Since pile-up will affect the contact depth, new values for reduced modulus and hardness were calculated by first determining the actual contact depth. This was accomplished by adding the pile-up height to the contact depth and using the new adjusted contact depth to calculate a new contact area. The new contact area was then used to determine reduced modulus and hardness.
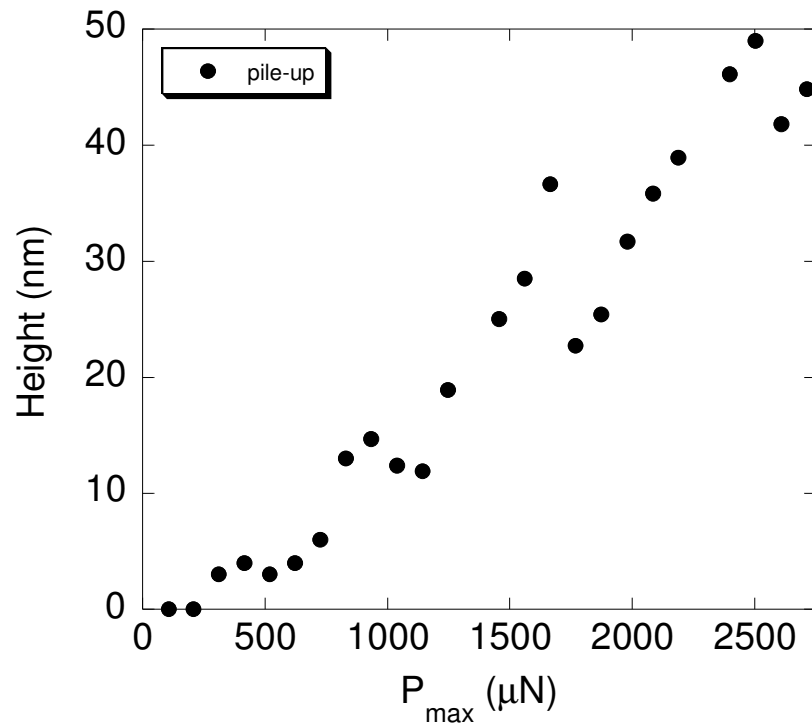
Figure 76. Pile-up as a function of the contact depth for a 200 nm thick gold film.

Figure 77 and Figure 78 compare the hardness and reduced modulus for the 200 nm thick gold film when taking into consideration the additional contact area due to material pile-up. Using the new contact area, the hardness decreased by approximately 1 GPa after maximum indentation loads of 1500 μN. For indents at lower loads, the difference was not as significant. The difference in reduced modulus as the result of using a new contact area was more significant than what was noticed for the hardness.
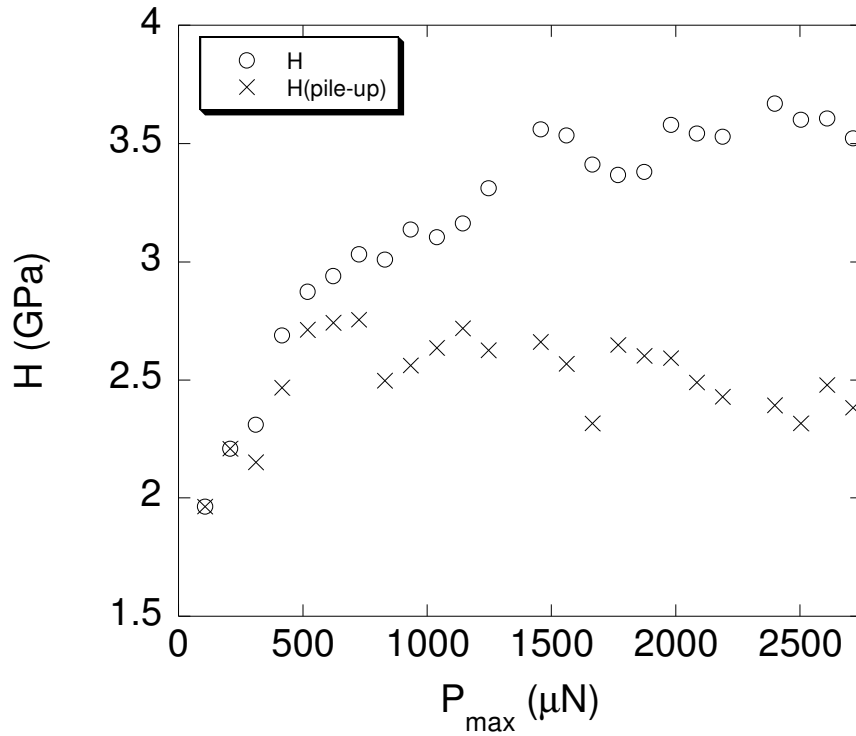
Figure 77. Corrected gold film hardness compensating for pile-up.
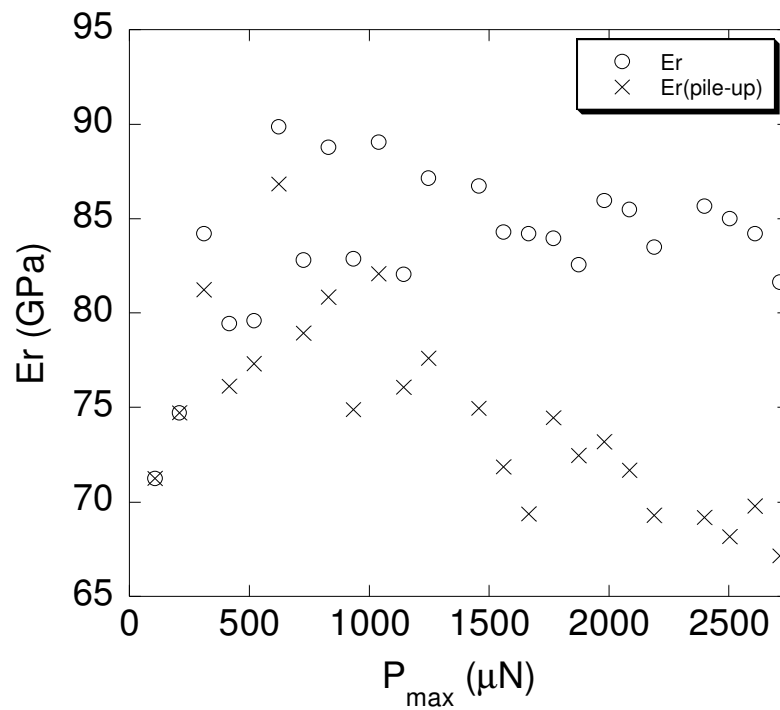
Figure 78. Corrected gold film reduced modulus compensating for pile-up.

129

A good comprehensive study of the determining factors causing pile-up has been conducted by Taljat and Pharr [89]. With the use of finite element analysis, they concluded that pile-up and sink-in are not only dependent on strain hardening, but also on the relative amount of elastic and plastic deformation as characterized by the non-dimensional material parameter, E/σ_y, the non-dimensional depth of penetration, h/R, and the friction coefficient, μ. One effect that they did not mention, which may play a role in the amount of pile-up, is the film thickness. Future tests will be conducted to determine the effect of film thickness on the amount of vertical pile-up. It is expected that indents performed to the same indentation depth, may produce a larger amount of vertical pile-up in thinner films. The thinner films will have in a larger indentation depth to film thickness ratio, h/t, and the substrate may act as a barrier preventing material displacement, resulting in greater amounts of pile-up.

4.4 Dynamic Testing

As device sizes decrease, there will be a need for thinner film thicknesses. As the film thickness is decreased, there is an increasing challenge in obtaining reliable indentation results. Difficulties in defining a tip area function for shallow indents and the influence of substrate properties have been discussed. Up until this point all indentation results have been obtained by using a quasi-static method of indentation, where a load is applied and then fully removed. Another option is to perform dynamic indentation testing, where a dynamic mechanical analysis can be used. For dynamic mechanical analysis (DMA), a small sinusoidal AC force is superimposed on the DC applied load. This is achieved by summing the DC and AC voltages, which is applied to the drive

plates. For a superimposed driving force, $F = F_0 \sin(\omega t)$, the equation of motion of the

indenter relative to the indenter head is modeled as:

$$m\ddot{x} + C\dot{x} + kx = F_0 \sin(\omega t) \tag{76},$$

where m is the indenter mass, C is the damping coefficient, ω is the frequency in rad/sec

and k is the spring constant. The solution to equation 76 is a steady-state displacement

oscillation at the same frequency as the excitation:

$$x = X \sin(\omega \cdot t - \phi) \tag{77},$$

where X is the amplitude of the displacement oscillation and ϕ is the phase shift of the

displacement with respect to the excitation force. The amplitude and phase shift can be

used to calculate the contact stiffness in a dynamic model. The indenter and the sample

are represented by the components in the dynamic model shown in Figure 79. The

standard analytical solution for this model, assuming that the machine frame stiffness is

infinite is as follows, where the amplitude of the displacement signal is:

$$X_0 = \frac{F_0}{\sqrt{\left(k - m\omega^2\right)^2 + \left[(C_i + C_s)\omega\right]^2}} \tag{78},$$

where C_i is the damping coefficient of the air gap in the displacement transducer, C_s is

the damping coefficient of the sample and the combined stiffness $(K_s + K_i)$ is k. The phase

shift between the force and displacement is:

$$\phi = \tan^{-1} \frac{(C_i + C_s)\omega}{k - m \cdot \omega^2} \tag{79}.$$
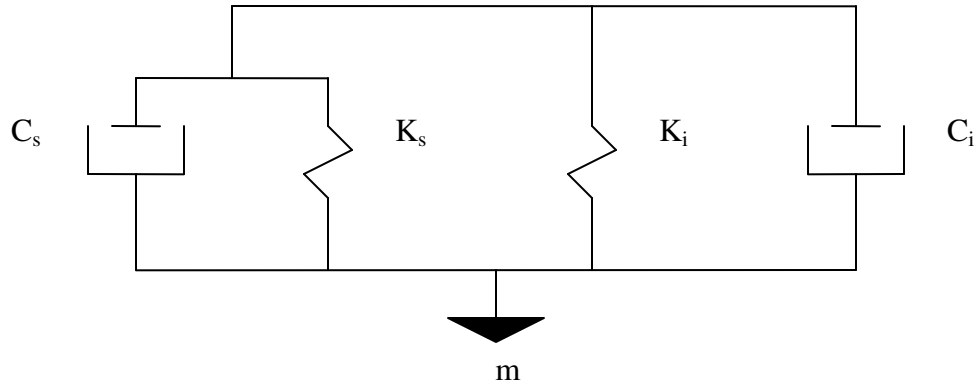
Figure 79. Modeling the dynamic test method.

Similar to the calibrating procedures used for the quasi-static testing, in order to determine the material's reduced modulus, the tip area function, indenter compliance and phase shift as a function of driving frequency must be determined. From there, the specimen stiffness (contact stiffness) is proportional to the reduced modulus:

$$K_s = 2 \cdot E_r \sqrt{\frac{A_c}{\pi}} \qquad (80).$$

The advantage of DMA is that the contact stiffness is obtained continuously during indentation allowing the reduced modulus to be determined throughout the indent cycle. The technique can also be extended to study the viscoelastic properties of polymeric materials. The ultimate sensitivity and useful frequency range of the technique depends on the mass, the damping coefficient and stiffness of the indenter. A low mass, low damping coefficient and optimum stiffness of the indenter will significantly improve sensitivity. There will also be a reduction in plasticity effects, such as reverse plasticity, which is effectively the same as putting a hold time at the peak load during a quasi-static test.

132

The main benefit by of using the dynamic method over the static method was observed here during shallow indent depths of thin films under 200 nm in thickness. Not only was the reduced modulus as a function of contact depth obtained more quickly, but there was less deviation of the results noticed across multiple tests. A comparison of the dynamic and quasi-static indentation tests for determining the reduced modulus is shown in Figure 80 and Figure 81.
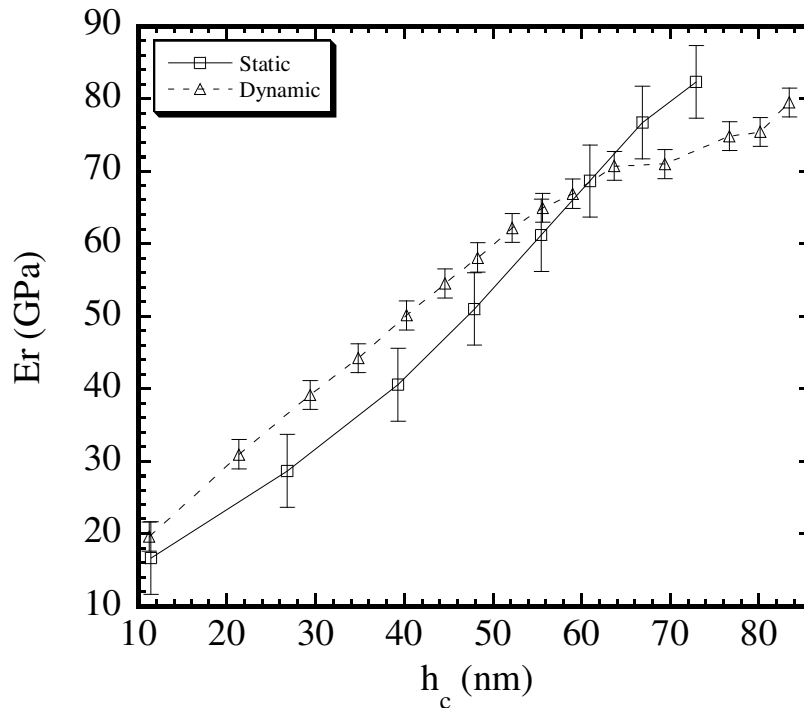
Figure 80. Comparison of dynamic and quasi-static indentation results of Er for a 140 nm thick low-k film.

In Figure 80 the deviation in reduced modulus for a 140 nm thick low-k film using the quasi-static indentation test was found to be ± 5 GPa , compared to ± 2 GPa for the dynamic indentation test. Figure 81 plots the results of quasi-static indentations factoring in pile-up and dynamic tests for determining the reduced modulus of a 200 nm thick gold film. Again, the deviation was less using the dynamic test compared to the quasi-static test.

133
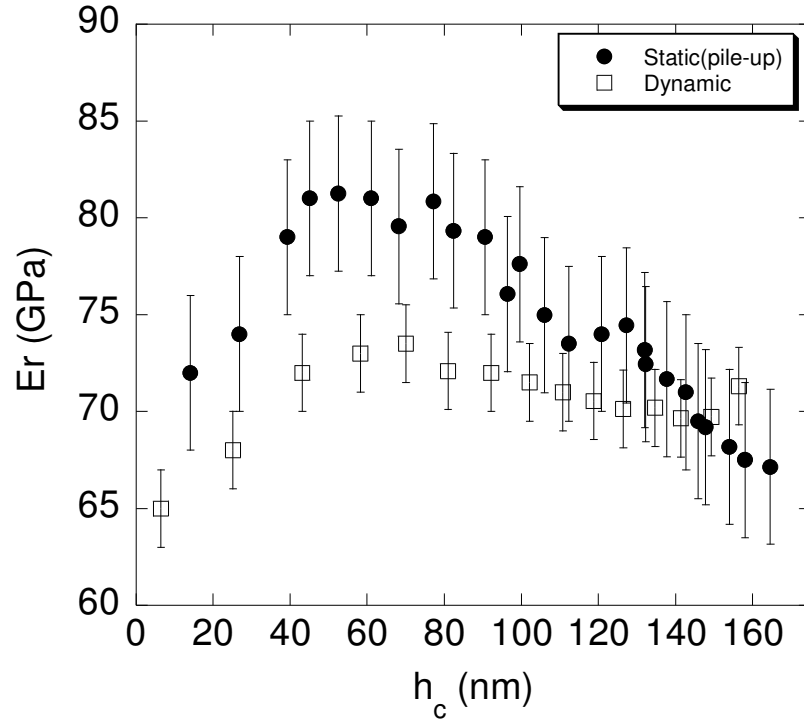
Figure 81. Comparison of dynamic and quasi-static indentation results of Er for a 200 nm thick gold film.

The decision is left up to the user to determine what indentation method they prefer, either quasi-static or dynamic. There have been two advantages observed here for using the dynamic method on thin films. One is that only one indent test needs to be performed to determine the reduced modulus as a function of contact depth. Second, there is less deviation in the results over a collection of tests. Additionally, the dynamic method also gives the user the option of analyzing viscoelastic properties, but this option was not necessary here. The dynamic indentation method is typically not used when analyzing thin film adhesion and fracture toughness. Since the max indentation load and contact depth are the only quantities required from the indentation data, the quasi-static method is preferred for determining those properties.

134

4.5 Non-traditional Tests

The usefulness of indentation for determining the modulus and hardness of thin films has been thoroughly covered in the previous sections. It should also be realized that indentation can be used for determining thin film adhesion and fracture toughness. Knowledge of a thin film's adhesion and fracture toughness is beneficial when reliability issues are of concern. As discussed before, methods will differ between macroscopic and microscopic tests. For example, at the macroscopic level there are two standard specimen configurations for determination of the plane-strain fracture toughness outlined by American Society of Testing and Materials (ASTM) standards; the single edge notched bend (SENB) and the compact tension (CT) specimen [90]. However, due to the film thicknesses that are of interest, the ASTM standard specimens are not an option for determining fracture toughness.

The same size challenges are presented with adhesion testing, although adhesion testing of thin films has a few more options available at the microscale than fracture toughness. A good outline of the different possibilities has been presented by Volinsky et al. [91]. Along with indentation, the four point bend and microscratch tests deserve recognition as popular methods of determining thin film adhesion [92, 93]. There is some debate on which method provides the best quantitative results for adhesion, but the choice of method will more than likely come down to what equipment is available. Because of that, indentation is used quite often because of its popularity for testing thin film modulus and hardness.

Analysis of the indentation load-displacement curve was all that was needed for determining thin film modulus and hardness. For determining thin film adhesion and

135

fracture toughness, analysis of the load-displacement curve will be necessary along with additional information obtained from post-indentation analysis of the film surface. The following sections will describe the procedures needed for determining a thin film's adhesion and fracture toughness using indentation. As before, challenges will be faced when the thin film thickness is decreased to the sub-micron level.

4.5.1 Adhesion Measurements

Adhesion can be described as the mechanical strength or bond strength between two joined bodies. Good adhesion of a film to a substrate is of obvious importance and is believed to be caused by a few different reasons: 1) atomic bonds created by the interaction of the two surfaces, 2) mechanical locking and friction due to surface texture and 3) a transition layer produced by the diffusion of one material into the other [11]. The debate exists on how to quantitatively measure adhesion with numerous approaches spanning from the atomic to macroscopic levels. A more academic approach could be taken, where theoretical bond strengths and perfect materials are considered, or a more pragmatic approach could be used where large area mechanical tests are used. Depending on the approach used, a difference of two orders of magnitude can be observed [11].

From a thermodynamic perspective, the "true" work of adhesion at the interface is the amount of energy required to create free surfaces from the bonded materials. In an ideal case, the true work of adhesion is defined when brittle fracture occurs and there is no energy dissipated due to plastic deformation or friction. Therefore, all energy is conserved as new surfaces are formed:

$$W_A = \gamma_f + \gamma_s - \gamma_{fs} \tag{81}$$

136

where γ_f is the film surface energy, γ_s is the substrate surface energy and γ_{fs} is the interfacial energy. The interfacial energy can be found by knowing the surface energies of the film and the substrate and using the contact angle technique schematically presented in Figure 82:

$$\gamma_{fs} = \gamma_s - \gamma_f \cos\Theta \tag{82},$$

where Θ is the contract angle between the droplet free surface and the substrate. With the surface energies and contact angle known the Young-Dupré equation can be used to find the true work of adhesion:

$$W_A = \gamma_f + \gamma_s - \gamma_{fs} = \gamma_f \left(1 + \cos\Theta\right) \tag{83}.$$
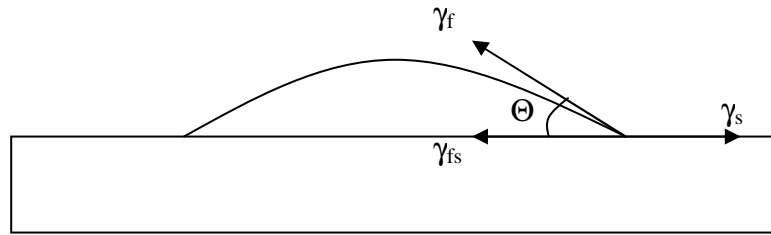
Figure 82. Contact angle technique.

In a perfect situation we could say that the true work of adhesion is equal to the film/substrate adhesion. This follows the idealized case of Griffith fracture where the fracture resistance Γ_i, is assumed to be equal to the thermodynamic true work of adhesion W_A. The true work of adhesion does not account for energy loss due to plastic deformation or friction. Even as fracture occurs in a brittle material there will always be a small plastic zone ahead of the crack tip that may extend from a single bond to over several atomic spacings [94, 95]. The small nonlinear plastic zone immediately surrounding the crack tip will be followed by a linear elastic zone that serves the function

of transmitting the applied stresses to the inner regions. A more sensible value of adhesion is the "practical" work of adhesion:

$$W_{A,P}(W_A) = W_A + U_f + U_s \qquad (84),$$

where W_A is the true work of adhesion, U_f is the energy per unit area spent due to plastic deformation in the film and U_s is the energy per unit area spent due to plastic deformation in the substrate. The practical work of adhesion $W_{A,P}$, is also called the interfacial toughness or the resistance to crack propagation of the film and the substrate pair.

Now that the basic definitions of adhesion are established, fracture mechanics will be considered. This connection is necessary because many of the methods used for determining adhesion are based on fracture mechanics. The field of fracture mechanics emerged from the study of solid mechanics, with a growing desire to characterize fracture and crack growth. In an attempt to provide quantitative answers of the material strength as a function of crack size, two main approaches have been taken; an energy balance approach and a stress intensity approach. The energy balance approach was first developed by A.A. Griffin, who modeled a static crack as a reversible thermodynamic system. He sought a configuration that minimized the total free energy of the system, where the crack would be in a state of equilibrium and thus be on the verge of extension. He started by defining the total energy of the system as being made up of two individual energy terms:

$$U = U_M + U_s \qquad (85),$$

where U_M and U_S are the mechanical and surface energy terms, respectively. The mechanical energy also consists of two parts and is defined as:

$$U_M = U_E + U_A \qquad (86),$$

138

where U_E is the potential strain energy stored in the elastic medium and U_A is the potential energy of the applied loading system. Thermodynamic equilibrium is reached by balancing the mechanical and surface energy terms over a virtual crack extension *da*. Figure 83 is schematic representing Griffith's crack system where *a* is the crack length, *da* is the crack extension, u_0 is the crack opening displacement, *S* is the crack surface and *P* is the applied load. The elastic body in Figure 83 can be treated as an elastic spring in accordance with the Hooke's law:

$$u_0 = \lambda \cdot P \tag{87},$$

where $\lambda = \lambda(a)$ is the elastic compliance. The strain energy of the system is equal to the work of elastic loading:

$$U_E = \int_0^{u_0} P(u_0) du_0 = \frac{1}{2} P \cdot u_0 \tag{88}.$$

The change in elastic energy, dU_E, can be described for two conditions; the fixed grips or the constant load conditions. Under fixed grips condition the applied loading system experiences zero displacement as the crack extends (u_0 = constant) and the elastic strain energy will decrease with crack extension. With fixed grip conditions the energy changes are as follows:

$$dU_A = 0 \tag{89},$$

$$dU_E = -\frac{1}{2}\frac{u_0^2}{\lambda^2} d\lambda = -\frac{1}{2}P^2 d\lambda \tag{90}.$$

The total mechanical energy is therefore:

$$dU_M = -\frac{1}{2}P^2 d\lambda \tag{91}.$$
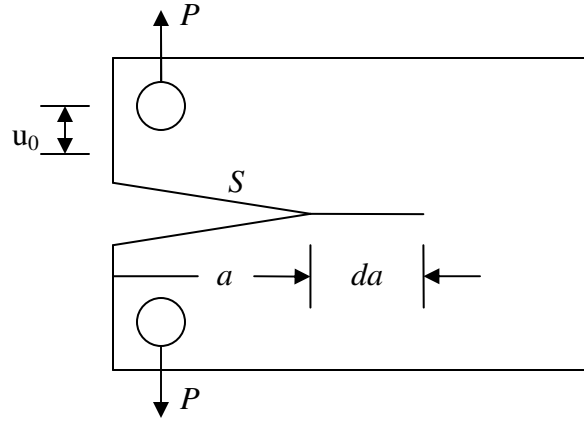
Figure 83. Static crack system for defining the mechanical energy release rate.

For the constant load condition, the potential energy of the applied load decreases and the elastic strain energy increases:

$$dU_A = -Pdu_0 = -P^2 d\lambda \qquad (92),$$

$$dU_E = \frac{1}{2}P^2 d\lambda \qquad (93).$$

Therefore, the total mechanical energy is:

$$dU_M = -\frac{1}{2}P^2 d\lambda \qquad (94).$$

Since equation 91 and equation 94 are identical, it has been shown that the mechanical energy released during incremental crack extension is independent of the loading configuration. The strain energy release rate, G, can be defined as the rate of change of the stored elastic strain energy with respect to the crack area under fixed grips conditions [96]:

$$G = -\left(\frac{\partial U_E}{\partial A}\right)_{u_0} \qquad (95).$$

140

In 1920 Griffith formulated that a crack will continue to grow as long as the strain energy release rate from the surrounding elastically strained material is equal to the energy required to form new surfaces [53]:

$$G = \Gamma_i \tag{96},$$

where Γ_i is the material's resistance to crack growth

The other approach for characterizing fracture and crack growth follows the crack stress field analysis and the next few equations are classic equations for a straight crack of length a:

$$K_I = \sigma_{22}\sqrt{\pi \cdot a} \qquad K_{II} = \sigma_{21}\sqrt{\pi \cdot a} \qquad K_{III} = \sigma_{23}\sqrt{\pi \cdot a} \tag{97},$$

where K is the stress intensity factor for mode I (opening mode), mode II (shear mode), mode III (twisting mode), σ_{ij} are the stresses far from the crack tip and a is the crack length. Modes one, two and three describe how the loads are being applied to the crack. Figure 84 represents the different modes of fracture and if the stress intensity factor K is greater than the critical stress intensity factor K_c, the crack will propagate. The Griffith and stress intensity approaches were combined by Irwin [94]:

$$G = \frac{K_I{}^2(1-v^2) + K_{II}{}^2(1-v^2) + K_{III}{}^2(1+\upsilon)}{E} \tag{98},$$

where E is the Young's Modulus and v is the Poisson's ratio of the bulk material.
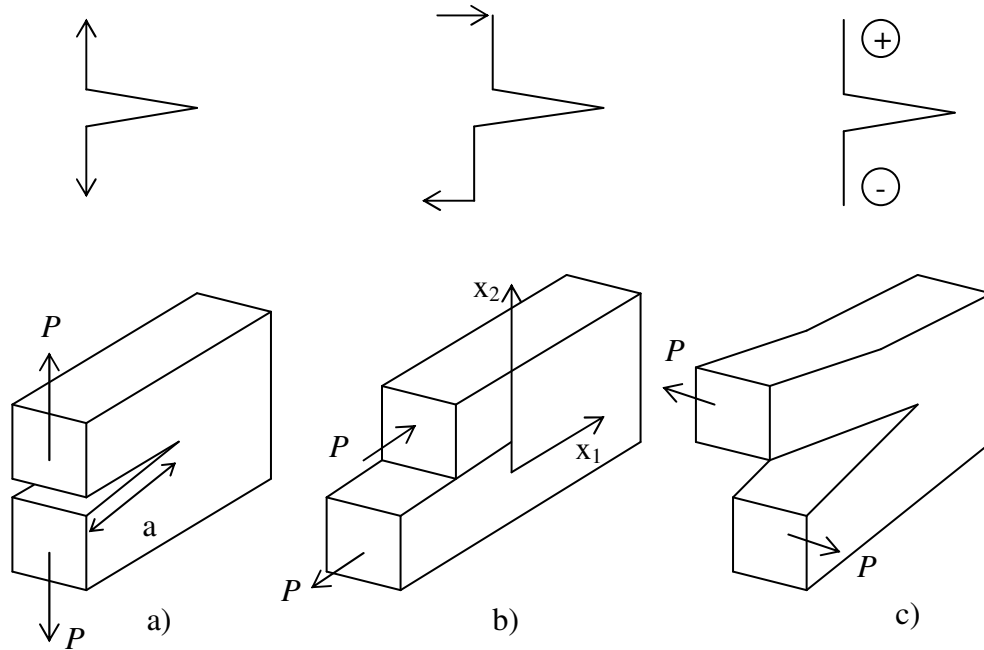
Figure 84. Modes of fracture: a) Mode I b) Mode II c) Mode III.

So far, the fracture analysis assumed the elastic body to be homogeneous and isotropic. Experimental evidence suggests that cracks in brittle, isotropic, homogeneous materials propagate such that pure mode I conditions are maintained at the crack tip. However, when discussing a layered material system, there will be an interface and mismatches in material properties resulting in a combination of modes at the crack tip. A measure of mode II and mode I loading acting on the crack is defined by the phase angle Ψ:

$$\Psi = \tan^{-1}\left(\frac{K_{II}}{K_I}\right) \tag{99}.$$

Application of equation 99 reveals that $\Psi = 0°$ for mode I loading and $\Psi = 90°$ for mode II loading. In general, anytime there is modulus mismatch between two joined bodies a combination of modes will always exist. The Dundurs' parameters, α and β, are used to

142

describe the elastic mismatch between the film and the substrate. The Dundurs'

parameters for plane strain are [97]:

$$\alpha = \frac{(\mu_1 / \mu_2)(1 - \upsilon_1) - (1 - \upsilon_2)}{(\mu_1 / \mu_2)(1 - \upsilon_2) + (1 - \upsilon_1)}$$

$$\beta = \frac{1}{2} \frac{(\mu_1 / \mu_2)(1 - 2\upsilon_2) - (1 - 2\upsilon_1)}{(\mu_1 / \mu_2)(1 - \upsilon_1) + (1 - \upsilon_2)} \tag{100},$$

where μ and υ are shear modulus and Poisson's ratio, and the subscripts 1 and 2 refer to

the upper and lower bimaterial layers. Because of the mode mixity, the interfacial

toughness of the film and the substrate varies with Ψ, as seen in Figure 85.
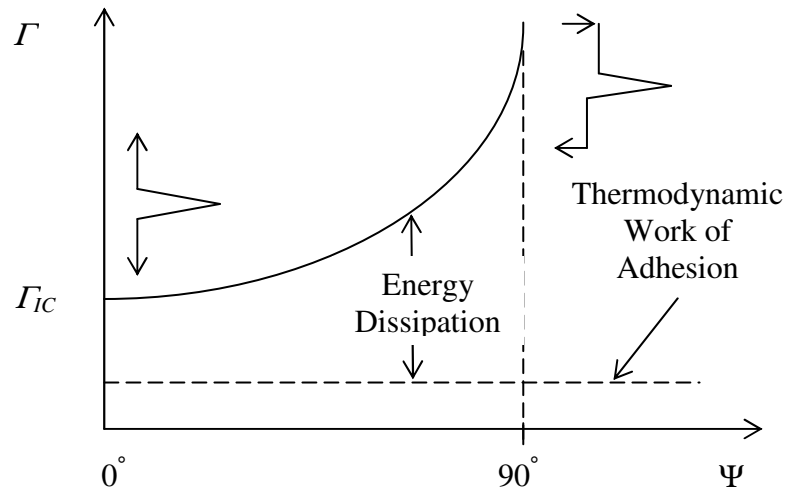
Figure 85. Strain energy release rate as a function of Ψ.

A new criterion for the initiation of crack growth at an interface when the crack

tip is loaded in mixed mode is characterized by Ψ as:

$$G = \Gamma(\Psi) \tag{101},$$

where $\Gamma(\Psi)$ is defined as the toughness of the interface and can be thought of as an

effective surface energy that depends on the mode of loading. A comprehensive study of

143

multiple mixed mode loading configurations has been compiled by Hutchinson and Suo [98].

Marshall and Evans have been able to apply a fracture analysis to indentation-induced delaminations of thin films. They were able to solve for the fracture toughness of the interface in terms of the equilibrium crack length, indenter load and geometry, the film thickness, the mechanical properties and the residual stress. To do this they treated the section of film above the delaminating crack induced by indentation and residual stress as a rigidly clamped disc shown in Figure 86 [99]. In order to help explain their derivation, the solution has been broken down into 4 steps. The first step in Figure 86 a delaminated section is hypothetically taken out to show the effects of a compressive residual stress. If the section was going to be placed back into the sample, the section would have to be recompressed with an edge stress σ_r. The work done would be:

$$U_p = \left(\pi \cdot h \cdot a^2 \right) \sigma_r \varepsilon_r \qquad (102),$$

where $\varepsilon_r = \Delta_R/a$ and $2a$ is the crack length. This is equivalent to the residual strain energy stored within the delaminated section before removal. The total energy of the system, $U_R = U_S + U_p$, is independent of crack length for an unbuckled plate. Therefore, the strain energy in the remainder of the film, $U_S = U_R - U_p$, must depend on the delamination radius, where U_R can now be treated as a constant.
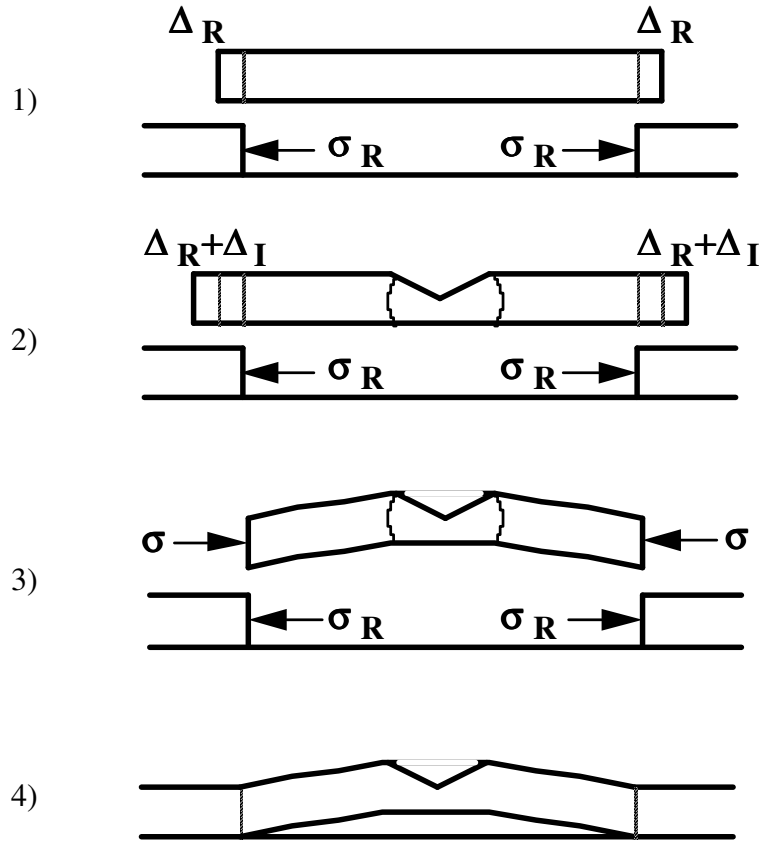
Figure 86. Hypothetical operations used to calculate the strain energy associated with an indentation-induced delamination in a stressed film.

In the second step, the indentation is made, which creates a plastic zone of deformation leaving a permanent impression of volume V_I. It is assumed that volume is conserved and results in radial displacements at the crack tip. It is modeled as an internally pressurized cylinder inducing a radial expansion Δ_I at the edges equal to:

$$\Delta_I = \frac{V_I}{2\pi \cdot h \cdot a} \tag{103},$$

where the indentation strain is defined as $\varepsilon_I = \Delta_I / a$ and the stress required to recompress the section Δ_I is:

$$\sigma_I = \varepsilon_I \frac{E}{(1-v)} = \frac{V_I E}{2 \cdot \pi \cdot h \cdot a^2 (1-v)} \tag{104}.$$

145

The internally pressurized cylinder has a radius-dependent elastic strain energy distribution with a total work done:

$$U_E = -\sigma_I \varepsilon_I \left[\frac{\pi \cdot h \cdot a^2 (1-v)}{2} \right] \qquad (105).$$

In the third step the expanded section is recompressed by a combination of the residual and indentation stresses. Compensating for the possibility of the edge stress exceeding the critical buckling stress the strain energy induced in step 3 is:

$$U_{RI} = \pi \cdot h \cdot a^2 \left[(\sigma_I + \sigma_R)(\varepsilon_I + \varepsilon_R) + (\alpha - 1)(\sigma_I + \sigma_R - \sigma_B)(\varepsilon_I + \varepsilon_R - \varepsilon_B) \right] \qquad (106),$$

where α represents the slope of the buckling load versus the edge displacement upon buckling:

$$\alpha = 1 - \frac{1}{1 + 0.902(1 - v_f)} \qquad (107).$$

In step four there is reinsertion and the total strain energy is the sum of the strain energies just described. The sum of the strain energies can be differentiated with respect to the crack area A in order to find the strain energy release rate G [99]:

$$G = -\frac{d}{dA}(U_S + U_E + U_{RI}) \qquad (108),$$

$$G = \frac{h\sigma_I^2(1 - v_f^2)}{2E_f} + (1-\alpha)\frac{h\sigma_R^2(1 - v_f)}{E_f} - (1-\alpha)\frac{h(\sigma_I - \sigma_B)^2(1 - v_f)}{E_f} \qquad (109).$$

Films that are thin, ductile or strongly adhering are likely to cause problems when using the single layer indentation test. These problems can be avoided by using a superlayer deposited over the film of interest. The superlayer is typically a refractory metal that can be deposited by means of relatively low temperature physical vapor deposition technique such as sputtering, where the temperature is not high enough to alter

146

the microstructure or interface of the original film. The superlayer can be tailored to optimize conditions for film thickness and residual stress, which allows for greater driving force for the same penetration depth to film thickness ratio. One condition that must be met for the superlayer indentation method to work is that the superlayer must adhere to the film more strongly than the film adheres to the substrate. If this condition is not met, the measurement obtained from the adhesion test will be for the superlayer to the film and not the adhesion of the underlying film to the substrate.

Kriese and Gerberich have combined the idea of a superlayer test with the Marshall and Evans findings by applying the laminate theory in order to calculate the strain energy release rate for a multilayer sample [100, 101]. For many cases the superlayer is much thicker than the underlayer and the test can be treated the same as the single layer test defined by Marshall and Evans. The superlayer indentation test has been applied here for determining the interfacial toughness of copper and organo-silicate glass (OSG) films.

Cooper and OSG films are commonly found in IC technology for a variety of reasons. OSG is a low-k dielectric film that is typically used as an insulating layer. The use of low-k dielectrics in the IC industry became popular about the same time as copper's replacement of aluminum for interconnects took place [102]. Both were driven by the desire to decrease RC delays, crosstalk noise and power dissipation. Although the speed of the devices increases as the feature size decrease, the interconnect delays become the major fraction of the total delay and limits the improvement in device performance. The RC delay is dependent on the metals' resistivity, the dielectric constant and the packing density [103]. As the packing density increases there is a

147

reduction in the wiring pitch (sum of the metal line width and the spacing between the metal lines) which results in a larger delay. This delay is a result of an increase in capacitance between the tightly packed metal lines and the increase in resistance due to smaller pitch lines.

Before the introduction of low-k dielectrics, SiO_2 was the popular choice as an interlayer material between interconnect structures. The immediate advantage of using a low-k is the reduction in dielectric constant and for most low-k materials it is below 3. On the down side, structural integrity becomes an issue due to reduced thermal and mechanical properties. Thermal and mechanical stability are important because low-k materials need to withstand the elevated processing temperatures and high stresses that can occur in the interconnect structures [104]. Resistance to thermal decomposition is important because decomposition can severely degrade the dielectric's material properties and lead to outgassing and film delamination. Because of these reasons, adhesion testing of copper and low-k films is of interest.

The first step in determining the adhesion of copper and low-k films was to deposit a tungsten superlayer. For both films a tungsten superlayer was sputter deposited, followed by the use of wafer curvature techniques for determining residual stress. Crack propagation and delamination of the films were then induced by indentation. After delamination the blister radius and contact depth are required to calculate the strain energy release rate. The delamination blister radius is found using an optical microscope with a micron ruler superimposed on the lens in the eye piece. A maximum magnification of 200X was used, as an increase in magnification decreases the ability to see height changes in the film. At 200X magnification, the radii measurements could be

taken with an accuracy of approximately ± 1 µm. The contact depth can be found using the Oliver-Pharr method from the load-displacement curve. A typical delamination blister resulting from the superlayer indentation test is shown in Figure 87. The delamination blister and contact radii are labeled x and a, respectively.
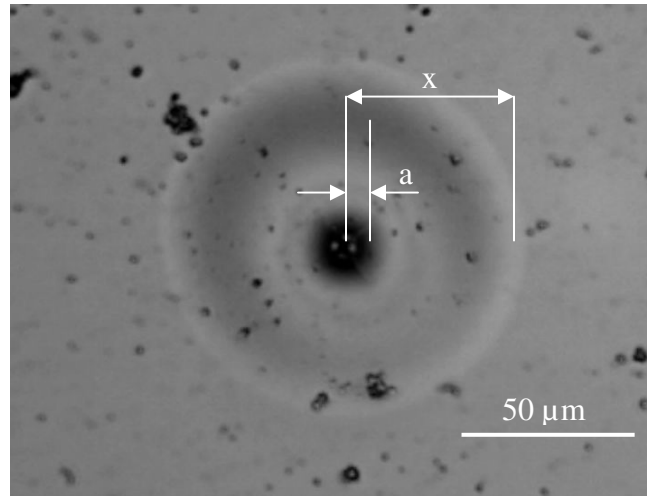
Figure 87. Delamination blister from the superlayer indentation test.

To compensate for the localized effect of the test and determine an average value of film adhesion, 4 trials of indents were made at different locations on each sample. Each trial consisted of 5 to 10 indents at varying loads, with the same load variation being used for each trial. Indentation was performed under load control, with the total indent time remaining the same for all indents on three different samples. To ensure that usable measurements were taken, it was necessary to keep the maximum loads within a certain range. If the loads applied were too small, no delamination blisters appeared. If loads were too high, extensive radial cracks appeared in the thin film along with substrate fracture, making adhesion calculations less accurate.

Figure 88 is the strain energy release rate for a 97 nm thick copper film plotted against x/a. For smaller indents and x/a larger strain energy release rates were

149

consistently measured and as the indents were made to greater depths and larger x/a ratios, the strain energy release rate decreased. Steady state cracking is assumed when the strain energy release rate starts to plateau off at larger x/a ratios, which means that the driving force and interfacial toughness become independent of the delamination length and initial flaw geometry [98].
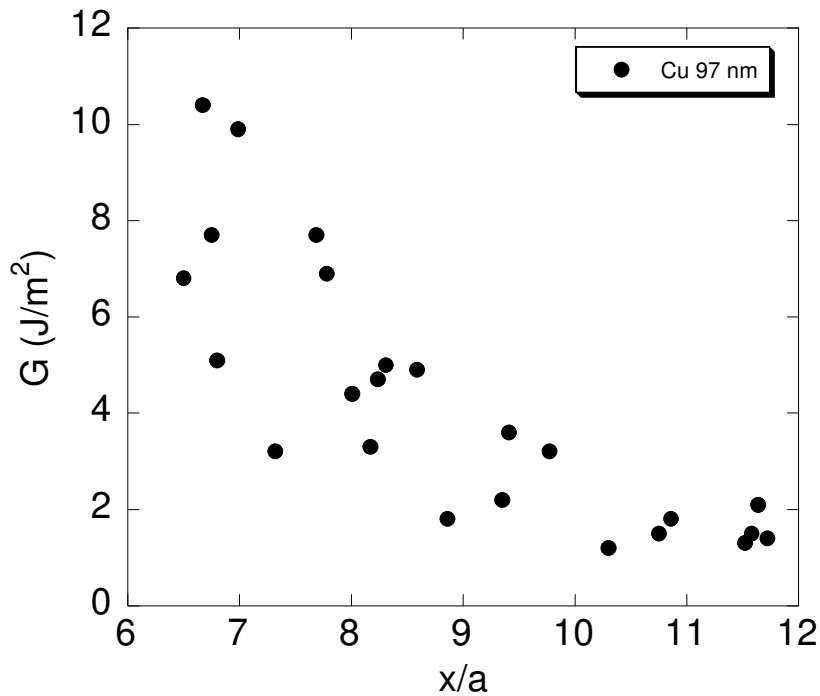
Figure 88. Strain energy release rate for 97 nm thick Cu film.

For the results in Table 6 it was assumed that the steady state strain energy release rate had been reached for x/a ratios greater than 9, and the average of these values were assumed to be the interfacial toughness of the film/substrate. The low-k film was measured to have an interfacial toughness of 0.69 J/m^2, which was comparable to results found in literature [105]. The interfacial toughness of the copper films was measured to be 2.98 and 2.74 J/m^2 for the film thicknesses of 67 and 97 nm, respectively. The increase in interfacial toughness with increasing film thickness was expected and

150

compares to results found in literature [91]. The increase in interfacial toughness with an increasing film thickness is thought to be caused by greater amounts of plastic deformation possible in the thicker films resulting in plastic energy dissipation.

Table 6. Strain energy release rates results for copper and OSG low-k films.

Film	Film thickness (nm)	x/a	W residual stress (MPa)	W thickness (nm)	G (J/m^2)
Cu	67	9-12	320	1100	2.74 ± 0.86
Cu	97	9-12	320	1100	1.98 ± 0.82
OSG low-k	140	9-11	500	463	0.69 ± 0.74

4.5.2 Fracture Toughness Measurements

Fracture toughness is a material property that characterizes a material's resistance to crack propagation. As with the previously discussed mechanical properties, testing procedures used for measuring the fracture toughness of bulk materials and thin films are not the same. The pre-cracked three point bend test is an example of a test method used for measuring bulk materials' fracture toughness, but it will be limited when testing films below several microns in thickness. A comprehensive review of fracture toughness measurement for thin films has been conducted by Zhang et al. and it describes several methodologies for testing thin films [106]. These methodologies were separated into five different categories, which include: bending, buckling, scratching, tensile and indentation tests. All of the methods had their pros and cons, but collectively shared the difficulty in testing thin films with thicknesses below about 100 nm. The indentation test is the most popular method for brittle materials and was reproduced here with its challenges presented and discussed.

151

To make a connection between radial crack patterns observed as a result of indentation and fracture toughness, an understanding of the complex elastic/plastic field introduced during the indentation cycle had to be developed. In order to accomplish this, initial models were based on experiments with soda lime silica glass. Soda lime glass proved to be a convenient sample because of its ability to be well polished and transparent and has been tested by many [107-112]. Much of the initial modeling of the sequential steps observed during crack propagation was based on experiments with soda lime glass. However, more recent findings concluded that no general theory can be used to predict crack morphology. There are five major types of crack morphology that are commonly generated in brittle materials by indentation contact. The expected crack type, and sequence of crack formation will depend on the indenter tip geometry, the mechanical properties of the material and the indentation load [107].

Four of the cracks types are commonly observed when the contact is elastic-plastic using pyramidal shaped indenter tips, including radial, median, half-penny and lateral cracks. There is a fifth type of crack called a cone crack and it is normally generated by the elastic loading of spherical or flat punch indenters. Cone cracks typically spread away from the material surface at a characteristic angle to the load axis after nucleation of a ring crack at the periphery of contact. Radial cracks are generated parallel to the load axis and remain close to the surface, starting at the edge of the plastic contact impression. They are thought to be generated by flaws at the deformation zone boundary and are driven by the residual stress field arising from the strain mismatch of the plastically deformed zone embedded in the surrounding elastically restraining area [108]. Unlike radial cracks, median cracks will be generated beneath the plastic

152

deformation zone and are in the form of full circles or circular segments truncated by the deformation zone boundary or material surface. Although the median cracks are nucleated at the deformation zone boundary, they are thought to be driven by the stress field arising from the elastic loading of the indenter onto the surface [109]. The most commonly seen crack morphology is that of a half-penny and it is depicted in Figure 89. In Figure 89, a half section of an elastic-plastic indent using a pyramidal shaped indenter tip is presented schematically. A portion of the final indent impression can be observed with a residual plastic zone located beneath the indent impression. The half-penny crack morphology is depicted as the dotted regions extending out from the indent impression corners and forming a half-circle shape into the material. Like median cracks, lateral cracks are also generated beneath the deformation zone, running parallel to the surface and are circular in shape.
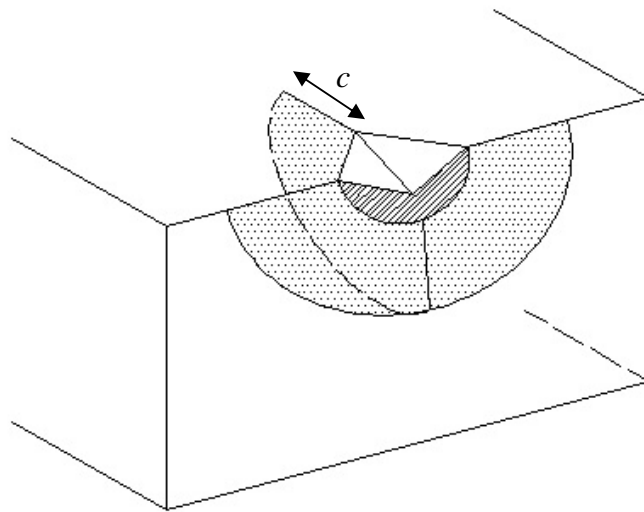
Figure 89. Half-penny fracture morphology.

Lawn, Evans and Marshall were the first to relate a materials' fracture toughness to the maximum applied load, P, and the radial crack length, c [110-112]:

$$K_c = \zeta \left(\frac{E}{H} \right)^{1/2} \frac{P}{c^{3/2}} \qquad (110),$$

where E and H are the Young's modulus and hardness of the material, ς is a material independent constant based on the indenter tip, which for Berkovich and Vickers indenters is $\varsigma = 0.016$ and for a cube corner tip $\varsigma = 0.04$ [113]. Initial indentation tests for calculating fracture toughness were performed on bulk sapphire to gain familiarity with the testing procedure. The modulus and hardness of the sapphire sample was first determined by indentation and the results for the reduced modulus and hardness are presented in Figure 90 and Figure 91.
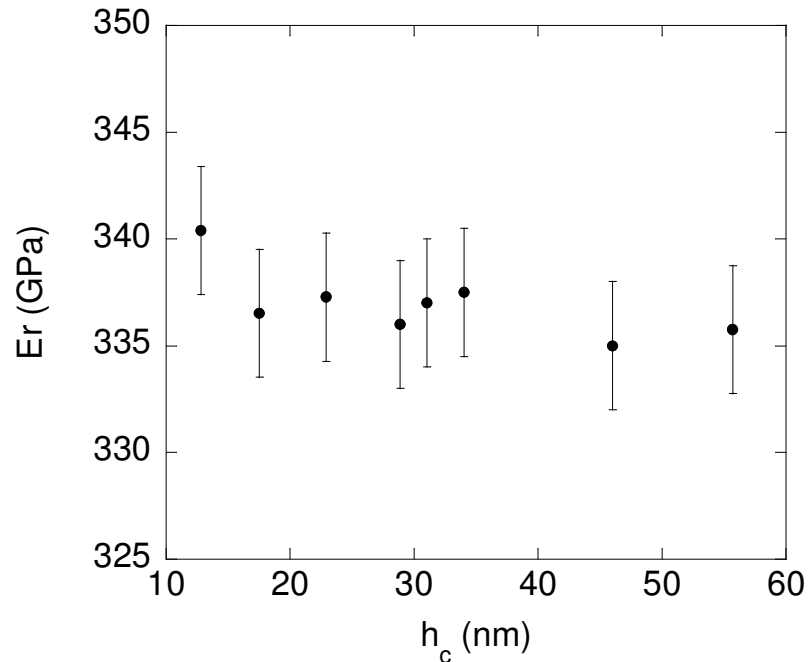
Figure 90. Reduced modulus of sapphire.
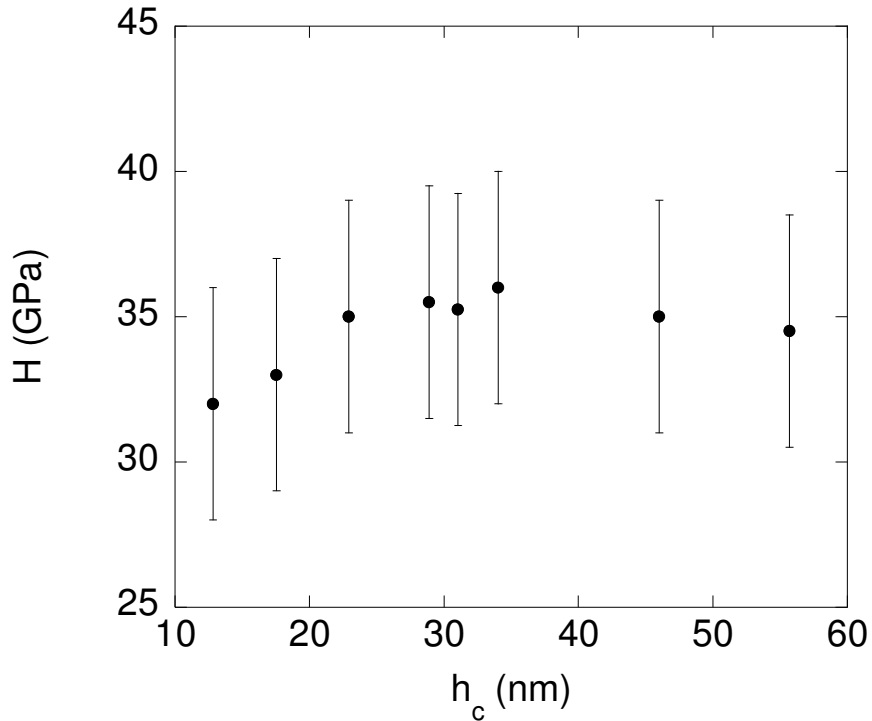
Figure 91. Hardness of sapphire.

After the modulus and hardness were determined, a series of indents ranging from 300 mN to 500 mN were performed using a Berkovich tip and Hysitron's multi-range transducer. The multi-range transducer is meant for indents that require larger loads (1 N) and displacements (80 μm). This load and displacement range is ideal for harder and thicker films. Indents below 300 mN were not used in calculating the fracture toughness of sapphire because they did not produce clearly defined radial cracks that could be observed in the optical microscope. Following indentation, an optical microscope was used to determine the radial crack length, c, and the results of a 500 mN indent can be observed in Figure 92. For each indent, all three of the radial cracks were measured and the average was used for c in equation 107. The average fracture toughness for the sapphire sample was calculated to be 1.2 MPa·m$^{1/2}$, which is lower than what was found in the literature (2.1 MPa·m$^{1/2}$)[111, 114].

155
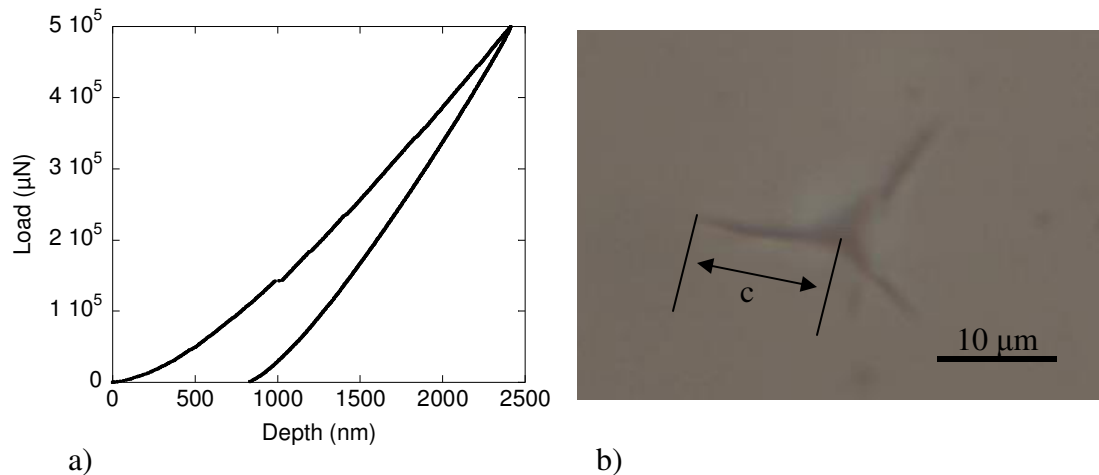
Figure 92. Berkovich indent into sapphire: a) load-displacement curve and b) corresponding optical micrograph.

The tests of sapphire provided confidence in using nanoindentation for calculating fracture toughness, but the goal was to use the method on films with thicknesses around 100 nm. Of particular interest was testing the fracture toughness of a 140 nm thick low-k dielectric film. The first challenge was to determine if radial cracks could be produced at such low loads. A problem arises because indentation cracking will occur at material specific cracking thresholds. The cracking threshold will not only be dependent on the indentation load, but on the geometry and condition of the indenter tip. Harding et al. found that the indentation cracking threshold could be significantly reduced by employing a sharper indenter tip. Their work focused on the geometries of a cube corner and Berkovich tips. When comparing indents to the same contact area, the cube corner tip will displace three times as much volume as a Berkovich tip. This results in greater stresses and strains in the surrounding material leading to a reduction in the cracking threshold load.

156

Initial comparison of the two different tip geometries was done by comparing the load-displacement curves for the same indentation load. It can be observed in Figure 93 that for the same maximum indentation load of a 1000 μN, the maximum indentation depths for the two tips are the same and the final indentation depth is slightly different. This indicates that the Berkovich indenter resulted in more elastic recovery upon unloading. This would be expected due to the larger included angle of the Berkovich indenter producing less stress and strain in the surrounding material.
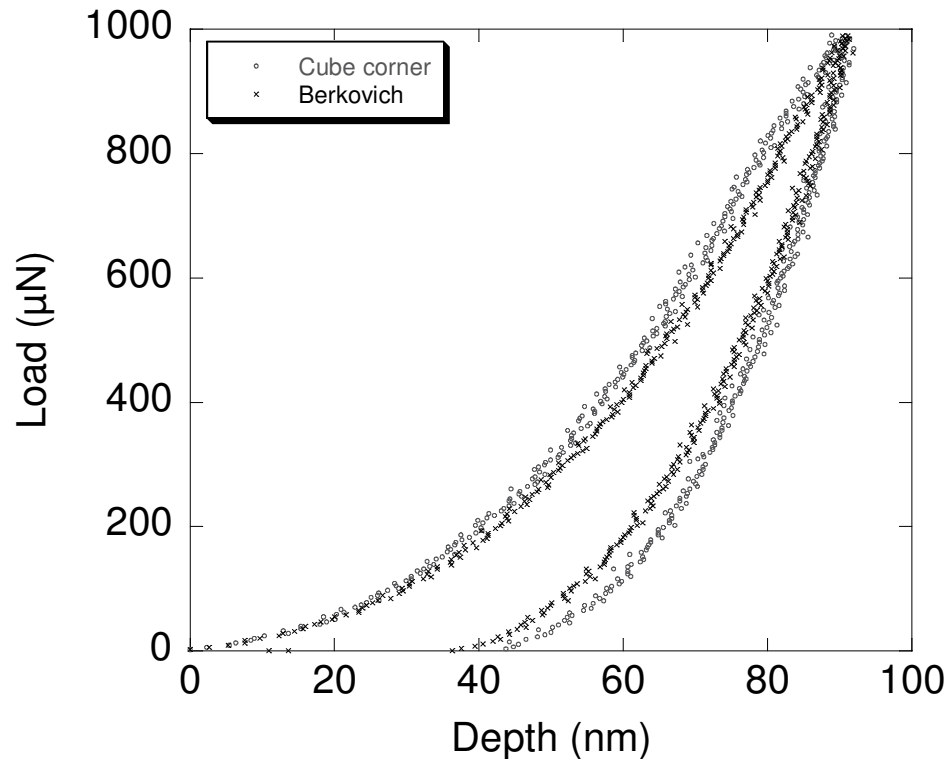
Figure 93. Load-displacement curve for a 1000 μN indent with a Berkovich and cube corner tips.

A more significant difference in the effects of the two tips could be seen after making topographic scans of the residual indents. Figure 94 a) and b) are 5 x 5 μm^2 topographic scans of the residual fractures left by 2000 μN indents using a Berkovich and cube corner indenters. The radial cracks appear to be slightly more defined in the

157

residual indent left by the cube corner tip. The radial cracks were also more consistent in length when comparing all three corners of the indent impression. For the Berkovich tip, there were two radial cracks that always appeared longer than the third one. Using the results obtained for the indentation tests and topography scans, an average fracture toughness of low-k film was calculated to be 0.13 MPa·m$^{1/2}$. The fracture toughness of the low-k film was measured to be higher than what was found in the literature, where fracture toughness of OSG low-k film varied between 0.01 and 0.05 MPa·m$^{1/2}$ [105].

a)   b)
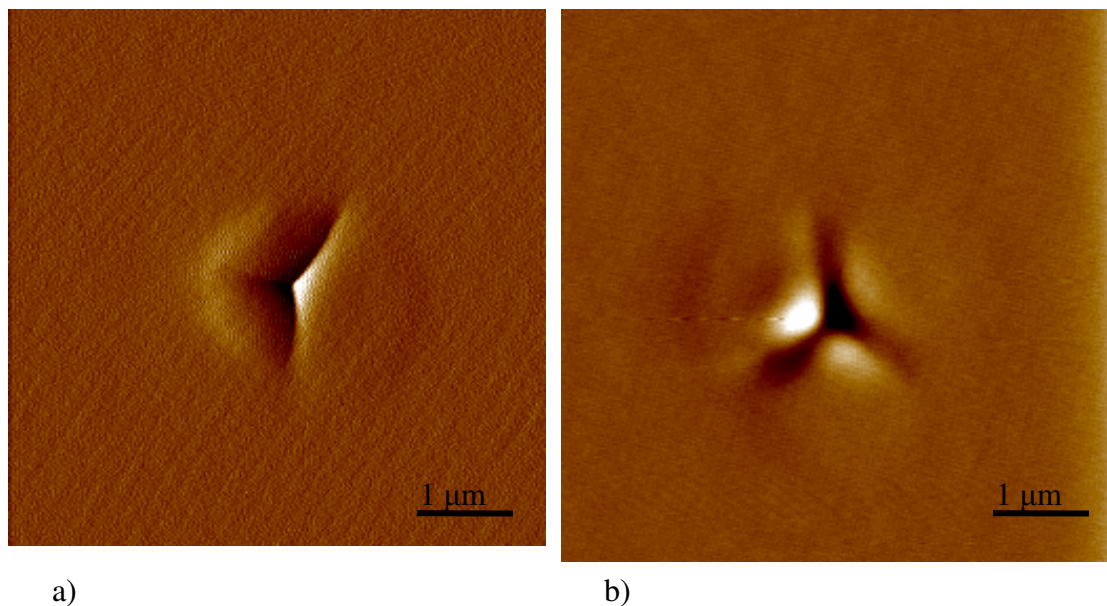
Figure 94. Topographic scan of 2000 μN indent in low-k film using a) Berkovich and b) cube corner tip.

Some improvements could be made to the testing procedure used here and the main one would be obtaining better images of the residual impressions. Using the Hysitron Triboindenter to scan the material surface is limited by the tip sharpness. The tip radii of the Berkovich and cube corner tips were found earlier to be 170 and 90 nm, respectively. The Hysitron transducer has excellent resolution in the vertical direction but will be limited in the lateral directions, especially when trying to measure crack

158

lengths and width. In the future, it would be ideal to use SEM to measure the crack

lengths. The only problem would arise when trying the find the indents on the surface of

the film since they are approximately 1.5 μm in diameter.

There is a major concern about the significance of substrate constraint on the

developing half-penny cracks. Equation 107 is based on the assumption that "well

developed" half-penny cracks are created by indentation, but because of the limited film

thickness of 140 nm, crack development in the low-k layer may be constrained by the

substrate. However, there was still a linear relationship between the maximum

indentation load and the crack length to the 3/2 power, which was observed by Lawn et

al. for well developed cracks (Figure 95) [110]. The ideal crack should also satisfy a

minimum requirement of the radial crack radius, c, to tip imprint radius, a, being at least

2. For the indents here, the ratio was closer to 1.5. Future work will be needed to check

the validity of using equation 107 on ultra thin films such as the ones tested here.
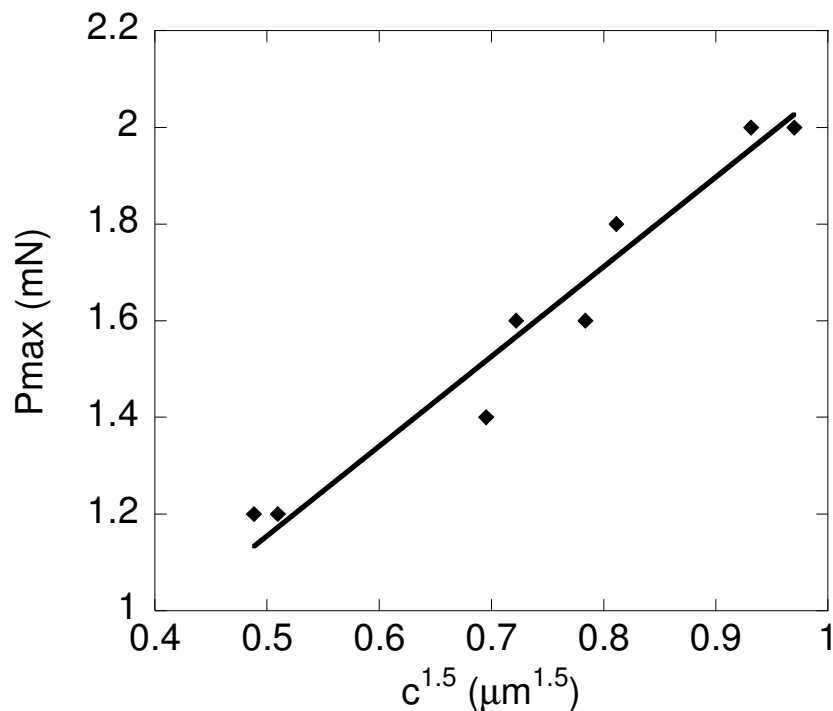
Figure 95. Maximum indentation load as a function of $c^{3/2}$.

Chapter 5

Delaminated Film Buckling Microchannels

5.1 Introduction

So far residual stress in thin films has been primarily shown to result in negative consequences that include wafer bowing, film cracking and delamination. However, depositing a film with compressive residual stress has been demonstrated to be a benefit when using the superlayer indentation for determining thin film interfacial toughness. A similar concept can be employed for creating microchannels. When the strain energy release rate, G, exceeds the interfacial toughness, Γ_i, of a film/substrate, delamination will occur. A simplified form of the strain energy release rate in a stressed film is [98]:

$$G = Z \frac{\sigma_f^2 h}{E_f} \tag{111},$$

where σ_f is the stress in the film, h is the film thickness, E_f is the modulus of elasticity and Z is a dimensionless parameter that depends on the geometry.

In thin film systems with biaxial compressive stress, various shapes of delaminated regions evolve. These shapes include long straight-sided, circular and telephone cord delaminations, which is the most commonly observed morphology. Delamination shape and size will depend on factors such as the film stress, thickness and interfacial toughness. Most importantly, their propagation depends on the interfacial toughness that increases as the mode mixity acting on the interface ahead of the

160

delamination crack shifts from mode I towards mode II. Interfacial failure starts with the film delaminating from the substrate, then the buckling loads the edge of the interfacial crack causing it to spread, resulting in a failure phenomenon that couples buckling and interfacial crack propagation.

To create useful microchannels from film delaminations, the direction and morphology of the delaminations needs to be controlled. The easiest way to control delamination is by controlling the interfacial toughness. This can be done by creating adhesion reducing layers that have a lower interfacial toughness than surrounding areas. A compressively stressed film can be used in conjunction with a patterned adhesion reducing layer as a future method for creating microchannels.

This method of creating microchannels could replace existing methods that tend to be time consuming and cumbersome. A currently used method of creating microchannels is by etching trenches in a substrate such as glass or silicon. The layout of the etched trenches is created using lithography techniques and the process is completed by bonding a glass or silicon wafer to the etched substrate. Drawbacks of using the wafer to wafer bonding technique include misalignment and voids trapped during the bonding processes that can change the desired shapes and future device function. Using delaminations will hopefully solve the existing challenges and provide an alternative method to create microchannels.

5.2 Creating Patterns

To create the adhesion reducing layers, standard photolithography techniques are employed, with the simplest approach using the patterned photoresist as the adhesion reducer. Photolithography is a technique similar to photography, where an original image

161

or pattern is transferred to a photosensitive material. The basic steps in lithography include the following: 1) The application of a photosensitive material (photoresist), 2) soft bake of the photoresist, 3) exposure of the photoresist, 4) development of the exposed pattern and 5) hard bake of the remaining pattern. Figure 96 is a depiction of the basis lithography steps used here along with the additional step of depositing a compressively stress film for creating microchannels using film delaminations.
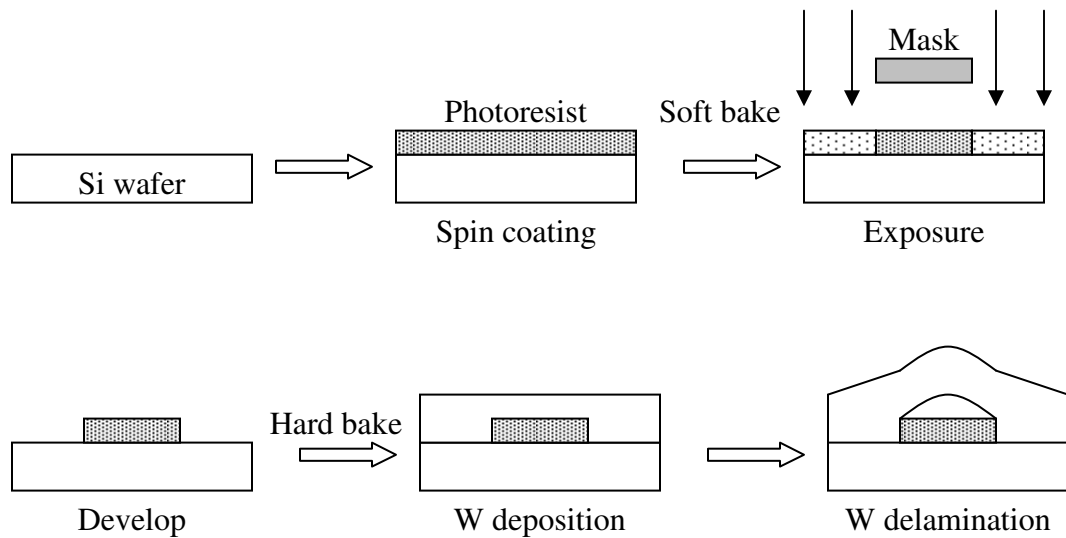
Figure 96. Process of creating microchannels.

There are two types of photoresist to choose from: positive and negative photoresist. Positive photoresist is exposed to UV light wherever it is to be removed. In positive photoresist, exposure to the UV light changes its chemical structure so that it becomes more soluble in a developer, opposite to the negative resist. The exposed resist is then washed away by a developer solution, leaving areas of the bare underlying material. Therefore, the mask contains an exact copy of the pattern which is to remain on the wafer. In general positive resists provide clearer edge definition than negative resists.

The better edge definition by positive resists makes them a better option for high resolution patterns.

Negative photoresists behave in the opposite manner. Exposure to the UV light causes the negative resist to become polymerized, and more difficult to dissolve. Therefore, the negative resist remains on the surface wherever it is exposed, and the developer solution removes only the unexposed portions. Therefore, masks used for negative photoresists contain the inverse of the pattern to be transferred. Shipley 1813 was used here, which is a positive photoresist that is optimized for G-line exposure (436 nm wavelength).

Normally to start the photoresist application process, the wafer surface is prepared in a specific way in order to remove surface moisture and contaminants. In order to remove moisture, the wafers are baked and then primed with an adhesion promoter. Hexamethyldisilazane (HMDS) is normally used as the adhesion promoter and is applied at reduced pressure to form a monomolecular layer on the wafer surface, making the wafer hydrophobic, which prevents moisture condensation. These wafer preparation steps were ignored here since the goal of the photoresist layer was to be an adhesion reducer and only a proof of concept was intended.

Spin coating is used to apply the photoresist with thicknesses ranging from a few hundred nanometers to a few microns. If thicker coatings are required, electrochemical coatings, spray coatings and casting processes are used [115]. A Laurell Technologies WS-400A-8NPP/Lite Spin Processor was utilized here and can handle wafers up to 8" in diameter. It uses a vacuum chuck to hold the wafers in place and the spin speed can range from 0 to 6000 rpm. Acceleration profiles, speed changes and spin times can all be

163

programmed by the user. By adjusting the spin speed the photoresist thickness can be

controlled. The manufacturers supplied thickness versus spin speed for Shipley 1813 is

shown in Figure 97. They suggest that Shipley 1813 has the best coating uniformity

between spin speeds of 3500 and 5500 rpm.
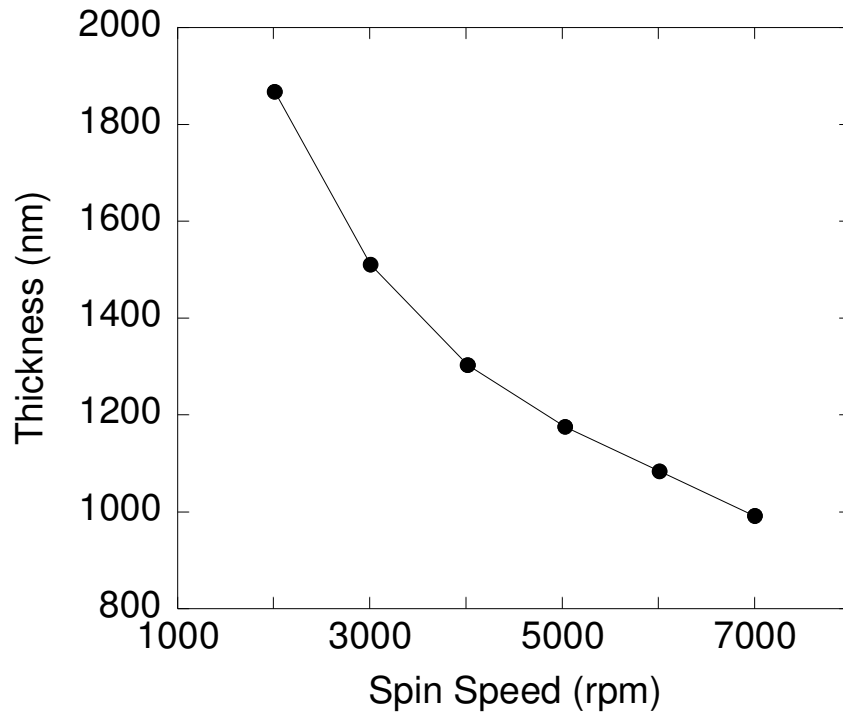
Figure 97. Photoresist thickness as a function of spin speed for Shipley 1813.

The spin speed and time used here were 4000 rpm for 40 sec, with a ramp speed

of 1000 rpm/sec. Based on the manufacture's supplied data for the resist thickness versus

spin speed, it was expected to have a resist thickness of approximately 1.3 μm after

application. However, the resist thickness was measured to be approximately 1.5 μm

with relatively good thickness uniformity across the wafer diameter. Spin-on deposition

of resist was a tricky process because the resist was applied manually. First, the wafer

surface had to be thoroughly cleaned of any debris to avoid streaking of the photoresist

during spinning. After surface cleaning the wafer had to be centered on the vacuum

164

chuck to avoid uneven distribution of the photoresist. A drop of photoresist was then placed in the center of the wafer and a few additional drops were added during the first 5 seconds of ramping the wafer up to full spin speed. Upon completion of the spin-on deposition, the wafer was placed on a hot plate for 90 seconds at 90 °C. It is suggested for future tests that an oven be used instead of the hot plate for soft and hard bake because of the hot plate uneven temperature distribution.

After photoresist soft bake, a range of exposure times was attempted in order to find the optimum for the resist thickness. The light source used for resist exposure was a mercury vapor lamp that provides a wavelength spectrum from 310 to 440 nm. A Karl Suss MA 56 Mask Aligner was used in hard contact mode for the mask and wafer alignment. The mask used had a repeating pattern which consisted of two straight lines running parallel, where the line width was measured to be 250 μm with 30 μm separation. Results of resist profiles after a range of exposure times can be seen in Figure 98 and Figure 99. The resist width and thickness varied up to 10 % across the 4" wafer diameter.
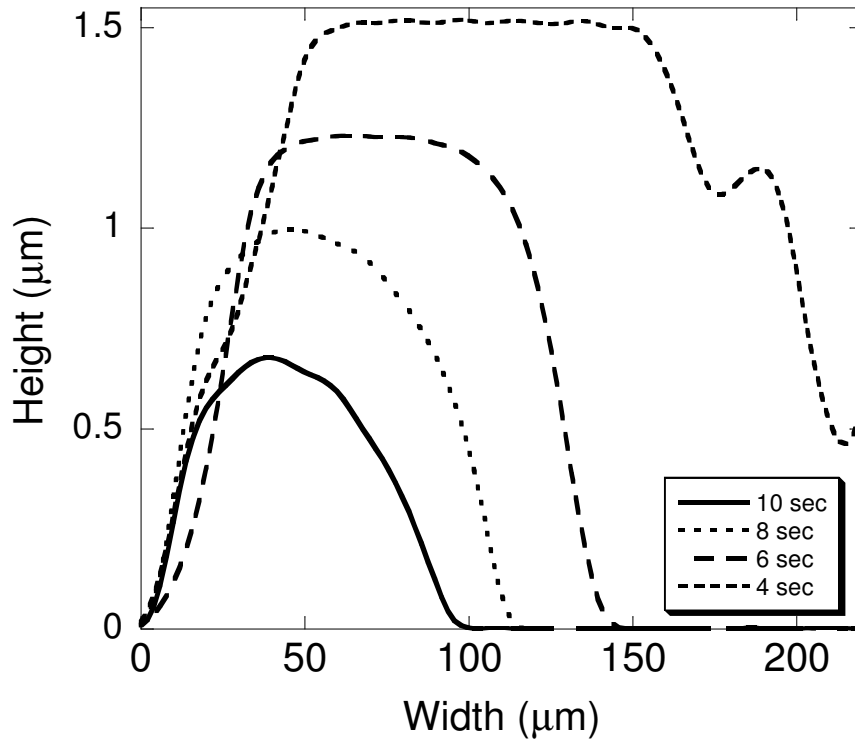
Figure 98. Photoresist profiles after different exposure times.

At the shortest exposure time of 4 seconds, the remaining developed resist
measured 1.5 μm in height and 218 μm in width. However, on most of the wafer there
also remained a thinner layer of resist between the parallel lines. It was concluded that an
exposure time of 4 seconds at 275 W was inadequate. From there the exposure time was
increased in 2 second increments, with the final resist height and width being inversely
proportional to exposure time. Along with decreasing line height and width, the resist
profile ended up being more rounded as the exposure time was increased.

After exposure, the wafers were placed in a developer bath for 30 seconds and
then rinsed with de-ionized water. Nitrogen was used to remove majority of the excess
moisture on the wafer and then it was hard baked on a hot plate at 110 °C for 100
seconds.

166
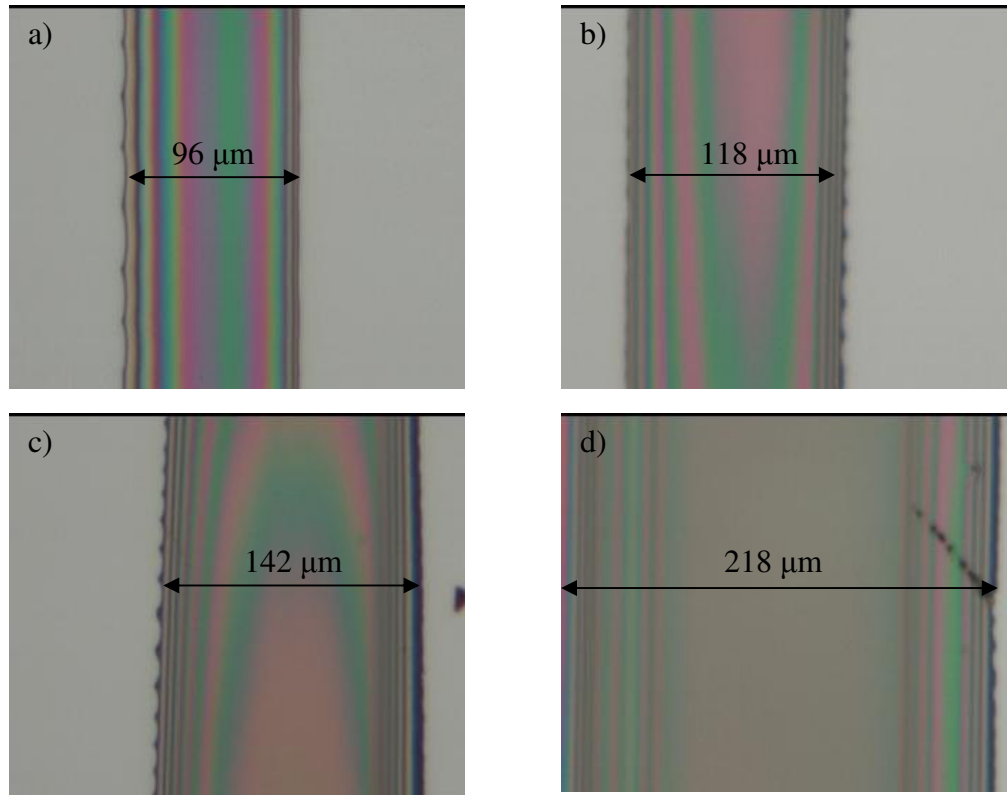
Figure 99. Effect of exposure time on the final photoresist thickness: a) 10 sec, b) 8 sec, c) 6 sec, and d) 4 sec.

Overall the lithography techniques used here were adequate for the objective of creating simple patterns on a wafer. However, it is suggested that a more thorough approach be taken in the future for optimizing spin speed and time, bake time and temperature, exposure and developer time. It must be understood that the line widths created here are relatively large compared with what lithography techniques are capable of. Therefore the quick optimization steps used here were adequate. If smaller line widths and heights were required a more meticulous approach would be needed. The final step in the process was to deposit a tungsten film that is forced to have compressive residual stress. Before those results are presented, a closer look at delamination morphology must be taken.

5.3 Delamination Morphology

As stated before, various shapes of buckled regions evolve in film/substrate systems that are in a state of biaxial compression. Details of their shape and size will depend on factors such as the film stress, thickness and interfacial toughness. The geometry of the buckles can be used to assess interfacial toughness. In straight-sided delaminations, also called Euler mode, the buckling stress can be found using the following expression [98]:

$$\sigma_B = \frac{\pi^2}{12} \frac{E}{\left(1-v^2\right)} \left(\frac{h}{b}\right)^2 \tag{112},$$

where h is the film thickness, b is the delamination half-width, E is the film's modulus and v is the film's Poisson ratio. Figure 100 is a picture of three straight-sided delaminations of a tungsten and diamond like carbon (DLC) film stack on a silicon wafer.
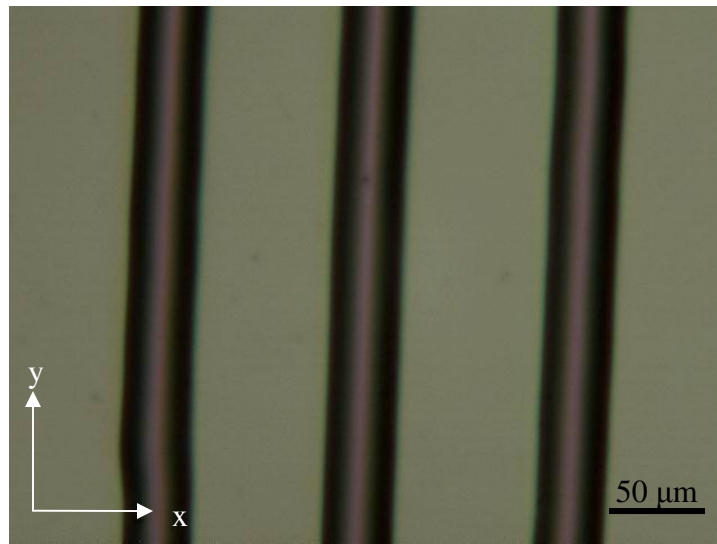
Figure 100. Straight-sided delaminations of a W/DLC film on Si.

168

The compressive stress, σ_r, is responsible for producing the buckling delaminations and can be found using the following expression [98]:

$$\sigma_r = \frac{3}{4}\sigma_B\left(\frac{\delta^2}{h^2}+1\right) \tag{113},$$

where δ is the delamination height. The film's steady state interfacial toughness, Γ_{ss}, is independent of the mode mixity and is defined in the direction of delamination propagation (y-direction) [98]:

$$\Gamma_{SS} = \frac{\left(1-v^2\right)h\cdot\sigma_r^2}{2\cdot E}\left(1-\frac{\sigma_B}{\sigma_r}\right)^2 \tag{114}.$$

The mode-dependent interfacial toughness, $\Gamma(\Psi)$, in the buckling direction (x-direction) perpendicular to delamination propagation is defined as [98]:

$$\Gamma(\Psi) = \frac{\left(1-v^2\right)h}{2\cdot E}(\sigma_r - \sigma_B)(\sigma_r + 3\cdot\sigma_B) \tag{115}.$$

Assuming that fracture happens at the interface, equations 112 through 115 can be applied to solve for the interfacial toughness between the photoresist and the tungsten film when straight-sided delaminations are present. One of the initial deposition tests was on a silicon wafer patterned with the larger 200 μm width photoresist lines. The tungsten film was deposited for 50 minutes with an argon pressure of 5 millitorr. This resulted in straight-sided delaminations forming across the width of the photoresist line as shown in Figure 101 a). The profile of the straight-sided delamination widths is shown in Figure 101 b). Using the delamination height, δ, delamination half width, b, and equations 112-115, the critical buckling stress was calculated to be 194 MPa, the residual stress of the film was 313 MPa, the steady state interfacial toughness was 0.0114 J/m^2 and the mode-dependent interfacial toughness was 0.0859 J/m^2.

169
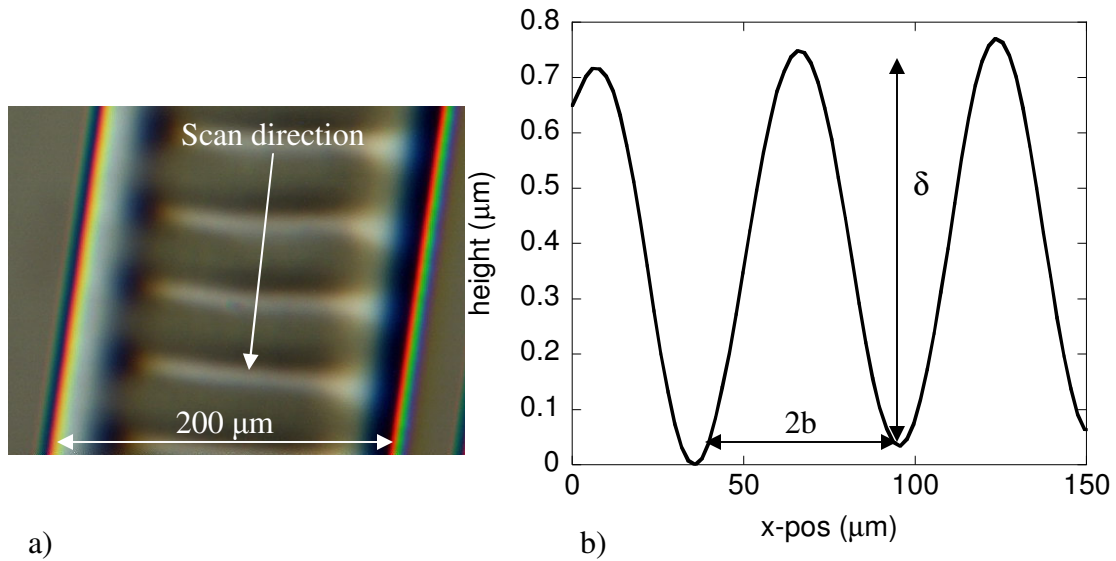
Figure 101. Tungsten delamination a) Optical image of delamination morphology, and b) Profile of delaminations.

The steps just taken for calculating interfacial toughness assumed that fracture took place at the tungsten/photoresist interface, but this has not been confirmed. There is also a possibility that the crack propagates in the photoresist, at the interface between the photoresist and the silicon substrate, or a combination of above mentioned. No matter where the crack is propagating, the important thing is that the interfacial toughness between the tungsten film and the silicon substrate, which has been reported in literature to be 1.73 J/m^2 [101], is stronger than that measured in the photoresist areas. Future experiments need to be conducted to determine the exact origin and path of the crack propagation.

Moon et al. have found that the delamination morphology can be predicted when the film stress is compared to the buckling stress [116]. For $\sigma_r/\sigma_B < 6.5$ straight-sided delaminations are predicted and for $\sigma_r/\sigma_B < 6.5$ telephone cord delaminations are predicted. For the delaminations in Figure 101, $\sigma_r/\sigma_B = 1.6$, which agrees with the Moon

et al. findings. Their predictions of delamination morphology were based on similar experimental methods that utilized lithography techniques for applying patterned areas of low interface adhesion surrounded by areas of high adhesion. By controlling the width of the low adhesion strips, the buckle morphology was controlled.

Ideally the delaminations would propagate parallel to the photoresist lines as opposed to perpendicular to them as seen in Figure 101. The main reason preventing this from happening is that the photoresist line is too wide. The photoresist is so wide that it exceeds the critical buckling width and there is enough room for the straight-sided delaminations to run perpendicular to the lines. Figure 102 a) and b) show two different delamination morphologies that are possible when the photoresist line is decreased in width. Telephone cord delamination morphology can be observed in Figure 102 a) when the photoresist width was approximately 120 μm. When the photoresist width was reduced to approximately 80 μm in Figure 102 b), a straight sided delamination was created. Unfortunately in Figure 102 b) tungsten delamination also occurred in-between the photoresist lines.

a)   b)
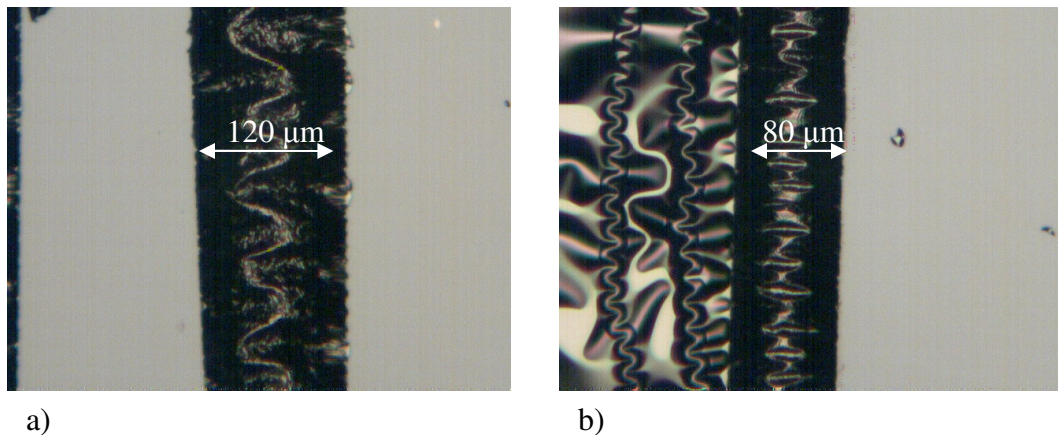
Figure 102. Delamination morphology with different photoresist widths: a) telephone cord delamination and b) straight-sided delamination.

Delamination morphology that was observed in Figure 102 would be necessary if the delaminations were to find future use in transporting fluids. Continued work is necessary to further experiment with photoresist width and its effect on delamination morphology. Attention to deposition parameters for controlling residual stress was found to be more important when using the adhesion reducing layers. Not only was delamination occurring in the patterned areas, but it was also common to see the delamination propagate across other areas of the wafer. The adhesion reducing areas acted as crack initiation sites that helped spawn delamination upon film deposition. There appears to be a fine line between creating delaminations on the patterned areas and delaminations on the rest of the wafer. Controlling the exact amount of compressive residual stress is critical for this method to work and be used for creating microchannels.

5.4 Delamination Microchannel Conclusions

By using photolithography to create adhesion reducing layers, buckling delaminations have been controlled and show potential use as microchannels. Delamination morphology depends on two conditions: 1) the buckling stress which is controlled by the adhesion reducing layers width and 2) the amount of compressive residual stress in the thin film. Here, telephone cord delaminations were observed at larger photoresist widths and straight-sided delaminations were observed for smaller photoresist widths. Line widths between 80 and 220 μm were created here, but future work could included line widths that are a few microns.

172

Chapter 6

Summary and Future Work

6.1 Summary

The research conducted here was separated into 4 main Chapters. Starting with Chapter 2, sputter deposition along with film thickness and residual stress effects were covered. Chapter 3 discussed different methods of measuring residual stress including film thickness non-uniformities in the calculations. Thin film characterization using nanoindentation was discussed in Chapter 4. The last topic was film delamination and its possible use as microchannels, which was covered in Chapter 5. The common thread between the Chapters is that thin film deposition and characterization is important when considering thin film use in microelectronics and MEMS applications.

6.1.1 Sputter Deposition

An in-depth look at DC magnetron sputter deposition has been taken and its effects on residual stress and film thickness uniformity have been examined. Because DC magnetron sputtering is not limited to depositing specific material types, has relatively high deposition rates and low deposition temperatures, it has become a popular method for film deposition. Depending on the system configuration, film thickness and residual stress have been measured to vary significantly across a 4" diameter (100) Si wafer. This variation is caused by the magnet, the same system component that is responsible for high deposition rates and low deposition temperature. The addition of a

magnet allows for a combination of magnetic and electric fields, which gives the system its advantages over basic DC sputtering systems. However, the changing interaction between the magnetic and electric fields across the target surface will result in non-uniform deposition rates and residual stresses.

A profile of the target surface was related to the non-uniform film thickness in the presence of a changing magnetic field. The profile showed a racetrack erosion pattern on the target surface that matched the areas where the magnetic and electric fields are perpendicular, creating an area of high current density. Based on the position of the erosion track, the target to substrate distance and by assuming a cosine sputter yield distribution, a theoretical deposition profile was determined and compared with the experimental data. Theoretical and experimental results show that for the given sputtering system configuration and a 4" wafer, the film thickness will vary from 33 to 45 % between the wafer center and edge. Film thickness uniformity can be improved if modifications are made to the system configuration.

It has been shown that the determining parameter for controlling residual stress is the working gas pressure. In general, low gas pressure will produce compressively stressed films and higher gas pressure will lead to films with tensile residual stress. In extreme cases, a combination of tensile and compressive residual stress has been observed. Reliability issues may exist if thin film residual stress is sufficiently large, where film cracking and delamination may be a mechanism for energy release. High levels of residual stress are unwanted when discussing device reliability, but are desirable when using the superlayer indentation test to determine film/substrate interfacial toughness. The compressively stressed superlayer assists indentation stresses in crack

174

propagation to purposely delaminate a film from a substrate. Following delamination, analysis of the load-displacement curve and delamination blister are conducted to calculate interfacial toughness.

6.1.2 Residual Stress Measurement

In most cases high amounts of residual stress are undesirable and need to be quantified. Two methods have been used here to measure thin film residual stress. One is based on measuring the change in wafer curvature before and after film deposition and the other uses X-ray diffraction to measure the lattice planes spacing. The curvature method was modified to account for changes in film thickness and wafer curvature by profiling the wafer before and after film deposition and reducing the profile into segments. Each segment had its own unique film thickness and curvature and by using the Stoney equation the residual stress for each segment was calculated.

The stress results obtained using the curvature method were compared with stress calculations using the $\sin^2\Psi$ technique. The $\sin^2\Psi$ technique uses X-ray diffraction to measure the lattice planes spacing, which can be related to the film stress if the elastic constants are known. The $\sin^2\Psi$ technique provided comparable results to the curvature method at larger 2θ peaks, but proved unsuccessful at smaller 2θ peaks. The technique could be improved by reducing the X-ray beam spot size and increasing the beam intensity. Unfortunately, that was not an option given the equipment available.

6.1.3 Thin Film Characterization using Nanoindentation

Nanoindentation is widely used for determining thin film mechanical properties, namely hardness and reduced modulus. It was shown here that nanoindentation can also

175

be used for determining film/substrate adhesion and fracture toughness. No matter what test is being performed, proper equipment calibration must be the first priority. The significance of the tip area function and machine compliance were thoroughly discussed, with different calibration methods demonstrated for each. The tip area function is of particular importance because it compensates for deviation between the intended and actual tip geometries. The biggest challenge in manufacturing pyramidal indenter geometry will be at the indenter tip, where it is impossible to manufacture a perfectly sharp tip. The resulting indenter tip geometry is commonly described to be spherical in shape. The spherical shape comparison has been confirmed here for a cube corner and Berkovich indenter by using Hertzian contact theory.

The current challenge for nanoindentation is testing films below 100 nm in thickness. Uncertainties in the tip geometry, surface roughness and substrate effects are all influencing factors at this indentation depth. At shallower indentation depths, dynamic mode testing was found to provide more reliable results with less scatter than quasi-static testing. An additional advantage of dynamic testing is that the reduced modulus can be measured continuously during an indentation, which significantly reduces testing time.

When indenting soft films on hard substrates, pile-up is commonly observed. The Oliver-Pharr method for determining contact depth does not account for pile-up, it assumes a small amount of sink-in. A possible solution to compensate for film pile-up was explored. A topographic scan was performed after each indent in order to measure the amount of pile-up. There vertical amount of pile-up was used to determine a new contact depth. The new contact depth was then used to calculate a new contact area,

176

which is used in the analysis for film hardness and reduced modulus. By compensating for pile-up and using a new contact area, there was a 15 to 30 % difference in reduced modulus and hardness results.

6.1.4 Creating Microchannels from Controlled Film Delaminations

By using standard lithography techniques, areas of low adhesion were created to control delamination morphology. This could be used as a new method for creating microchannels for transporting, mixing and storing fluids in microfluidic devices. Current methods for creating microchannels involve etching and wafer bonding. The advantages of the new method are in its ease of manufacturing and cost effectiveness. Proof of concept was provided here by using photoresist as the adhesion reducing layer. By controlling the photoresist line width, delamination morphology was controlled.

6.2 Future Work

Much of the work presented here addressed current challenges in sputter deposition and film characterization using nanoindentation. Some steps were taken to overcome those challenges, but more work is still required. The following sections outline some ideas that the author would like to address personally or see future graduate students pursue.

6.2.1 Pop-in Phenomenon

Load excursions or pop-ins are interesting events that are sometimes observed in load-displacement curves. Pop-in events are happen during load-controlled indentation and are sudden bursts of displacement at specific indentation loads, which produce discontinuous steps in the load-displacement data. In crystalline materials without

177

surface oxides and other contaminating surface layers, the first pop-in event signifies the transition from purely elastic to elastic/plastic deformation and is thought to be associated with the nucleation and propagation of dislocations [117-119]. The local maximum shear stress generated under the indenter at pop-in events is frequently close to the material's theoretical strength, $G/2\pi$, where G is the shear modulus [120, 120]. This would suggest that deformation at the nano-scale is controlled by the homogeneous nucleation of dislocations and not the motion of pre-existing dislocation structures. Some of the parameters thought to be influencing the pop-in phenomenon are the load applied, loading rates, tip radius, crystal orientation and pre-existing dislocations [119, 120].

Even in a brittle material like sapphire, plastic deformation is initiated prior to the onset of fracture if the indenter tip is sharp. The load at which the pop-in event is observed is found to be very repeatable as in the case of sapphire in Figure 103. The pop-in events in Figure 103 are for three indents and the load at which pop-in occurs varies between 7900 and 8200 μN.
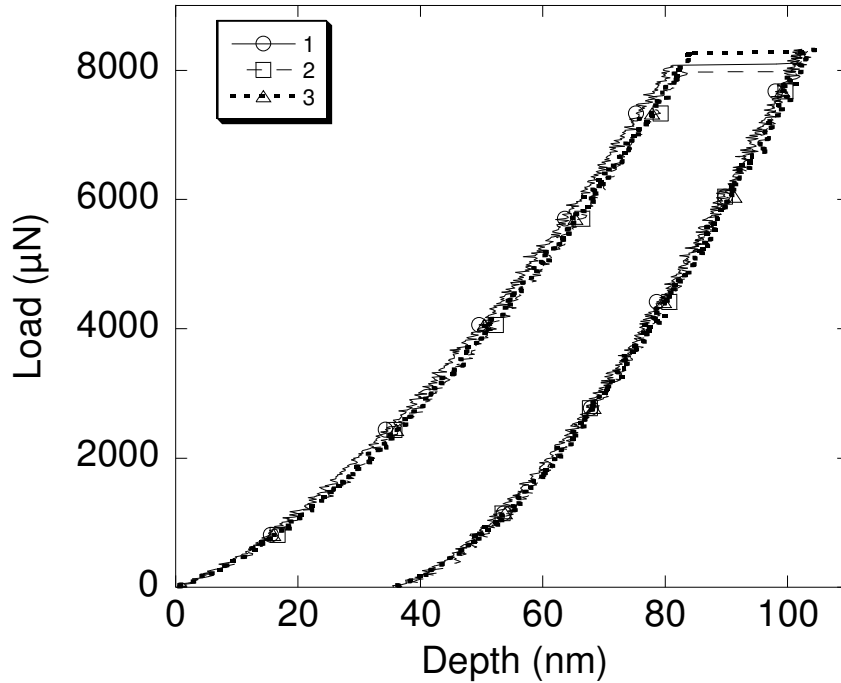
Figure 103. Pop-ins observed at the same load for a sapphire sample using a Berkovich indenter.

To confirm that the pop-in phenomenon was a transition from elastic to elastic/plastic contact, an indent was performed to a maximum load just below the load pop-in events were noticed. Figure 104 is a 7300 μN indent that shows perfectly elastic contact behavior. The loading and unloading portions of the load-displacement curve were plotted with different markers to help indicate this. Since there was no plastic deformation this would indicate that no dislocations were generated. Additional proof of the pop-in being an elastic to plastic transition is by use of Hertzian contact theory applied to the loading portion of the curve prior to the pop-in. Equation 72 from Chapter 4 was used to plot the Hertzian contact model against the loading portion of the load-displacement curve in Figure 105.

179
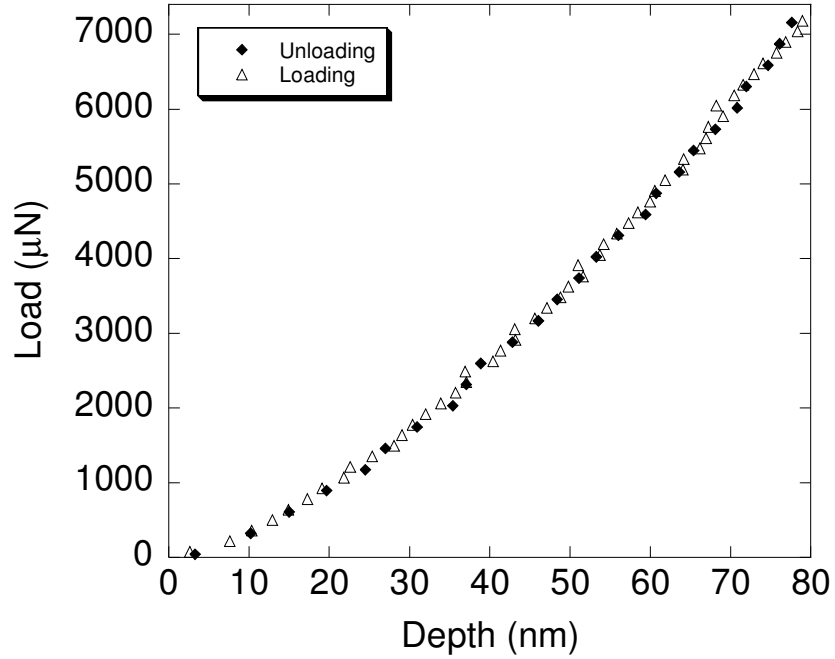
Figure 104. Perfectly elastic indent prior to pop-in loads.
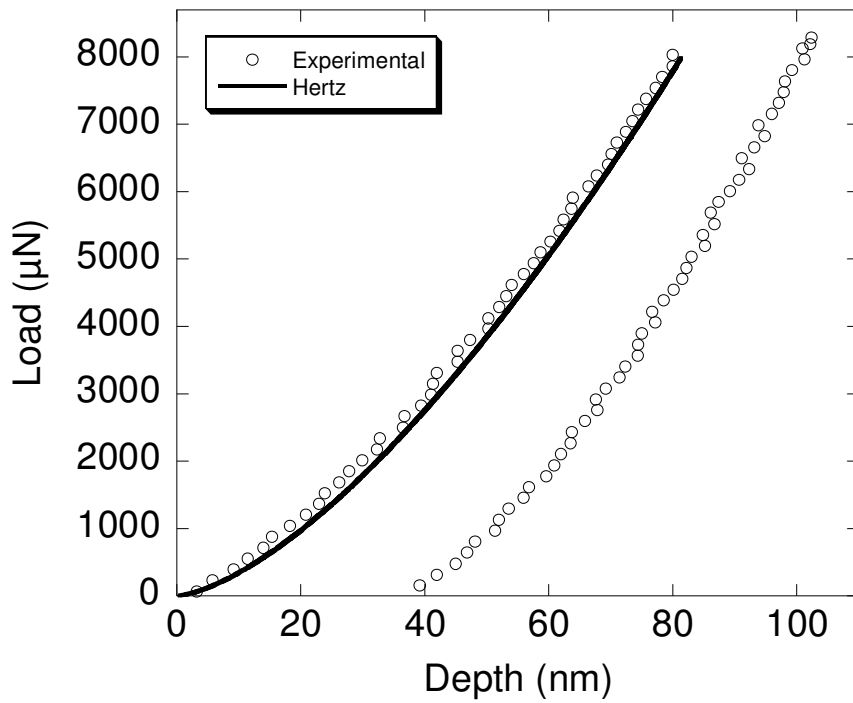
Figure 105. Hertzian fit prior to pop-in event modeling elastic loading.

The resolution of current nanoindenters allows for exploring elastic and plastic

deformation of solids at the nanometer level. Future work would involve using the pop-

in events to calculate the maximum shear stress at the elastic threshold, which could be compared to the theoretical strength of a material.

6.2.2 Microfluidic Devices

Microfluidics has been a rapidly growing field along with the rest of the microelectronics boom. In the late 1980s the early stages of microfluidics were dominated by the development of microflow sensors, micropumps and microvalves [122]. Like many different areas of engineering, having everyone agree on a set definition is sometimes difficult and microfluidics does not differ in that sense. But one point that the majority can agree upon is that a microscopic quantity of a fluid is the key issue in microfluidics. One main advantage of microfluidics is utilizing scaling laws for achieving better sensor performance. This can be seen in the following example regarding diagnostic sensitivity, where the sample volume V and the sensor efficiency η_s are inversely related [122]:

$$\eta_s = \frac{1}{V \cdot N_A \cdot A_i} \tag{116},$$

where N_A is Avogadro's number and A_i is the concentration of analyte i. From equation 116, the sensor efficiency increases with decreasing the sample volume. As the fluid volume is decreased, there will also be a need to decrease the size of the channels the fluid is transported in. Some possible delaminations sizes created here are shown in Figure 106. The delamination channel width was varied from 25 to 60 μm and the height was varied from 0.75 to 2 μm.

181
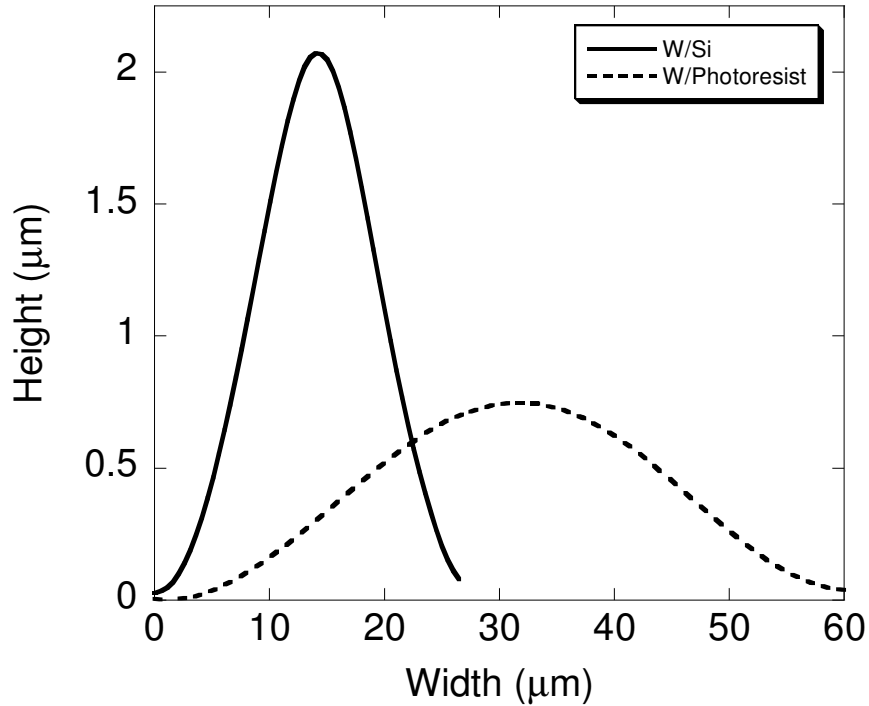
Figure 106. Different delamination channels profiles.

An interesting effect has been observed with the introduction of water at the film/substrate interface of highly compressed films. Water appears to reduce interfacial toughness and spontaneous delamination propagation was initiated with the introduction of water. Figure 107 shows the propagation of a telephone cord delamination over a 90 second time interval when water was introduced at the lower left hand corner. In this case (Figure 107), the delamination microchannels could be used as a one time use, disposable microfluidic devices.
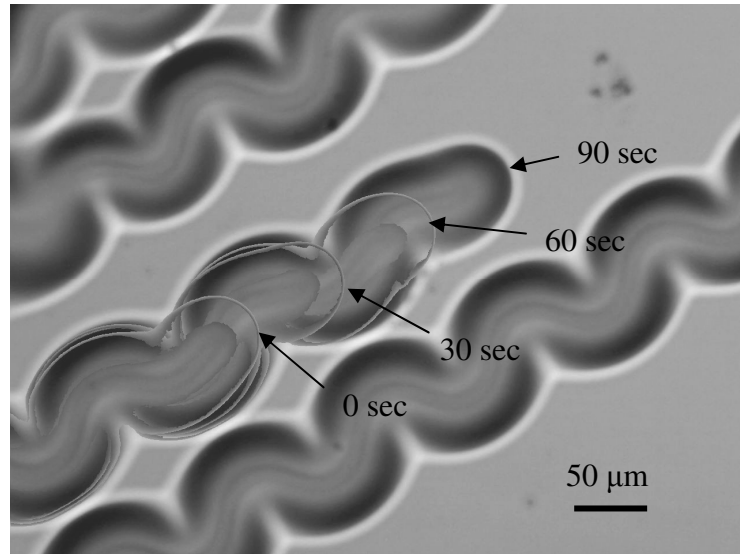
Figure 107. Delamination propagation induced by the introduction of water.

Using film delaminations to create microchannels shows promise in the field of microfluidics. The key to creating the microchannels is by utilizing areas of reduced adhesion to control the delamination morphology. Possible areas for future work could be in finding better choices for adhesion reducing layers and developing more complex delamination patterns. Creating the microchannels is only a small component of the overall picture if they are to be used in microfluidic devices. Integration of the microchannels onto a "lab on a chip" type device is the goal, but many questions still need to be answered on how the fluid will be placed into the microchannels and how the fluid with be transported once inside the microchannels.

References

1   International Roadmap Committee, *International technology roadmap for semiconductors 2007 edition* (2007)

2   M. M Vai,., *VLSI design*, Boca Raton, CRC Press (2001)

3   W. D. Nix, *Mechanical properties of thin films*, Metallurgic Trans. A, 20A, 2217 (1989)

4   B. Jacoby, A. Wienss, R. Ohr. M. von Gradowski, H. Hilgers, *Nanotribological properties of ultra-thin carbon coatings for magnetic storage devices*, Surface and Coatings Technol., 174, 1126 (2003)

5   S. J. Lim, S. Kwon, H. Kim, *ZnO thin films prepared by atomic layer deposition and RF sputtering as an active layer for thin film transistor*, Thin Solid Films, 516, 1523 (2008)

6   X. Liang, G. Zhan, D. King, J. A. McCormick, J. Zhang, S. M. George, A. W. Weimer, *Alumina atomic layer deposition nanocoatings on primary diamond particles using a fluidized bed reactor*, Diamond and Related Materials, 17, 185 (2008)

7   N. Yu, A. Polycarpou, T. F. Conry, *Tip-radius effect in finite element modeling of sub-50 nm shallow nanoindentation*, Thin Solid Films, 450, 295 (2004)

8   K. D. Bouzakis, N. Michailidis, S. Hadjiyiannis, G. Skordaris, G. Erkens, *The effect of specimen roughness and indenter tip geometry on the determnation accuracy of thin hard coatings stress-strain laws by nanoindentation*, Materials Characterization, 49, 149 (2003)

9   R. Gunda, S. K. Biswas, S. Bhowmick, V. Jayaram, *Mechanical properties of rough TiN coating deposited on steel by cathodic arc evaporation technique*, J. Am. Ceram. Soc., 88(7), 1831 (2005)

10   H. Bei, E. P. George, J. L. Hay, G. M. Pharr, *Influence of indenter tip geometry on elastic deformation during nanoindentation*, Physical Review Letters, 95, 045501 (2005)

11   M. Ohring, *Materials science of thin films*, San Diego, Academic Press (2002)

12   B. Kindler, W. Hartmann, J. Klemm, B. Lommel, J. Steiner, *Preparation of targets by sputter deposition*, , Nucl. Instr. And Meth. In Phys. Res. A, 521, 222 (2004)

13   W. R. Grove, *On the electro-chemical polarity of gases*, Phil. Trans. Roy. Soc. London, 142, 87 (1852)

14   A. W. Wright, *On the production of transparent metallic films by electrical dischage in exhausted tubes*, Amer. J. Sci. Arts, 13, 49 (1877)

15   P. Sigmund, Phys. Rev., 184, 383 (1969)

16   M. A. Makeev, A. L. Barabasi, *Effect of surface morphology on the sputtering yields. I. Ion sputtering from self-affine surfaces*, Nucl. Instr. And Meth. In Phys. Res. B, 222, 316 (2004)

17   M. A. Makeev, A. L. Barabasi, *Effect of surface morphology on the dputtering yields. II. Ion sputtering from rippled surfaces*, Nucl. Instr. And Meth. In Phys. Res. B, 222, 335 (2004)

18   C. Huyghebaert, T. Conard, W. Vandervorst, *Energy and angular dependence of the sputter yield and ionization yield of Ge bombarded by O_2^+*, Applied Surface Science, 231, 693 (2004)

19   J. E. Mahon, A. Vantomme, *A simplified collisional model of sputtering in the linear cascade regime*, J. Vac. Sci. Technol. A, 15(4) 1976 (1997)

20   R. V. Stuart, G. K. Wehner, J. Appl. Phys. 33, 2345 (1963)

21   Y. Matsuda, Y. Yamamura, Y. Udeda, K. Uchino, K. Muraoka, M. Maeda, M. Akazaki, Jpn. J. Appl. Phys, *Energy dependence of angular distributions of sputtered particles by ion-beam bombardment at normal incidence*, 25, 8 (1986)

22   S. Mahieu, G. Buyle, D. Depla, S. Heirwegh, P. Ghekiere, R. De Gryse, *Monte Carlo simulation of the transport of atoms in DC magnetron sputtering*, Nucl. Instr. and Meth. in Phys. B, 243, 313 (2006)

23   G. Buyle, D. Depla, K. Eufinger, J. Haemers, W. De Bosscher, R. De Gryse, *Simplified model for the DC planar magnetron discharge*, Vacuum, 74, 353 (2004)

24   T. P. Drusedau, M. Lohmann, F. Klabunde, T. M. John, *Investigations on energy fluxes in magnetron sputter-deposition: Implications for texturing and nanoporosity of metals*, Surface and Coatings Technology, 133, 126 (2000)

25   R. E. Somekh, *The thermalization of energetic atoms during the sputtering process*, J. Vac. Sci. Technol., A2(3), 1285 (1984)

26   J. M. Harper, J. J. Cuomo, R. J. Gambino, H. R. Kaufman, R. S. Robinson, *Mean free path of negative ions in diode sputtering*, J. Vac. Sci. Technol., 15(4), 1597 (1978)

27   R. S. Robinson, *Energetic binary collisions in rare gas plasmas*, J. Vac. Sci. Technol., 16(2) 185 (1979)

28   T. Smy, L. Tan, S. S. Winterton, S. K. Dew, M. J. Brett, *Simulation of sputter deposition at high pressures*, J. Vac. Sci. Technol., A15(6), 2847 (1997)

29   G. M. Turner, S. M. Rossnagel, J. J. Cuomo, *Measured radial and angular distributions of sputtered atoms in a planar magnetron discharge*, J. Appl. Phys. 75(7), 3611 (1994)

30   T. Nakano, S. Baba, *Gas pressure effects on thickness uniformity and circumvented deposition during sputter deposition process*, Vacuum, 80, 647 (2006)

31   S. Hong, E. Kim, B. Bae, K. No, S. Lim, S. Woo, Y. Koh, *A Simulation model for thickness profile of the film deposited using planar circular type magnetron sputtering sources*, J. Vac. Sci. Technol. A, 14(5) 2721 (1996)

32   K. S. Fancey, *A coating thickness uniformity model for physical vapor deposition systems: Overview*, Surface and Coatings Technol., 71, 16 (1995)

33   S. Hong, E. Kim, Z. Jiang, B. Bae, K. No, S. Lim, S. Woo, Y. Koh, *Effects of gas ring position and mesh introduction on film quality and thickness uniformity*, Mat. Sci. Eng., B45, 98 (1997)

34   R. A. Vidal, B. D. Teolis, R. A. Baragiola, *Angular dependence of sputtering yield of water ice by 100 keV proton bombardment*, Surface Science, 588, 1 (2005)

35   S. Inoue, T. Ohba, H. Takata, K. Koterazawa, *Effects of partial pressure on the internal stress and the crystallographic structure of RF reactive sputtered Ti-N films*, Thin Solid Films, 343, 230 (1999)

36   D. W. Hoffman, *Perspective on stresses in magnetron-sputtered thin films*, J. Vac. Sci. Technol. A, 12(4), 953 (1994)

37   D. W. Hoffman, J. A. Thornton, *Internal stresses in sputtered chromium*, Thin Solid Films, 40**,** 355 (1977)

38   J. A. Thornton, J. Tabock, D. W. Hoffman, *Internal stresses in metallic films deposited by cylindrical magnetron sputtering*, Thin Solid Films, 64, 111 (1979)

39   P. V. Plunkett, R. M. Johnson, C. D. Wiseman, *Stresses in sputter-deposited nickel and copper oxide thin films*, Thin Solid Films, 64, 121 (1979)

40   D. W. Hoffman, J. A. Thornton, *Compressive stress and inert gas in Mo films sputtered from cylindrical-post magnetron with Ne, Ar, Kr, and Xe,* J. Vac. Sci. Technol., 17(1), 380 (1980)

41   J. A. Thornton, D. W. Hoffman, *The influence of discharge current on the intrinsic stress in Mo films deposited using cylindrical and planar magnetron sputtering sources*, J. Vac. Sci. Technol. A, 3(3), 576 (1984)

42   H. Windischmann, *Intrinsic stress in sputter-deposited thin films*, Critical Reviews in Solid State and Materials Sciences, 17(6), 547 (1992)

43   D. W. Hoffman, M. R. Gaerttner, *Modification of evaporated chromium by concurrent ion bombardment*, J. Vac. Sci. Technol. 17(1), 425 (1980)

44   J. D. Finegan, R. W. Hoffman, *Stress and stress anisotropy in evaporated iron films*, J. Appl. Phys., 30, 597 (1959)

45   F. A. Doljack, R. W. Hoffman, *The origin of stressing thin nickel films*, Thin Solid Films, 12, 71 (1972)

46   H. Windischmann, *Temperature dependence of intrinsic stress in Fe, Si, and AlN prepared by ion beam sputtering*, J. Vac. Sci. Technol. A, 7(3), 2247 (1989)

47   J. A. Thornton, *The microstructure of sputter-deposited coatings*, J. Vac. Sci. Technol. A, 4(6), 3059 (1986)

48   J. A. Thornton, *Influence of apparatus geometry and deposition conditions on the structure and topography of thick sputtered coatings*, J. Vac. Sci. Technol., 11(4) 666 (1974)

49   J.A. Thornton, Ann. Rev. Mater. Sci. 7, 239, 1977

50   W. Buckel, *Internal stresses*, J. Vac. Sci. Technol. 6, 606 (1969)

51   R. W. Hoffman, *Stresses in shin films: The relevance of grain boundaries and impurities*, Thin Solid Films, 34, 185 (1976)

52   W. D. Nix, B. M. Clemens, *Crystallite coalescence: A mechanism for intrinsic tensile stresses in thin films*, J. Mater. Res., 14(8), 3467 (1999)

53   A. A. Griffith, *The phenomena of rupture and flow in solids*, Phil. Trans. Roy. Soc. London Series A, 221, 163 (1921)

54   A. A. Volinsky, *Fracture patterns in thin films and multilayers*, Mat. Res. Soc. Symp. Proc., 795, U3.8.1 (2004)

55   G. Gore, *On the properties of electro-deposited antimony*, Phil. Trans. Roy. Soc. London, 148, 185 (1858)

56   G. G. Stoney, *The tension of metallic films deposited by electrolysis*, Proc. Roy. Soc. London. Series A, 82, 172 (1909)

57   M. Gelfi, E. Bontempi, R. Roberti, L. E. Depero, *X-ray diffraction debye ring analysis for stress measurement (DRAST): a new method to evaluate residual stress*, Acta Mater., 52, 583 (2004)

58   L. Meda, K. Dahmen, S. Hayek, H. Garmestani, *X-ray diffraction residual stress calculation on textured $La_{2/3}Sr_{1/3}MnO_3$ thin film*, J. Crystal Growth, 263, 185 (2004)

59   C. V. Falub, A. Karimi, M. Ante, W. Kalss, *Interdependence between stress and texture in arc evaporated Ti-Al-N thin films*, Sur. Coat. Technol., 201, 5891 (2006)

60   E. Atar, C. Sarioglu, U. Demirler, E. Kayali, H. Cimenoglu, *Residual stress estimation of ceramic thin films by X-ray diffraction and indentation techniques*, Scripta Mater., 48, 1331 (2003)

61   B. Girault, P. Villian, E. Le Bourhis, P. Goudeau, P. Renault, *X-ray diffraction analysis of the structure and residual stresses of W/Cu multilayers*, Sur. Coat. Technol., 201, 4372 (2006)

62   J. Zhang, Y. Zhang, K. Xu, V. Ji, *General compliance transformation relation and applications for anisotropic cubic metals*, Materials Letters, 62, 1328 (2008)

63   R. W. Hertzberg, *Deformation and Fracture Mechanics of Engineering Materials*, Wiley, New York (1976)

64   G. Maeder, M. Barral, J. L. Lebrun, J. M. Sprauel, *Study of the mechanical behavior of materials by using synchrotron radiation*, The Rigaku Journal, 3(2), 9 (1986)

65   H. Araki, *Micro area X-ray diffraction techniques*, The Rigaku Journal, 6(2), 34 (1989)

66   D. Balzar, N. C. Popa, *Analyzing microstructure by Rietveld refinement*, The Rigaku Journal, 22(1), 16 (2005)

67   B. D. Cullity, S. R. Stock, *Elements of X-ray diffraction*, Prentice Hall, Upper Saddle River, NJ (2001)

68   H. Behnken, V. Hauk, *Determination of steep stress gradients by X-ray diffraction results of a joint investigation*, Mater. Sci. Eng. A, 300, 41 (2000)

69   I. C. Noyan, J. B. Cohen, *Residual stress: Measurement by diffraction and interpretation*, Springer-Verlag, New York (1987)

70   D. R. Askeland, *The science and engineering of materials*, PWS Publishing Co., Boston (1994)

71   B. D. Cullity, S. R. Stock, *Elements of X-ray diffraction*, Prentice Hall, Upper Saddle River, NJ (2001)

72   S. A. Syed Asif, K. J. Wahl, R. J. Colton, *Nanoindentation and contact stiffness measurement using force modulation with a capacitive load-displacement transducer*, Review of Scientific Instruments, May (1999)

73   Hysitron Triboindenter manual

74   W. C. Oliver, G. M. Pharr, *An improved technique for determining hardness and elastic modulus using load and displacement sensing indentation experiments*, J. Mater. Res., 7(6), 1564 (1992)

75   G. M. Pharr, A. Bolshakov, *Understanding nanoindentation unloading curves*, J. Mater. Res., 17(10), 1660 (2002)

76   I. N. Sneddon, *The relation between load and penetration in the axisymmetric Boussinesq problem for a punch of arbitrary profile*, Int. J. Enging. Sci., 3, 47 (1965)

77   J. Y. Kim, D. Read, D. Kwon, *Depth-dependent hardness characterization by nanoindentation using a Berkovich indenter with a rounded tip*, Mat. Res. Soc. Symp. Proc., Vol. 875, O2.4 (2005)

78   K. D. Bouzakis, N. Michailidis, S. Hadjiuiannis, G. Skordaris, G. Erkens, *The effect of specimen roughness and indenter tip geometry on the determination accuracy of thin hard coatings stress-strain laws by nanoindentation*, Materials Characterization, 49, 149 (2003)

189

79   N. Yu, A. A. Polycarpou, T. F. Conry, *Tip-radius effect in finite element modeling of sub-50 nm shallow nanoindentation*, Thin Solid Films, 450, 295 (2004)

80   Y. T. Cheng, C. M. Cheng, *Further analysis of indentation loading curves: Effects of tip rounding on mechanical property measurements*, J. Mater. Res., 13(4), 1059 (1998)

81   J. Thurn, R. F. Cook, *Simplified area function for sharp indenter tips in depth-sensing indentation*, J. Mater. Res., 17(5), 1143 (2002)

82   Z. Xue, Y. Huang, K. C. Hwang, M. Li, *The influence of indenter tip radius on the micro-indentation hardness*, J. Eng. Mat. Technol., 124, 371 (2002)

83   Y. Huang, F. Zhang, K. C. Hwang, W. D. Nix, G. M. Pharr, G. Feng, *A model of size effects in nano-indentation*, J. Mech. Phys. Solids, 54, 1668 (2006)

84   G. Feng, W. D. Nix, *Indentation size effect in MgO*, Scripta Mater., 51, 599 (2004)

85   R. Saha, W. D. Nix, *Effects of the substrate on determination of thin film mechanical properties by nanoindentation*, Acta Mater., 50, 23 (2002)

86   S. M. Han, R. Saha, W. D. Nix, *Determining hardness of thin films in elastically mismatched film-on-substrate systems using nanoindentation*, Acta Mater., 54 1571 (2006)

87   A. Bolshakov, G. M. Pharr, *Influences of pileup on the measurement of mechanical properties by load and depth sensing indentation* techniques, J. Mater. Res., 13, 1049 (1998)

88   G. M. Pharr, *Measurement of mechanical properties by ultra-low load indentation*, Materials Science and Engineering A, 253, 151 (1998)

89   B. Taljat, G. M. Pharr, *Development of pile-up during spherical indentation of elastic-plastic solids*, International J. of Solids and Structures, 41, 3891 (2004)

90   R. J. Sanford, *Principles of fracture mechanics*, Prentice Hall, Upper Saddle River, NJ (2003)

91   A. A. Volinsky, N. R. Moody, W. W. Gerberich, *Interfacial toughness measurements for thin films on substrates*, Acta Mater., 50, 441 (2002)

92   P. G. Charalambides, J. Lund. A. G. Evans, R. M. McMeeking, *A test specimen for determining the fracture resistance of biomaterial interfaces*, J. Appl. Mech., 56, 77 (1989)

93   S. K. Venkataraman, D. L. Kohlstedt, W. W. Gerberich, *Metal-ceramic interfacial fracture resistance using the continuous microscratch technique*, Thin Solid Films, 223, 269 (1993)

94   G. Irwin, *Analysis of stresses and strains near the end of a crack traversing a plate*, J. Appl, Mech. 79, pp. 361-366 (1957)

95   B.R. Lawn, *An atomistic model of kinetic crack growth in brittle solids*, J. Mat. Sci. 10, pp. 469-480

96   B. Lawn, *Fracture of brittle solids*, Cambridge University Press, Great Britain (1993)

97   J. Dundurs, *Edge-bonded dissimilar orthogonal elastic wedges under normal and shear loading*, J. Appl. Mech. 36, pp. 650-652 (1969)

98   J.W. Hutchinson, Z. Suo, *Mixed mode cracking in layered materials*, Adv. Appl. Mech. 29, pp. 63-191 (1992)

99   D. B. Marshall, A. G. Evans, *Measurement of adherence of residually stressed thin films by indentation. I. Mechanics of interface delamination*, J. Appl. Phys., 56(10), 2632 (1984)

100   M. D. Kriese, W. W. Gerberich, N. R. Moddy, *Quantitative adhesion measures of multilayer films: Part I. Indentation mechanics*, J. Mater. Res., 14(7), 3007 (1999)

101   M. D. Kriese, W. W. Gerberich, N. R. Moddy, *Quantitative adhesion measures of multilayer films: Part II. Indentation of W/Cu, W/W, Cr/W*, J. Mater. Res., 14(7), 3019 (1999)

102   P.S. Ho, J. Leu, W.W. Lee, *Low Dielectric Constant Materials for IC Applications*, Springer, Verlag Berlin Heidelberg (2003)

103   T. Sakurai, T. Iizuka, *Gate electrode RC delay effects in* VLSI's, IEEE J. of Solid State Circuits, 20(1), 290 (1985)

104   W.D. van Driel, *Facing the challenge of designing for Cu/low-k* reliability, Microelectronics Reliability, article in press (2007)

105   A. A. Volinsky, J. B. Vella, W. W. Gerberich, *Fracture toughness, adhesion and mechanical properties of low-k dielectric thin films measured by nanoindentation*, Thin Solid Films, 429, 201 (2003)

106   S. Zhang, D. Sun, Y. Fu, H. Du., *Toughness measurement of thin films: a critical review*, Surface Coatings Technology, 198, 74 (2004)

191

107   R. F. Cook, G. M. Pharr, *Direct observation and analysis of indentation cracking in glasses and ceramics*, J. Am. Ceram. Soc., 73(4), 787 (1990)

108   B. R. Lawn, T. P. Dabbs, C. J. Fairbanks, *Kinetics of shear-activated indentation crack initiation in soda-lime glass*, J. Mater. Sci., 18, 2785 (1983)

109   B. R. Lawn, M. V. Swain, *Microfracture beneath point indentations in brittle solids*, J. Mater. Sci., 10, 113 (1975)

110   B.R. Lawn, A.G. Evans, D.B. Marshall, *Elastic/plastic indentation damage in ceramics: The median/radial crack* system, J. Am. Ceram. Soc. 63 [9] 574-581 (1980)

111   G.R. Anstis, P. Chantikul, B.R. Lawn, D.B. Marshall, *A critical evaluation of indentation techniques for measuring fracture toughness: I, direct crack* measurements, J. Am. Ceram. Soc., 64 [9] 533-538 (1981)

112   P. Chantikul, G.R. Anstis, B.R. Lawn, D.B. Marshall, *A critical evaluation of indentation techniques for measuring fracture toughness: II, strength method*, J. Am. Ceram. Soc., 64 [9] 539-543 (1981)

113   D.S. Harding, W.C. Oliver, G.M. Pharr, Mater. Res. Soc. Symp. Proc. 356 (1995)

114   T. Scholz, G. A. Schneider, *Fracture toughness from submicron derived indentation cracks*, Appl. Phy. Let., 84(16), 3055 (2004)

115   S. Franssila, *Introduction to micro fabrication*, John Wiley and Sons, Ltd, West Sussex, England (2004)

116   M. W. Moon, K. R. Lee, K. H. Oh, J. W. Hutchinson, *Buckle delamination on patterned substrates*, Acta Mater., 52, 3151 (2004)

117   W. W. Gerberich, J. C. Nelson, E. T. Lilleodden, P. Anderson, J. T. Wyrobek, *Indentation induced dislocation nucleation: The initial yield point*, Acta Mater., 44(9), 3585 (1998)

118   Y. L. Chiu, A. H. W. Ngan, *Time-dependent characteristics of incipient plasticity in nanoindentation of a Ni_3Al single crystal*, Acta Mater., 50, 1599 (2002)

119   W. Wang, C. B. Jiang, K. Lu, *Deformation behavior of Ni_3Al single crystals during nanoindentation*, Acta Mater., 51, 6169 (2003)

120   H. Bei, E. P. George, J. L. Hay, G. M. Pharr, *Influence of indenter tip geometry on elastic deformation during nanoindentation*, Phy. Rev. Letters., 95, 045501 (2005)

121   T. A. Michalske, J. E. Houston, *Dislocation nucleation at nano-scale mechanical contacts*, Acta Mater., 46(2), 391 (1998)

122   N.T. Nguyen, S.T. Werely, *Fundamentals and Applications of Microfluidics*, Artech House, Norwood, MA (2002)

Appendices

Appendix A. Excel Spreadsheet for Theoretical Film Thickness

The excel spreadsheet below is only a small fraction of the total spreadsheet used for predicting the film thickness distribution across a four inch wafer. The target erosion profile was used to determine the how the sputtering yield varies across the target. By assuming a cosine distribution for the sputtering yield and using a target to substrate distance of 5 cm the film thickness was predicted.

					offset		
					SY		
d =	5						

deg	rad	tan	cos	x-pos		Sy_0	
-90	-1.570796	-1.63246E+16	6.12574E-17	-8.16228E+16	6.12574E-17	-8
-89	-1.553343	-57.28996163	0.017452406	-286.4498082	0.017452406	-2
-88	-1.53589	-28.63625328	0.034899497	-143.1812664	0.034899497	-1
-87	-1.518436	-19.08113669	0.052335956	-95.40568344	0.052335956	-9
-86	-1.500983	-14.30066626	0.069756474	-71.50333128	0.069756474	-7
-85	-1.48353	-11.4300523	0.087155743	-57.15026151	0.087155743	-5
-84	-1.466077	-9.514364454	0.104528463	-47.57182227	0.104528463	-4

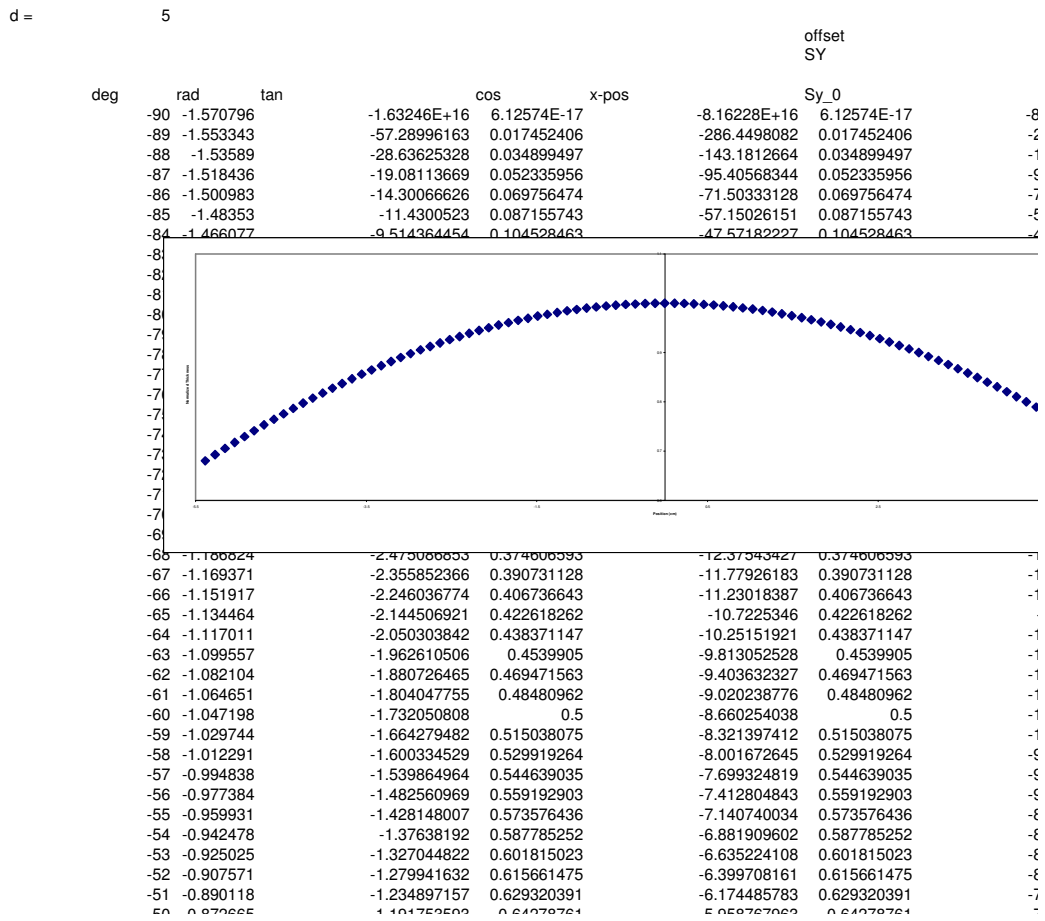| -68 | -1.186824 | -2.475066853 | 0.374606593 | -12.37543427 | 0.374606593 | -1 |
-67	-1.169371	-2.355852366	0.390731128	-11.77926183	0.390731128	-1
-66	-1.151917	-2.246036774	0.406736643	-11.23018387	0.406736643	-1
-65	-1.134464	-2.144506921	0.422618262	-10.7225346	0.422618262	
-64	-1.117011	-2.050303842	0.438371147	-10.25151921	0.438371147	-1
-63	-1.099557	-1.962610506	0.4539905	-9.813052528	0.4539905	-1
-62	-1.082104	-1.880726465	0.469471563	-9.403632327	0.469471563	-1
-61	-1.064651	-1.804047755	0.48480962	-9.020238776	0.48480962	-1
-60	-1.047198	-1.732050808	0.5	-8.660254038	0.5	-1
-59	-1.029744	-1.664279482	0.515038075	-8.321397412	0.515038075	-1
-58	-1.012291	-1.600334529	0.529919264	-8.001672645	0.529919264	-9
-57	-0.994838	-1.539864964	0.544639035	-7.699324819	0.544639035	-9
-56	-0.977384	-1.482560969	0.559192903	-7.412804843	0.559192903	-9
-55	-0.959931	-1.428148007	0.573576436	-7.140740034	0.573576436	-8
-54	-0.942478	-1.37638192	0.587785252	-6.881909602	0.587785252	-8
-53	-0.925025	-1.327044822	0.601815023	-6.635224108	0.601815023	-8
-52	-0.907571	-1.279941632	0.615661475	-6.399708161	0.615661475	-8
-51	-0.890118	-1.234897157	0.629320391	-6.174485783	0.629320391	-7
-50	-0.872665	-1.191753593	0.64278761	-5.958767963	0.64278761	-7

Figure 108. Excel spreadsheet for predicting film thickness.

Appendix B. Sample of Mathcad Calculation for Film Stress

An excel file containing the wafer profile before and after film deposition was first imported into Mathcad. From there it was broken down into smaller segments with a unique curvature and film thickness for each segment. The Stoney equation was then applied to each segment.

$d :=$ (C:\..\data_0.xls) $d2 :=$ (C:\..\data2_0.xls) $E := 384 \times 10^9$

$v := 0.28$

$i := 0 \quad s1 := 1 \quad s2 := 75$

$sub_i := submatrix(d, s1, s2, 0, 1)$ $sub2_i := submatrix(d2, s1, s2, 0, 1)$

$xval_i := (sub_i)^{\langle 0 \rangle} \quad yval_i := (sub_i)^{\langle 1 \rangle}$ $xval2_i := (sub2_i)^{\langle 0 \rangle} \quad yval2_i := (sub2_i)^{\langle 1 \rangle}$ $h_s := 546 \times 10^{-6}$

$z_i := regress(xval_i, yval_i, 2)$ $z2_i := regress(xval2_i, yval2_i, 2)$

$fit(x) := interp(z_i, xval_i, yval_i, x)$ $fit2(x) := interp(z2_i, xval2_i, yval2_i, x)$

$a_i := (z_i)_{5,0}$ $a2_i := (z2_i)_{5,0}$

$cur(p) := \frac{d^2}{dp^2}(a_i \cdot p^2)$ $cur2(p) := \frac{d^2}{dp^2} a2_i \cdot p^2$ +

$c_i := cur(0)$ $c2_i := cur2(0)$

$c_i = -0.017$ $c2_i = -0.028$

$s_i := \frac{E \cdot h_s^2 \cdot (c2_i - c_i)}{6 \cdot (1 - v) \cdot t(0)}$ $deltac_i := c2_i - c_i$

$s_i = -8.283 \times 10^8$

Figure 109. Sample of Mathcad program used for calculating residual stress.

About the Author

Patrick Waters has received all of his degrees in Mechanical Engineering from the University of South Florida. His primary area of research is in thin films and materials characterization. He was employed by Harris in Melbourne Florida immediately following graduation.